# FAULT PROTECTION AND REDUCED-ORDER MODELING FOR SECONDARY CONTROLLER DESIGN OF INVERTER-BASED MICROGRIDS

by

**Hashim Abbas M Al Hassan**

B.S., University of Pittsburgh, 2010

M.S., University of Pittsburgh, 2014

Submitted to the Graduate Faculty of

the Swanson School of Engineering in partial fulfillment

of the requirements for the degree of

Doctor of Philosophy

University of Pittsburgh

2018

UNIVERSITY OF PITTSBURGH

SWANSON SCHOOL OF ENGINEERING

This dissertation was presented

by

Hashim Abbas M Al Hassan

It was defended on

December 15, 2017

and approved by

Amro El-Jaroudi, PhD, Associate Professor
Department of Electrical and Computer Engineering

Brandon Grainger, PhD, Assistant Professor
Department of Electrical and Computer Engineering

Zhi-Hong Mao, PhD, Associate Professor
Department of Electrical and Computer Engineering

Gregory Reed, PhD, Professor
Department of Electrical and Computer Engineering

William Stanchina, PhD, Professor
Department of Electrical and Computer Engineering

Rajat Majumder, PhD, Adjunct Professor
SIEMENS Gamesa Renewable Energy

Dissertation Co-Advisor: Brandon Grainger, PhD, Assistant Professor
Department of Electrical and Computer Engineering

Dissertation Co-Advisor: Zhi-Hong Mao, PhD, Associate Professor
Department of Electrical and Computer Engineering

**FAULT PROTECTION AND REDUCED-ORDER MODELING FOR SECONDARY CONTROLLER DESIGN OF INVERTER-BASED MICROGRIDS**

Hashim A. Al Hassan, PhD

University of Pittsburgh, 2018

This dissertation studies fault detection in the case of low-fault current levels and reduced-order modeling of inverter-based microgrids. A phase-based fault detection method is developed that can detect faults regardless of fault current levels and without reliance on communication systems. The speed of this approach is increased by utilizing all the phases of the three-phase power system, effectively reducing the fault detection duration to one third of a cycle at most. Additionally, for any microgrid system configuration that would cause fault detection difficulties, a model-based fault detection approach is developed. This method can be used without communication for certain system constraints, which are derived analytically. Besides protecting the system properly, controllers are needed to stabilize the system post-faults or post-disturbance events. Model-based controller synthesis methods can be a plausible approach to this problem, but may result in high-order controllers. Using reduced-order models can lower the complexity of controller design. Hence, this dissertation also develops a reduced-order model for microgrids. A *dq* based reduced order model for secondary layer controller design is developed. The model has a significantly lower order with better accuracy than the current available models. A linear quadratic integral controller is designed based on the lower-order model to demonstrate the application of the proposed model. Simulations are performed to verify the proposed solutions in PSCAD and MATLAB/Simulink environments.

## TABLE OF CONTENTS

## LIST OF TABLES

## LIST OF FIGURES

## ACKNOWLEDGMENTS

First, I thank God Almighty for bestowing upon me countless favors that allowed me to finish this piece of work.

Second, I wish to express my deepest gratitude and love to the womb that carried me, and the heart that loved me unconditionally. My mother (Zakiah) faced many difficulties in her life. As a result of this, she gained a great amount of resilience and strength which helped in shaping the character that I am today. Although, she did not have the opportunities that I had, she realized the power and importance of education. She wanted nothing more but to give us all that she could possibly provide. From a young age, she always pushed me to be strong, more educated, and to be the best that I can be. Without her love, support, and high expectation of me, I would not have been where I am today.

I am also indebted to my father (Abbas) who continually motivates, and encourages me. At points where I felt lost or drained, he was there for the rescue. He was one of the few non-technical people that was willing to listen to my technical difficulties and actually provide useful recommendations. He has taught me the value of independent critical thinking, learning, and research. His habit of intellectual reading, research, and his huge library at home served as a great inspiration to me. Without my dad's encouragement and guidance, I would not have been able to finish this degree.

I also desire to express my thanks and love to my dear wife (Ola). She was instrumental in pushing me to grow in both my technical capabilities and soft skills. I also deeply appreciate her patience in putting up with my long hours at the lab, and in keeping an open ear listening to my frustrations and difficulties. Her faith and confidence in me during my low times was a key factor in helping me get past my obstacles. I thank her for offering a warm and loving environment at home. The love that is between us is truly the fuel that keeps my energy levels up and keeps me pursing my dreams. Without her sacrifices, I would not have been able to finish this degree.

I also would like to thank my three years old loving daughter (Israa) for being the light of our house and for putting up with my long hours at the lab. Although she does not realize it yet, she was a great motivating factor for me.

Additionally, I want to express my sincere appreciation to my advisors Prof. Mao and Prof. Grainger. Dr. Mao played the most important role in developing my analytical abilities. He played a key role in teaching me the fundamentals of academic research and critical thinking. He showed me how to become a true scientist and researcher. In addition, his encouragement and warm-hearted kindness helped push me forward. Dr. Grainger played the most critical role in this research. He served as a great consultant that kept his door open daily for technical conversations. He was always there for both technical and emotional support. I cannot express enough how great of an advisor he was. Not only that, he served as a great role model in terms of his work ethics and style which helped shape my current work style. Words truly fall short in thanking both Dr. Grainger and Dr. Mao.

I also would like to express my deepest thanks to Prof. Reed who served as a great mentor and role model. Dr. Reed helped me understand the power industry better. He also helped

shape my vision for the future. Additionally, his high expectations in terms of professionalism and communication abilities made me into the character that I am today. Dr. Reed made the power program at the university a truly unique one where I was able to grow in all aspects not just the technical one.

I also would like to thank Charles Luebke, Dr.Vijay Bharavaju, Dr. Qiang Fu for teaching me practical engineering R&D skills when I was interning with them at Eaton Corporation. I would like to thank the rest of my committee members for their contributions. In no particular order, these are Amro El-Jaroudi, William Stanchina, and Rajat Majumder.

I also would like to express special thanks to all my former and current colleagues. All of them helped in my growth and in making the lab a great enjoyable environment. In no particular order, these are, Patrick Lewis, Dr. Andrew Reiman, Dr. Ansel Barchowsky, Samantha Morello, Alvaro Cardoza, Dr. Mathew Korytowski, Dr. Hussain Bassi, Dr. Emmanuel Taylor, Thamer Alharbi, Dr. Robert Kerestes, Mathieu Bertin, and the rest of the team.

I dedicate this dissertation to my parents, wife, and daughter.

Hashim A. Al Hassan

# 1.0 INTRODUCTION

The degradation of the earth's environment, the depletion of conventional fossil fuel energy resources, and increased energy demands have led our society to explore alternative energy options. The idea of utilizing infinite clean energy resources such as solar and wind energy has always been the dream of engineers and researchers since at least the time of the great inventor Nikola Tesla. Nikola tesla stated the following in this regard [1]:

"*Whatever our resources of primary energy may be in the future, we must, to be rational obtain it without consumption of any material*"

Recently, great advancements have been made to generate, transmit, distribute, and consume such forms or renewable energy efficiently. One of the advancements made, which could make the wide spread of renewable energy resources a reality in the near future, is the invention and advancement of power electronic devices. Power electronics represent only one piece of the puzzle as an enabler of renewable energy systems. In particular, the traditional electrical grid may not be able to handle large amounts of renewable energy resources integrated via power electronic devices due to the distributed and intermittent nature of renewable energy. Hence, the other piece of the puzzle is forming alternative grid architectures that can handle the large amounts of distributed renewable energy integration. This has established the concept of "microgrid" (MG) to facilitate the integration of renewable energy resources [2], [3], [4]. The

microgrid concept was proposed not only as a way to facilitate renewable energy integration but also to increase grid reliability and security. The U.S. department of energy (DOE) defines a MG as follow:

"*A group of interconnected loads and distributed energy resources (DER) with clearly defined electrical boundaries that acts as a single controllable entity with respect to the grid [and can] connect and disconnect from the grid to enable it to operate in both gridconnected or island mode*"

Although in the DOE definition it includes the ability to connect and disconnect to the main grid, a broader MG concept can be and often is adopted to include standalone systems that cannot connect to the main grid. This is to include similar concepts that are built in rural impoverished areas with no access to a main traditional grid. Currently, an estimated 1.2 billion people lack access to electric power [5]. Microgrids can be the solution to help empower humanity's energy needs.

As I mentioned, one of the most beneficial features of a microgrid is the ability to integrate distributed renewable energy resources. This is because it is easier and more practical to exploit renewable energy that is spread and distributed across many areas as opposed to forming a central generation plant that exploits energy only at its location.

Integrating energy in a distributed fashion is also a more resilient, reliable, and secure way of transmitting energy. It is a way to prevent cascaded catastrophic blackout similar to the 2003 northeast blackout [6]. The 2003 blackout affected 50 million people when more than 61800 MW of electrical load was lost in many of the northeastern states as well as some parts of Ontario. This blackout lasted in some areas for more than two days with rolling blackouts over the following two weeks and cost over six billion dollars. The initial blackout occurred due to a

fault caused by trees that grew in the paths of power lines. When that fault occurred, it resulted in the shutdown of the line, which resulted in other lines carrying the additional load. Three other lines also shut down after sagging into trees, causing a major overload of the other power lines. This caused a series of failures from overloads in most of Northeastern America [6]. This kind of cascaded blackouts can be avoided if microgrids are utilized.

Therefore, microgrids can be used in places where high reliability is needed to provide power to critical loads. For example, critical loads such as hospitals and data centers can benefit greatly from microgrids, where continuous supply of power is highly critical. It could be also practical for university campuses, refugee camps, and military bases.

Industry is pushing to make microgrids a practical and economic reality by developing solutions to its different problems. For example, Eaton, ABB, SIEMENS, and GE are a few of the companies working to solve microgrid's technical problems [7]–[10]. "*Microgrid energy systems are becoming an exciting, even fundamental way to leverage new technologies, harness new energy sources and address new government regulations. Eaton's engineers see microgrids as the dawn of a transformative age—and the culmination of decades' worth of tireless research and development*."[7]. Figure 1-1 shows a layout of several microgrid energy systems.

Although the microgrid concept is designed to solve many of the traditional electrical grid problems, it has its own protection, stability, and control challenges [11]–[17] which need to be resolved to achieve its full projected benefits. Hence, the protection and modeling for controller design purposes are the main focus of this dissertation. The main contributions of this work are: (1) the development of phase-based communication-less fault detection method, (2) the development of model-based communication-less fault detection method, (3) the development of *dq* based reduced order model for secondary controller design purposes, and (4)

the application of LQI control on both the reduced-order and the full-order models for voltage control in microgrids to demonstrate the usefulness of the model.

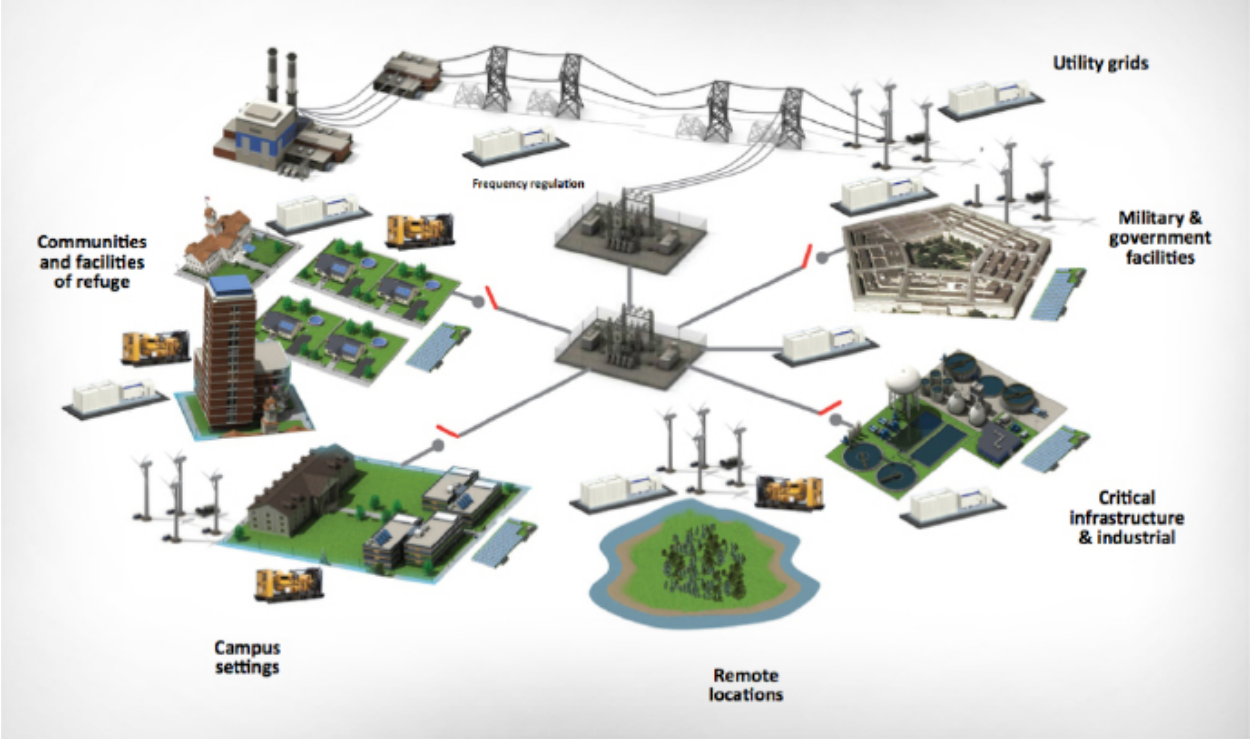


**Figure 1-1.** Layout of Several Microgrids [7]

## 1.1 OBJECTIVE

The protection challenges in microgrids hinder us from exploiting their full potential. One of the main causes for these challenges is the bi-directionality of power flow in microgrids as opposed to one-directional power flow in the traditional power grid. Also, future microgrids will be heavily inverter-based which adds further complications due to the lack of high fault currents associated with these devices[18]. Additionally, microgrids can operate either in grid-connected

or islanded modes of operation. This makes it difficult to use traditional protection methods [11], [19]–[21] such as overcurrent protection and fuses. Hence, many research articles have been published dealing with these protection issues [11], [22]–[31]. However, there are still many issues associated these solutions. Some of these protection problems will be a focus in this dissertation. Specifically, communication-less algorithms will be proposed to overcome the bi-directionality of power flow, different modes of operations, and the low-fault currents that inverter-based microgrids produce. Two methods will be proposed, the first one is a high-speed phase-based fault detection method, and the second one is a model-based fault detection method.

Inverter-based sources not only cause protection issues but also control and stability issues after disturbance (i.e., faults, load change, etc) scenarios and during normal condition scenarios. This has also always been a challenge due to the lack of inertia, uncertainty in renewable energy resources, and the different modes of operations. There are many control problems within microrids such as voltage control, frequency stability, power sharing, and transient stability. Many control paradigms have been proposed to solve many of microgrid control and stability problems [13], [28], [32]–[39]. One of these control and stability issues, is the ability to maintain stability in the case of load variation [40], [41]. One of the most common control approaches to microgrids is hierarchal control [36]. In hierarchal control, there are three layers of control (primary, secondary, and tertiary). This hierarchy is due to the fact that each control layer has a different timescale with the primary being the fastest layer, next the secondary, and then the tertiary [36], [37], [42]. The main objective of the primary control is to respond to fast changes to stabilize the system and to maintain proper load sharing between the generation units. The controllers used in this layer are usually the real power-frequency (P/f) droop controller and the reactive power-voltage (Q/V) droop controller [43], [44]. The objective

of the secondary controller is to compensate for voltage and frequency deviation caused by the primary controller. This controller is slower than the primary, and many central and distributed control techniques have been proposed for this layer [36], [42], [45]–[47]. Finally, the main goal for the tertiary controller is optimal economic dispatch [36], [48], [49]. In order to design and tune a controller in any layer, appropriate models have to be utilized. Secondary level controller design is an active area of research [32]. In many of the research articles to date, the full order model has been utilized [35] to design and tune secondary level controllers. However, this model is quite large consisting of 16 states per DG and makes using control design algorithms challenging due to the computational burden. Also, using this full-order model in control design could result in high-order controllers which are not desired in any control application. Hence, a lower order model is needed which is another focus of this dissertation. Reduced models have been developed in many papers [40], [50]–[55]. Here, a different approach to reduce the model is presented based on the physical insights of the system. Then, a secondary controller is designed based on this model and applied to the full-order model to demonstrate the effectiveness of the reduced-order model.

## 1.2 DISSERTATION ORGANIZATION

This dissertation will be organized as follow: In Chapter 2, literature review of microgrid protection, control, and reduced-order models will be given. In Chapter 3, the design of high speed fault detection and protective coordination of microgrids utilizing the phase change will be presented. In Chapter 4, the model-based fault detection method will be given. This method is

designed in order to protect microgrid configurations not protected by the method developed in Chapter 3. In Chapter 5, the *dq* based reduced-order model of the microgrid for secondary controller design purposes will be given. In Chapter 6, demonstration of secondary controller design using the reduced-order model will be made. Chapter 7 concludes the dissertation by providing future directions.

# 2.0 LITERATURE SURVEY OF AC MICROGRIDS

In this chapter, a literature review pertinent to the objectives of this research is given. The literature review is divided into two main sections. The first one is the protection section. The second one is the control section, which includes the reduced-order modeling literature.

## 2.1 INTRODUCTION TO MICROGRID PROTECTION

As energy demands increase, the electric power industry moves into the direction of adding more diversified and distributed energy resources (DERs). With the introduction of DERs, parts of our traditional distribution system can become microgrids (MGs). Microgrids may also be built from scratch to provide electric power to areas where building a transmission system is a challenge or uneconomical such as remote rural areas.

Although MGs could provide solutions to many electric power problems, there are many technical challenges that need to be resolved in order for MGs to be widely deployed. One of those challenges is the protection system design. The protection system that is designed for the traditional power system is not fully applicable to the MG because of the nature of MGs as power is not transmitted unidirectionally anymore, diversification of distributed sources such as diesel generators and inverter-based sources, and different modes of operations. In general, the

introduction of power electronic devices into the power system changes the protection system requirements significantly. This is evident not only in microgrids but also in many other applications such as high-voltage DC links [56], [57].

In this section, multiple objectives are achieved. First, protection problems are outlined. Then, a survey of the different microgrid protection strategies is presented. After that, protection strategies are grouped together and their associated problems are presented. Finally, gaps of the protection strategies are provided.

### 2.1.1 Microgrid Protection Problems

Based on the review of papers [11], [19], [20], [22], [23], [25], [27], [28], [31], [58]–[78], the following are the main problems associated with MG protection:

1. Fault detection, location, and isolation in an islanded MG where fault current is low due to the limited current contribution of inverter-based DERs (max 2 pu) which makes using overcurrent protection ineffective.

2. Disconnection of the MG by operating only the Point Of Common Coupling (PCC) circuit breaker during grid-side faults without tripping other breakers inside the MG.

3. A proper overall protection system works both in the grid-connected and in islanded mode of operation as faults are significantly different in each mode of operation.

4. Preventing nuisance tripping (false tripping) of overcurrent protection during grid-connected mode or islanded-mode where a DER could cause the breaker of the feeder (or any kind of branch) adjacent to the faulted feeder (or branch) to falsely trip as shown in Figure

2-1. $I_{DER2}$ may falsely identify F1 fault as fault on its feeder (a fault on point A) which will cause circuit breaker 2 (CB2) to falsely trip.

5. Preventing blinding of overcurrent protection during grid-connected mode. Blinding occurs for example when a fault occurs between the grid and a DER where the breaker on the grid side might not see enough current coming from the grid due to the DER current contribution or as shown in Figure 2-2. In this figure, protection device (PD) 1 will see different fault current levels depending on the level of $I_{DER}$ (which could be variable), depending on line impedance and fault impedance. Therefore, PD1 could become blind to faults downstream - at point B for example.

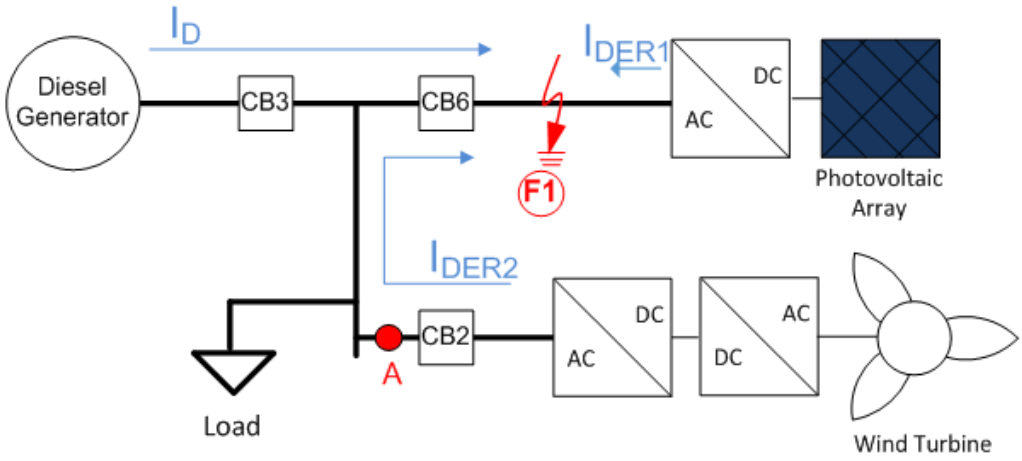


**Figure 2-1.** False tripping of the circuit breaker (CB2) seeing current $I_{DER2}$

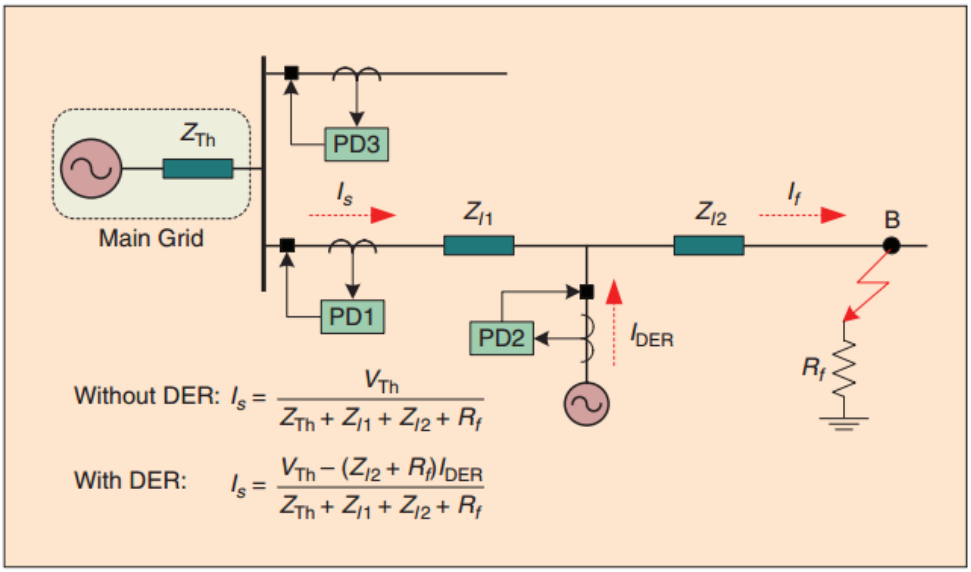


**Figure 2-2.** Blinding of circuit breaker CB2 [11]

6. Designing a proper protection coordination is a challenge due to the bidirectionality of power flow in the MG during both grid-connected and islanded modes of operation.

7. Traditional trip time curves and the nature of MGs cause fuses to trip during temporary faults which cause a permanent fault. It is desired to operate the reclosers in case of temporary faults and then operate the fuse or the breakers in case those faults do not resolve. Thus, proper methods to coordinate fuses and reclosers are needed.

8. Detect high impedance faults as high impedance faults is a challenge even in the traditional grid.

### 2.1.2 Review of Protection Strategies

Many protection strategies have been developed to attempt to deal with many of the problems mentioned in the previous section. However, these solutions are not complete and have different gaps.

In [20] the authors have designed one protection strategy that works for both islanded and grid connected operation. The authors have utilized differential current to protect against L-G faults for zones upstream of the fault, zero-sequence current for L-G faults for zones downstream of the fault, and negative sequence for L-L faults. Appropriate time delays have to be set for the proper operation of this protection strategy. One problem that [20] has not investigated is the case where distributed resources do not meet load demand. Another problem is they did not investigate grid side faults. According to their strategy, grid-side L-G faults should cause all relays to trip due to the presence of zero-sequence component.

In [58], the authors designed a protection system using digital relays that are assisted by communication in order to detect faults for the case of grid-connected and single-islanded or multiple islanded. Their protection system is based on differential protection and comparative voltage protection that relies on communication in order to protect the different MG configurations and change the fault levels depending on the status of the MG. This strategy is costly because it depends on differential currents and a communication system.

In [31], the authors have used a micro-processor based relay and utilized voltage, zero-sequence, negative sequence components of current, energy level, and directional element to design a MG protection relay (MPR) that works in both grid-connected and islanded modes and does not rely on communication.

An adaptive protection strategy for a MG has been proposed by [59] to protect MGs with high penetration of DERs. Their adaptive method is based on communication and works only in the islanded mode of operation. A multi-agent based strategy that depends on the large fault current supplied by the utility and uses a communication network has been proposed in [60]. Thus, this strategy can only work in the grid-connected mode.

Some other authors [61] have proposed a protection method utilizing traditional protection schemes and a communication network. Their method is based on overcurrent relays, which makes it work only in the grid-connected mode. In [27], the authors have proposed an integrated protection and control unit that utilized a communication network and used over current relays to isolate the fault which makes this method work only in the grid-connected mode as well.

An attempt to tackle the islanded MG protection problem has been done in [62] the authors tried to tackle the challenge by using differential relays which is a very costly method. In [63] the authors have developed a method based on differential sequence components that extract features form differential values through data mining approaches to protect against faults in an islanded MG. This method relies on communication and heavy signal processing which requires the use of microprocessors relays.

Voltage measurement along with an adaptive overcurrent scheme are proposed as a method to protect the MG when islanded [64]. In [65] voltage has been used as the mechanism to protect the islanded MG as well. This time the voltage measurements are converted into *dq* rotating frame and used to detect the faults. For this method to be implanted, a communication network has to be utilized.

Some authors have tried to boost fault current in an islanded MG by adding flywheels to the system [66]. This makes it easy to use the traditional protection system because flywheels supply enough overcurrent during fault for the protection devices to operate. This method is costly and depends on the proper operation of flywheels.

Some authors mix different strategies in one protection method in order to enhance their method as in [25]. The authors have developed a protection method based on two strategies. The first one is based on impedance differential which uses a communication system to protect the MG in all modes. This strategy serves as the primary protection method. A back-up protection based on inverse-time low-impedance protection is the second strategy in case the primary protection fails. This protection system is expected to be expensive since using differentials is expensive.

In [19] the authors have investigated using central control and monitoring infrastructure in order to change relay settings in digital relays in order to protect MGs in both the grid-connected and the islanded modes of operation.

In [67], the authors identified and located faults by doing wavelet packet transform of the *dq* components. They implemented their method in digital multirelay and showed that it works for both grid-connected and islanded modes. This method is complex and requires extensive computation because of the signal processing needed.

The authors in [28] have investigated protecting a typical distribution system that is turned into a MG by introducing DERs, they have dealt with the recloser-fuse incoordination problem in the grid-connected mode by replacing feeder auto-recloser with a digital recloser and designed algorithm for proper coordination of the recloser and the fuse. The have also proposed different scenarios for protecting the Micro-grid when islanded such as total shut down of the

MG during faults, two-mode protection relays that change settings depending on the status of the grid (islanded or grid-connected), and a scenario where the relay is designed for both modes without having to change any settings.

In [68], the authors have developed a differential zone protection scheme. This scheme is based on taking measurements at the borders of zones and calculating the differential. The authors claim that their method is as effective as differential line protection. However, it is costly due to the use of the differential scheme.

In [22], protection of islanded multi-microgrids (MMG) have been investigated. The authors have utilized differential current and directional component in their algorithm in order to protect a multiple microgrid system consisting of two MGs.

In [69] the authors have designed adaptive relays with algorithms that detect the mode of operation and the faulted section then update the relay settings depending on the mode and the fault to protect the system. They used time overcurrent characteristics in order to identify the faulted section. Their protection algorithm is based on directional overcurrent component, current measurements, voltage measurements, and the frequency.

In [70] and [71], the authors used the traveling wave initial surge generated by the fault and recorded at the ends of the feeders and utilized mathematical morphology technology to protect a MG with high penetration of inverter-based sources. Their method relies on low-bandwidth communication channel to identify faults and coordinate breakers.

A harmonic based method has been developed by Al-Nasseri et al. in [72] where the fundamental voltage component is used to detect and determine the type of fault. The fundamental component amplitude of the faulted phase is expected to drop compared to other phases. Then, the THD is used to determine the faulted zone. The THD of the faulted phase will

be greater than the THD of the un-faulted phases. This method requires a communication channel in order to identify the faulted zone and trip the proper circuit breaker. A hybrid method using multi-resolution wavelet analysis and current traveling wave generated by the fault is proposed in [73] but has not been validated by simulation nor experiments. Artificial intelligence methods have also been developed in [74], [75]. One method is based on particle swarm optimization and the other is based on differential evolution algorithms.

Also, in [76] a search algorithm based on graph theory has been proposed to coordinate relays in the MGs. An observer-based approach has been proposed in [23]. The approach is based on an observer design and using current measurement at one end and voltage measurement at two ends to determine the state of the zone (faulted or unfaulted). A combination of different techniques has been proposed in [77]. The authors proposed using the rate of change of frequency as a primary quick fault detection method and used under and over voltages as a back-up protection method as the rate of change of frequency might fail to detect some faults depending on time-delay.

### 2.1.3 Main Problems with the Different Classes of Strategies

Protection solutions has been classified by [79] into 6 main classes. The classes and their associated problems is as follow:

A. Adaptive Protection Systems:

    1. A knowledge of all possible configurations has to be known before designing the protection system.

2. Power flow and short circuit studies have to be done every time the topology of the MG changes.
3. Traditional power system protection devices have to be upgraded.
4. A communication system is necessary.

B. Voltage-based methods:

1. Protection failure could be caused by minor voltage drop differences in relays at the two ends of short lines.
2. For methods using the *dq* voltage, a high calculation complexity is involved.
3. The method is weak when it comes to detecting high impedance faults.
4. With the high penetration of distributed generations, voltage based methods could experience problems.
5. The methods rely on communication infrastructure.
6. They depend on network architecture.
7. Slows down protection significantly due to IEEE1547 voltage-ride through requirements for renewables.

C. Differential Protection:

1. Measurements have to be synchronized.
2. DG connection/disconnection cause transients that could cause problems to this protection system.
3. Unbalanced loads cause problems.
4. High communication infrastructure and high CT installations are needed.
5. High cost.

D. Distance Protection:

1. Unreliable detection due to limited fault resistance.
2. Fault resistance cause errors in measuring admittance.
3. Down-stream source infeed increase tripping time.
4. Accuracy is degraded because of harmonics, current transients, decaying DC magnitude and time constant.

E. Overcurrent protection and symmetrical components:

1. Problems with accuracy.
2. Grid side faults may cause all breakers to trip.
3. The whole protection system fails in case of communication failure.

F. Using external devices to improve the protection:

1. High cost associated with storage devices.
2. Maintenance is critical for devices with high short circuit capability such as flywheels.
3. Highly dependent on the accurate operation of islanding detection and correct operation of the current source.

It is worth noting here that the main issues regarding fault detection that this research attempts to solve are the issues of low-fault current levels, different modes of operation, and bi-directionality of power flow. These issues make it difficult to detect faults especially if communication systems are not used. It is more desired that fault detection is communication-free in order to decrease cost and improve reliability. Proposed solutions without reliance on communication are given in Chapters 3 and 4.

## 2.2 MICROGRID CONTROL OVERVIEW

The problem of fault detection mentioned in the previous section is not the only critical problem when it comes to the operation of microgrids. Additional critical aspects of microgrids are the ability to have a stable operation during normal operation and to recover from severe disturbances such as large load changes and faults. The reason why this is critical is that, a severe disturbance such severe load changes might cause the system voltage to fall below accepted voltage deviations. Hence, improved controllers are needed to improve post-disturbance and steady-state stability of microgrids. The focus here is on secondary controllers, which are responsible for compensating for voltage and frequency deviations.

In order to design secondary controllers, appropriate models have to be used. Many control synthesis algorithms use the model of the system to synthesize controllers. When that's done, the controller synthesized has an order similar to the model order. Hence, a reduced-order model is one of the methods used to reduce the order of the controller. Therefore, a reduced order model will be developed for this objective in Chapter 5. Before doing that, it is essential to understand microgrid control methods. Therefore, a review of microgrid control and modeling will be given in this section.

### 2.2.1 Microgrid Control Background

The microgrid has many issues that need to be overcome to fully utilize its full potential. One of the most important issues that needs to be fully resolved is microgrid control and stability. Microgrid control is more challenging than traditional power system control due to the lack of

inertia, resistive nature of cables, uncertainty of produced energy, and unbalanced conditions of the system [32]. Microgrids are controlled in hierarchical manner with three layers of control (primary, secondary, tertiary) as shown in Figure 2-3. This hierarchy is due to the fact that each control layer has a different timescale with the primary as the fastest layer, then secondary, then tertiary [36], [37], [42]. The main objective of the primary control is to respond to fast changes to stabilize the system and to maintain proper load sharing between the generation units. The objective of the secondary controller is to compensate for voltage and frequency deviation caused by the primary controller. Finally, the main goal for the tertiary controller is economic dispatch.

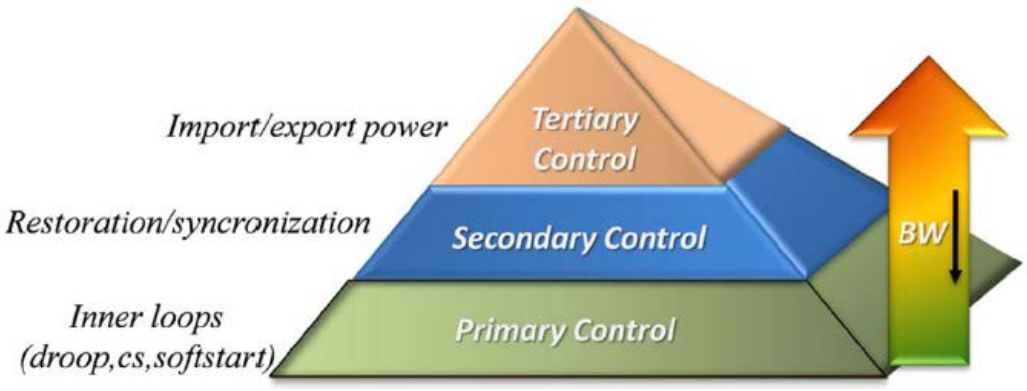


**Figure 2-3.** Hierarchical Control layers of a microgrid [36].

#### 2.2.1.1 Zero-Level Control

Zero-level control which is often called “inner loops” is responsible for controlling voltage and current specified by the primary controller. Zero level controllers are presented in subsections 5.2.2 and 5.2.3.

#### 2.2.1.2 Primary Control

There are many methods that are used in the primary controller to share the active and reactive power and to stabilize the system in microgrid systems. The primary power sharing methods can be mainly classified into droop-based methods and non-droop based methods [32].

The droop control concept in microgrids is borrowed from the conventional control methods of synchronous generators in traditional power systems. This traditional concept is completely decentralized (no communication at all) which makes it very attractive. It is based on the fact that when there is an increase in real power demand the speed of the prime mover in the synchronous generator is decreased and the prime mover speed is proportional to the system frequency. Hence, the frequency set-point is increased which makes the generator produce more real power. The voltage and reactive power behave in a similar manner; the output reactive power varies according to variation in voltage. This frequency and real power droop and voltage and reactive power droop can be artificially designed for inverters in microgrids [32]. Droop control method is very popular and thoroughly researched in the literature [43], [48], [80]–[85]. The basic frequency and real power droop, and voltage and reactive power droop are implemented according to the following equations, respectively:

$$\omega = \omega^* - D_P(P - P^*) \tag{2.1}$$

$$V = V^* - D_Q(Q - Q^*) \tag{2.2}$$

where $\omega^*$, $V^*$, $P^*$, and $Q^*$ are the references for the angular frequency, voltage, real and reactive power, respectively. $P$, and $Q$ are the measured real and reactive power, respectively. $\omega$

and $V$ are the new set points sent to the inverter inner controllers. $D_P$ and $D_Q$ are the droop coefficients which can be determined using optimization techniques [86] or heuristically to satisfy [87], [88]:

$$D_{P1}P_{n1} = D_{P2}P_{n2} = ... = D_{PN}P_{nN} = \Delta\omega_{\max} \tag{2.3}$$

$$D_{Q1}Q_{n1} = D_{Q2}Q_{n2} = ... = D_{QN}Q_{nN} = \Delta V_{\max} \tag{2.4}$$

where $\Delta\omega_{max}$ and $\Delta V_{max}$ are the maximum angular frequency deviation and maximum voltage deviation, respectively. $P_{ni}$ and $Q_{ni}$ are the nominal active and reactive power of the $i$th DG, respectively. $N$ is the number of inverters in the microgrid.

The conventional droop control is based on the assumption that that the network impedance is mostly inductive which is the case in the traditional power system. However, microgrids have mainly resistive networks. Therefore, alternatives such as voltage-real power control and frequency-reactive power control are proposed [89]–[91]. This is exactly the opposite of the traditional droop control. Another approach is through the use of a virtual impedance in the control loop in order to have accurate droop characteristics using the traditional droop and decouple real and reactive power control even when lines are both resistive and reactive[38], [39], [92], [93]. Another approach proposed is through the use of virtual synchronous frame transformation in which decoupling of real and reactive power is achieved [82], [94]–[97].

Non-droop based methods are central controllers (using central communication) to achieve the goal of primary control. In [35], [98], a central controller is proposed where total the

load is sent to the central controller and commands based on the distributed generation characteristics is sent back to the individual DGs. In [45], a master-salve control approach is proposed. Other central controllers are proposed in [99], [100] and with different communication requirement such as requiring low-bandwidth or using CANbus communication. In general, this type of controller is not very attractive because it is prone to a single point-of-failure.

An interesting primary control method is the virtual synchronous generator (VSG) method [101], [102] where control loops of the inverters are designed in such away to mimic the behavior of synchronous generators.

When there is a grid-interfacing converter in a grid-connected application, many control methods can be implemented alongside the power sharing control for grid synchronization such as proportional resonant controllers (PR), proportional-integral (PI) controllers, hysteresis or dead-beat controllers [103], [104].

#### 2.2.1.3 Secondary Control

The secondary controller main function is to compensate for voltage and frequency deviations, which are caused due to the primary controller action. This controller is slower than the primary one and it is usually implemented in a centralized fashion. However, there have been many research efforts to make the secondary controller less central and make it distributed instead. The different control schemes (with respect to communication and centrality vs. less communication and distributed) have been proposed for the secondary layer [36], [42], [43], [45]–[47], [105]–[112] .

#### 2.2.1.4 Tertiary Control

The tertiary controller is the slowest control and it is responsible for economic dispatch. This controller is active when the microgrid is grid-connected to regulate power flow between the grid and the microgrid based on optimality [36], [48], [49]. Figure 2-4 shows a summary of the different control levels with their objects, methods and speed of response.

### 2.2.2 Microgrid Reduced-Order Modeling Review

Reduced models have been developed in many papers [40], [50]–[55]. A reduced order model including the dominant modes has been derived in [55]. Nevertheless, their model is for single-phase systems and excludes network dynamics. A reduced order model has been derived in [113] using the well-known singular perturbation technique. Nonetheless, the model developed is suitable for stability analysis and is not well suited for secondary control design. The authors in [53] produced an effective low-order (15 state) model for a 2 DG microgrid system as opposed to a 36 state full order model. However, the work neglects the network dynamics. Their model also relies upon utilizing the operating point of the full-order model which can be hard to obtain.

Most of the reduced models use mathematical tools such as the singular perturbation technique to reduce the model and ignore the network dynamics. Ignoring the network dynamics is satisfactory for high-inertial systems but stability results may not be accurate for low-inertial microgrids [50], [52]. The authors in [52] attempted to include the network dynamics. However, they developed a phasor-based model and they ignored the coupling between DGs. The coupling between units affects the dominant modes of the system which will be shown in Chapter 5. It is also more desirable that the reduced model be constructed in the conventional *dq* reference frame

so that it captures the modes of interest for the control objectives of the secondary layer. Hence, a reduced-order *dq* based model that includes network dynamics and coupling effects is developed in Chapter 5.

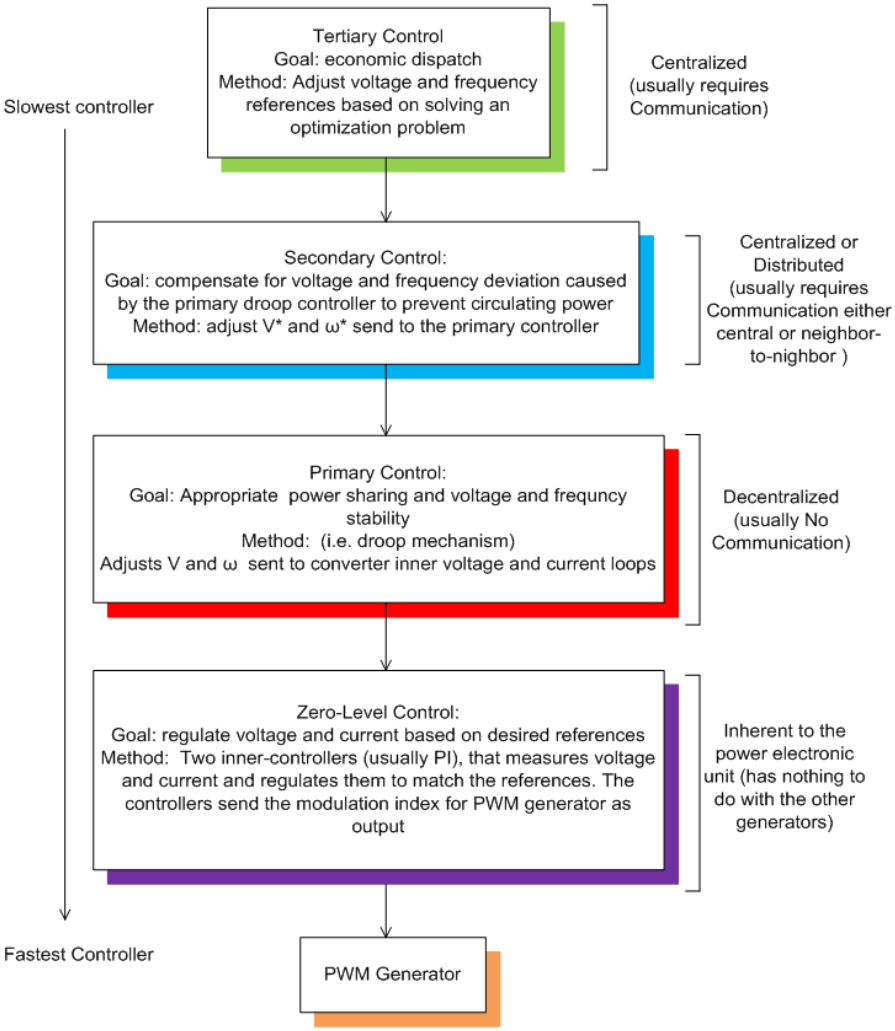


**Figure 2-4.** The different layers of control levels in a microgrid.

# 3.0 HIGH-SPEED PHASE CHANGE BASED FAULT DETECTION AND PROTECTIVE COORDINATION

Detecting faults in microgrids is extremely challenging due to the bi-directionality of power flow and the limited fault currents produced by inverter-based sources. Hence, a method is developed here in order overcome such challenges. Additionally, knowledge of the fault feeding side (fault direction) is a necessary element to properly protect the microgrid and avoid blinding and nuisance tripping. Hence, the method developed determines the fault direction with good speed. Phase change of the phase difference between voltage and current happens to be an indicator that satisfies these objectives and adheres to the constraints of the microgrid. This chapter explores the use of such an indicator and uses it as a foundation to propose a novel high-speed fault detection and fault direction detection method. A protective coordination algorithm is also proposed. The performance of the proposed solution is demonstrated in the PSCAD/EMTDC simulation environment.

## 3.1 INTRODUCTION

Protection is one of the most critical and challenging problems when it comes to microgrid systems. The limited current contribution from inverter-based sources, the bi-directionality of

power flow, the diversification of distributed energy resources (DERs), and the different modes of operation are the elements which cause difficulty in protecting microgrids [1-2]. Traditional over-current protection is not a reliable method when it comes to protecting the microgrid due to lower available source currents resulting in longer trip times [1-2]. Most methods in the literature depend on differential protection and a communication system in order to achieve this objective which can be slow and very costly [1-3]. Relying on communication degrades the reliability because the system becomes more prone to a single point of failure. Others have used sequence components, which fails in detecting balanced three-phase faults and is unreliable in the case of unbalanced conditions [2], [4]. Some have used data mining approaches along with the differentials which are complex methods and also depend on communication [5]. The same is true for traveling wave based approaches [6-7]. Wavelet analysis has been proposed in [8] and has not been validated. In [9], the authors have added a flywheel in the microgrid in order to boost up fault currents and use traditional over-current protection. This method is costly and depends on the proper operation of the flywheel. A combination of different approaches have been proposed in [10] with differential protection as the main strategy. This method is costly and slow since it relies on other mechanisms as backup.

Here, an alternative scheme will be explored in order to protect the microgrid. Specifically, the scheme will overcome the issues of low fault levels and bi-directionality of power flow that may cause blinding, nuisance tripping, or slow tripping times. This alternative cannot be based on voltage levels alone because renewables have to meet low-voltage and high-voltage ride through requirements (IEEE1547). Detecting the fault direction is critical to deal with the bi-directionality of power flow and to perform proper protective coordination. If this objective is achieved along with detecting the fault with good reliability and speed, microgrid

protection becomes manageable. The most practical method to achieve this is using directional relays. However, traditional high-speed directional relays determine the direction of current in 20 ms [11], which is not fast enough in order to reliably protect the microgrid weak sources.

In this chapter, three main goals will be accomplished. These include: first, justify the use of phase change between voltage and current as the main indictor to detect faults and fault direction to properly operate a circuit breaker (CB). Second, utilize this indicator (phase change) and develop an approach to identify the direction of the fault and coordinate between circuit breakers faster than traditional high-speed directional relays. In this case, phase detection will be processed faster by exploiting all of the phases of the three-phase system along with their negative counterpart. A method to extract the fastest and the second fastest detection from the different signals is also developed. Finally, implement the indicator in a protective coordination algorithm.

## 3.2 BASIC PRINCIPLE OF FAULT AND FAULT DIRECTION DETECTION

### 3.2.1 System Configuration for Investigation

Correct modeling of the microgrid system under faults is critical in our investigation of finding an indicator for fault detection and direction detection. The microgrid system that is being studied in this chapter is shown in Figure 3-1. This microgrid is similar in configuration to the one installed by Eaton in Menomenee Falls, Wisconsin. The microgrid contains a diesel generator, photovoltaic array system (PV) and wind turbine system (WT). Diesel generators

generally produce 3 to 7 per unit (p.u.) current during faults. Hence, this diesel generator is modeled to deliver a maximum of about 5 p.u. Inverter-based sources limit fault currents to a maximum of 2 p.u. during faults. Hence, they are modeled here to produce 1 p.u. during faults. The rating of the diesel generator is 1.8 MVA, the rating of the WT and PV are 0.420 MVA and 0.2196 MVA, respectively. The PV and wind systems are average models represented by controlled current sources. They produce a maximum of 1 p.u. during faults. It is important to note that inverters switch from supplying real power to fully reactive power during faults. This feature is also represented in the modeling efforts. Note that the diesel generator is represented by a voltage source with variable frequency input to validate the method under variable frequency conditions.

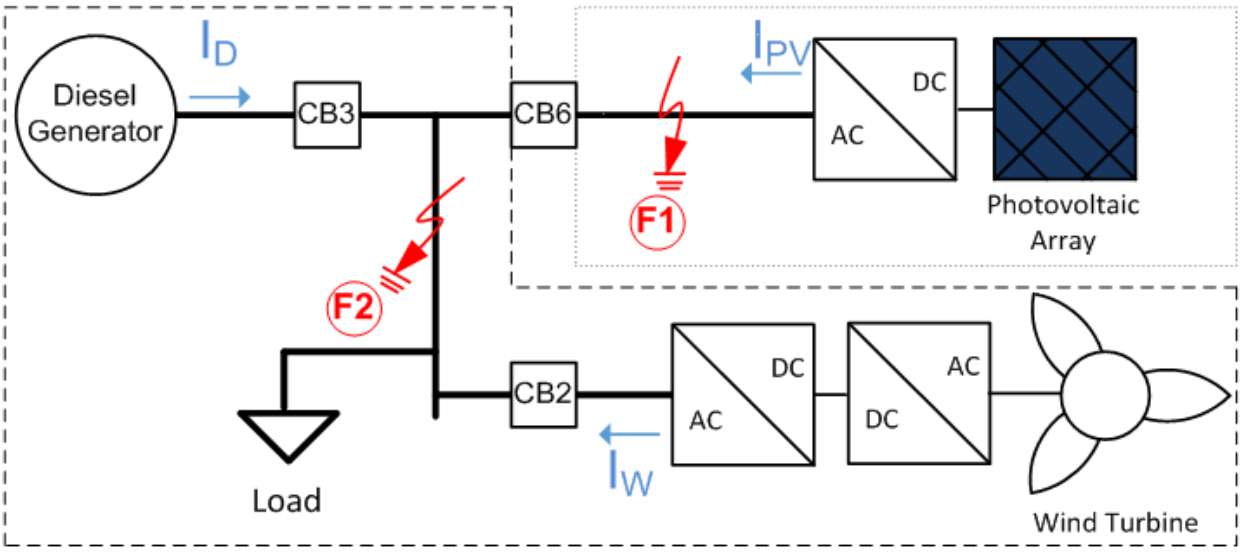


**Figure 3-1** Microgrid System for Studying Faulted Scenarios

### 3.2.2 Fault Detection and Direction Detection Principle

As noted previously, the inverter-based sources transition to supply full reactive power during faults. The transition from real power (power factor (PF) = 1) to reactive power (PF = 0) causes a $-90^0$ degree shift in phase between voltage and current. This characteristic of inverters can be used as one distinguishing indicator for detecting faults and the fault current direction. For example, if a fault F2 occurs in the system of Figure 3-1, or any fault to the left of CB6 (dashed line area which is referred to as a Microgrid side faults (MGSF)), the current transformer (CT) at CB6 will see only the current contribution, IPV, coming from the PV system. This is because all of the other currents (ID and IW) will be feeding the fault F2 and will not pass through the CT at CB6. The CT at CB6 will see a $-90^0$ phase difference change because the inverters only supply reactive power during the system fault duration. This phase difference is not present if the fault occurs to the right of CB6, (solid line area which is referred to as source side fault (SSF) according to CB6) such as fault F1 because in this case the CT at CB6 does not see the PV fault current and it sees other currents that give rise to a different phase angle explained in subsequent paragraphs. Based on this example, we can be confident that a $-90^0$ phase change means a fault not on the inverter-based feeder adjacent to the CT (not a SSF according to local relay).

In general, breaker CB6 needs to be opened for its own SSF (faults in the PV feeder) and to be kept closed temporarily for MGSF (faults on the busbar or other feeders). The only time it is required to open breaker CB6 for a MGSF, after some time based on voltage level (to account for voltage ride through), is when a busbar fault is identified. This is because a fault on the busbar cannot be isolated unless all of the feeder breakers are opened. This helps isolate only the faulted section and achieve minimum loss of generation during faults. The requirement is the

same for breaker CB2 and CB3. Hence, they should open for SFF and remain temporarily closed for MGSF (SFF and MGSF in prospective to their CB and CT location). All breaker coordination can be done if we can distinguish between SSF and MGSF types.

So far it has been shown how to detect MGSF. Using the phase difference change as the indicator again, the fault and current direction can be detected in the case of faults feeding from the source side (SSF, i.e. right of CB6 and CB2, left of CB3). In those instances, it is clear that the current reverses its direction in order to feed the fault. This current reversal causes the phase angle to change by $180^0$. This principle can be applied to protect many other microgrid configurations, in particular, those containing inverters only or microgrids containing inverters and rotating machinery. The question left to be answered is how to measure this phase change faster than high-speed directional relays (<20ms) in order to open or maintain circuit breakers in the closed state to prevent damage to weak generation sources.

## 3.3 PROPOSED HIGH-SPEED PHASE MEASURMENT STRUCTURE

### 3.3.1 Phase Measurement Basic Unit Structure

The phase difference between two signals is shown in Figure 3-2. The figure shows the phase difference between voltage and current for the case when the current is leading the voltage. The diagram shows 4 distinct regions from which the phase can be determined. The four areas corresponds to: (1) Rising edge of I then the rising edge of V. (2) Falling edge of I then falling

edge of V. (3) Rising edge of V and a falling edge of I. (4) Falling edge of V and rising edge of I.

When the current lags the voltage, the same four areas in Figure 3-2 appear but in a different order. Any of the four areas in Figure 3-2 can be utilized in order to design a high speed phase measurement unit. Depending on the phase angle change and the point of wave on which the fault occurs, one of the areas will produce results faster than the others. However, for simplicity, the focus will be on the use of area (1). The design approach that is taken is irrespective of whether the current is leading or lagging the voltage.

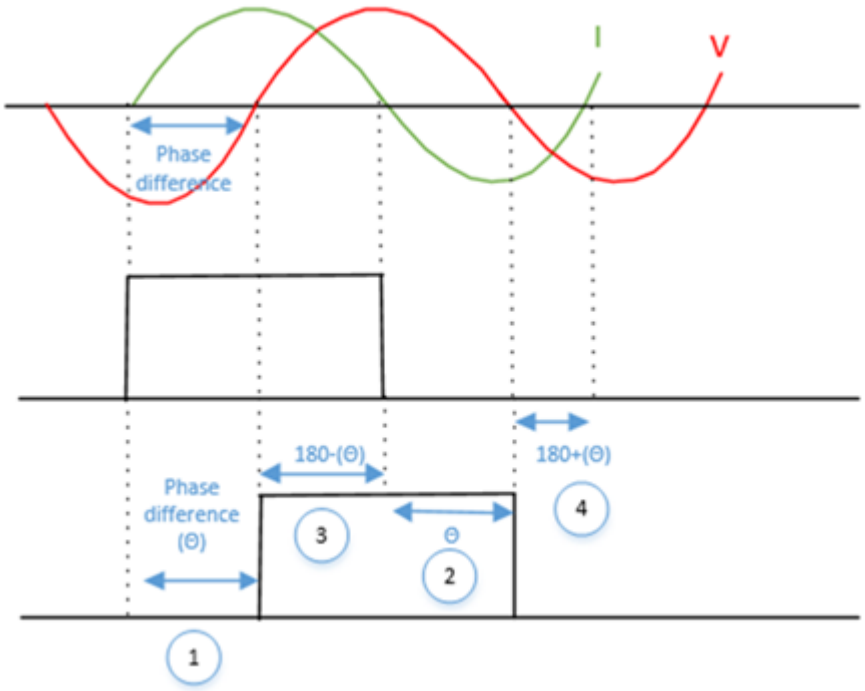


**Figure 3-2.** Graphical illustration of phase difference for the case when current leads voltage.

There are many approaches to design a phase measurement unit. Here, basically the phase measurement is detected by counting the number of samples between zero-crossings.

Figure 3-3 shows one cell (substructure) of the measurement unit modeled in PSCAD. The sinusoidal signals are converted into square waves where the negative area is 0 and the positive is 1. Then, a rising edge detector is used to determine when a rising edge occurs in each of the signals. After that, the output of the current rising edge detector is fed to the reset input of the counter while the counter input is always fed a constant numerical value of one for each sample. The voltage rising edge detector output is fed to a read time block. The job of the read time block is to determine the instant at which we read the counter signal. The output is then multiplied by $360f\tau$, where f is the frequency of the signal and $\tau$ is the sampling time.

The desire is for the unit to operate much faster than 20 ms. Hence, we utilize other signals in the microgrid as references. One phase of the current is compared against six voltage signals. These include voltage phases (A, B, and C) and their negative counterpart (-A, -B, -C) as shown in Figure 3-4. Each phase of the three phase measured current signal, taken at one of the CB locations, is compared against the six voltage signals mentioned resulting in 18 unique comparisons.

Utilizing six signals divides the phasor diagram into six distinct areas as shown in Figure 3-4. Hence, depending on the point of wave on which the fault occurs and the change of phase angle, the faulted phase angle will be positioned in one of those six areas. Therefore, taking the vector closest to the new shifted fault vector, as the calculation reference, will give the quickest phase detection. For example, in Figure 3-4, vectors C and –A will give the quickest phase detection magnitude when they are utilized as references given the faulted current vector, IA_F. For this example, the expected phase detection time (t) can be calculated as follows noting that Ts is the duration of one period of the AC signal and fs is the fundamental frequency

$$t = \frac{T_s}{6} = \frac{1/f_s}{6} = \frac{1/60Hz}{6} = \frac{16.67ms}{6} = 2.78ms \tag{2.1}$$

This is very quick and it's only utilizing area (1) of Figure 3-2. If all areas are utilized, the phase detection becomes even faster (4 times faster in theory). For design simplicity, we will use one area of Figure 3-2 to demonstrate the concept. For each current phase signal, 6 units such as the one in Figure 3-3 are needed, totaling 18 units for all 3 phases of current.

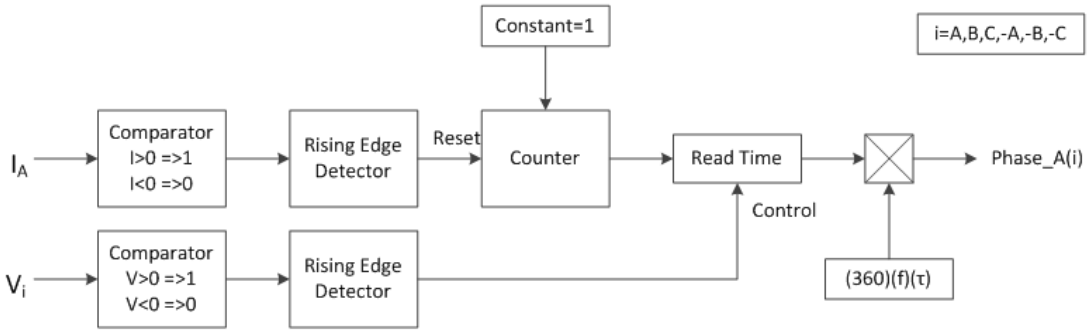


**Figure 3-3.** Phase measutment unit substructure

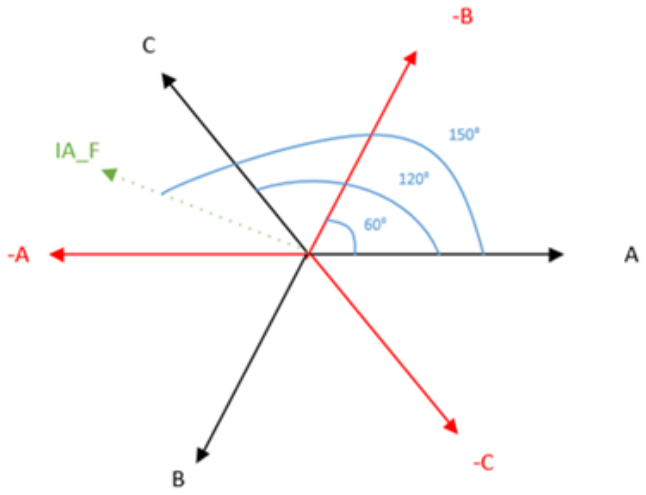


**Figure 3-4.** Six microgrid reference signals for phase detection

### 3.3.2 Central Processor for Utilizing Quickest Detection

The ultimate goal of the phase information is to detect faults and determine fault current direction within the microgrid ($90^0$ indicates one direction and $180^0$ indicates the opposite direction) to trip a circuit breaker and for performing protective coordination. Hence, there is a need to send the quickest directional signal to the protective coordination logic to trip appropriate breakers. The fastest reference after confirming with the 2nd fastest reference (totaling 2 out of the 6 references in Figure 3-4) has to be determined for each phase. Hence, 2 signals are utilized from the 18 comparison signals (each of the 3 current phases compared against 6 references in Figure 3-4) generated by the overall apparatus. The problem is that we do not know in advance which two vectors give the fastest and 2nd fastest detection because we do not know where the fault vector will position itself with respect to the six signals in Figure 3-4. This is due to the lack of knowledge of the point on-wave on which the fault occurs. This is solved by using a central processor shown in Figure 3-5.

Figure 3-5 shows the central device that processes all the signals coming out of each phase detector in Figure 3-3 in order to send a command signal to the protective coordination algorithm (section IV). First the phase is detected using the apparatus in Figure 3-3 for phase i, where i=(A,B,C,-A,-B,-C)=(1,2,3,4,5,6). Then PhaseA(i) is sent to a comparator to check whether the phase is $180^o$ to indicate direction reversal (to indicate a local SSF). The output of the comparator is then sent to a D flip-flop to store the value at the instant the comparator signal becomes 1 and stores it in FFP(i) for all future time for validating against other signals at a later time (to confirm the 1st fastest detection with the 2nd fastest detection signal). Each current phase signal of the three phase signals produce a FFP(i) (six FFP(i) for each phase). The value 1

is stored to indicate $180^0$ phase change at the instant that phase change is detected. When the output of the flip flop (FFP(i)) is 1, this gives an indication of a direction reversal as soon as it occurs (to indicate a SFF). Signal FFP(i) is then sent to an AND gate. This AND gate is used to validate the first fastest detection with a second detection of the 2nd fastest signal producing signal SIG(i). Since we are not sure which signal gives the fastest nor 2nd fastest, the second input to the AND gate is the output of an OR gate that takes the remaining 5 FFP(i) signals and OR them together. Hence, 6 AND gates are used to compare each of the 6 FFP(i) signals with FFP(i) of the fastest of the remaining 5 signals. Hence, one of the AND gates will give its 1 value signal earlier than the remaining ones when there is a direction reversal. For protective coordination purposes, only the indication of the direction reversal is needed, at the instant direction reversal is validated, without having to know which signal gave the indication. Hence, the outputs of the AND gates are sent to an OR gate. This OR gate gives a value (Sig_Fast_180_IA=1) when phase A current (compared to 6 voltage references) sees a $180^o$ phase angle change (direction reversal) immediately when confirmed with the 2nd fastest reference.

For the remaining B and C phases, two more OR gates are utilized. They are not shown in the figure and only their outputs Sig_Fast_180_IB and Sig_Fast_180_IC because they perform the same operation described previously and of the same structure of the total logic producing Sig_Fast_180_IA. All three are implemented to give an indication of direction reversal on each of the three current phases. For protective coordination purposes, we would need an indication of directional reversal in any of the phases regardless of that phase. Hence, the outputs of each of the three OR gates is sent to the final OR gate that gives a value of 1 (Sig_Fast_180=1) as soon

as a confirmed direction reversal occurs on any of the phases of the current. Hence, when Sig_Fast_180=1, this confirms a local SFF according to the local relay.

For a MGSF, an indication of 90º phase shift is desired. Hence, the same logic in Figure 3-5 is duplicated and the only difference is the comparator value to send an indication of 90º phase change. The output of the final OR gate for this scenario is named (Sig_Fast_90) here. When Sig_Fast_90=1, this confirms a MGSF.

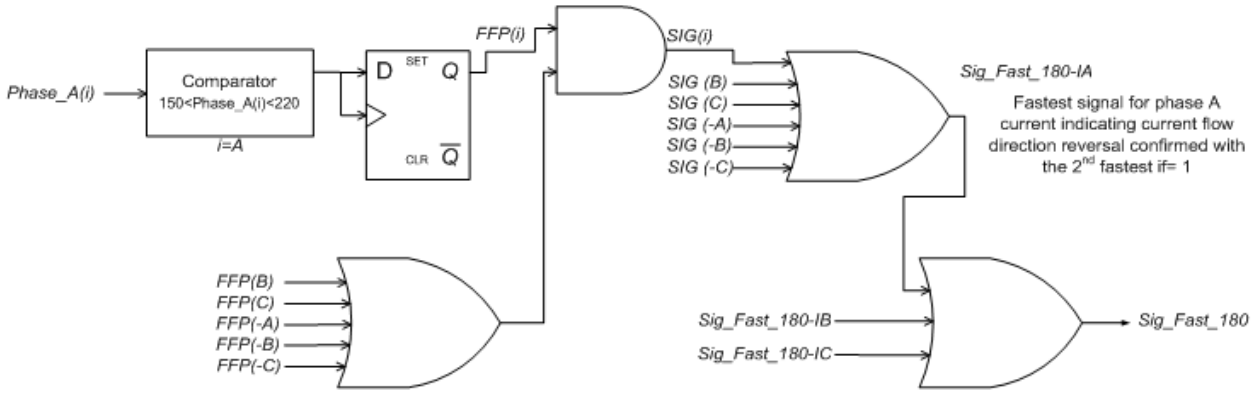


**Figure 3-5.** Central processor to give 1800 phase shift indication based on the quickest and 2nd quickest references for all phases of the current.

## 3.4 BASIC PROTECTION COORDINATION ALGORITHM

The previous apparatus and logic is implemented at the relay responsible for each circuit breaker of the microgrid. Then, the output of the logic for each breaker is sent to algorithms A, B1 and B2, which are presented here.

### 3.4.1 Local Source Side Faults (Algorithm A)

This part of the algorithm determines whether the fault is in the source side feeder (local SSF, i.e. to the right of breaker CB2 and CB6 or left of CB3) and trips the associated breaker if the fault is on the source side and not the microgrid side (MGSF). The algorithm is shown in Figure 3-6. First the signals are collected for each CB locally and individually. Then the algorithm determines if the output of the central processor is equal to 180$^{o}$ (Sig_Fast_180=1 in Figure 3-5 is equal to 1). If Sig_Fast_180 is equal to one, then a fault direction reversal is detected and confirmed at the earliest possible time. This means that the fault is located on the source side (local SSF) that is closest to that circuit breaker. Hence, a trip command is triggered for the associated circuit breaker to isolate the fault. Now the rest of the system is protected, the smallest possible area is isolated and the microgrid can operate normally without the faulted section.

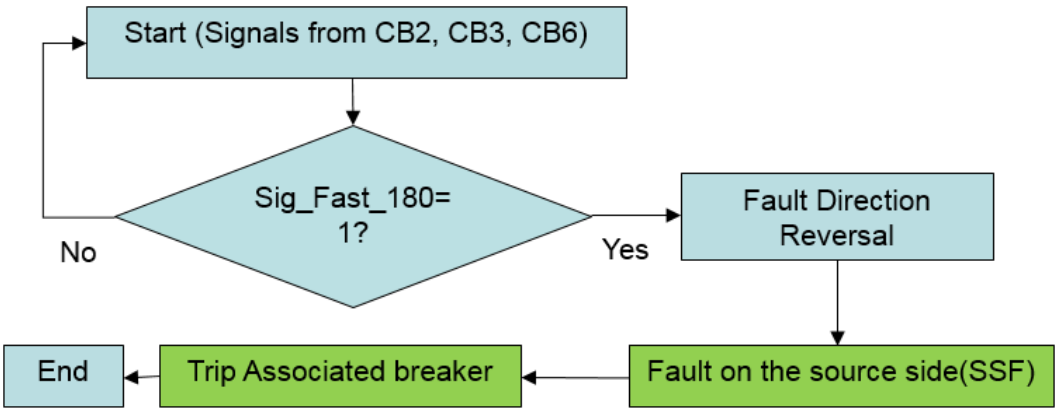


**Figure 3-6**. Algorithm A. for CB2, CB3, and CB6 to determine directional reversal.

### 3.4.2 Microgrid Side Faults (Algorithm B1)

This part of the algorithm determines whether the fault is on the busbar or not. When the fault is located on the busbar it is required to trip all circuit breakers to shut the microgrid down because a busbar fault impacts all sources. When the MGSF fault is a SSF on one of the other feeders, a ride through of the fault is performed locally to give the relay of the other feeder a chance to see the fault and trip its associated breaker according to Figure 3-6. The algorithm for this section is shown in Figure 3-7. This algorithm is processed in either the relay for CB6 or CB2. The relays for CB2, CB3, and CB6 are located adjacent to the busbar. Hence, the logic of these relays can be processed in one single relay because of the physical proximity which can make the coordination independent of the communication network. It is assumed here that the algorithm is processed in CB6. The algorithm is designed in a similar fashion when it is processed in CB2. In Figure 3-7, first signal Sig_Fast_90 is received from the logic found in Figure 3-5 but 90 degrees is the phase indicator of interest. If this signal is equal to 1, this means the current has switched from supplying real power to supplying reactive power. The associated CB sees the contribution of fault current coming from the inverter-based source and gives an indication that the fault is not on the source feeder closest to that breaker (not local SSF); because if it was, it will not see the 90 degree phase change but will see 180 degree that is indicative of direction reversal. The algorithm will then check whether the other breakers (CB3 and CB2) are still closed; because if they are still closed, it means that they have not seen a direction reversal (not SSF for other feeders), which means that the fault is on the busbar. A trip command will be sent to CB6 and signal sig is set to 1 to be sent to CB2 and CB3 for (Algorithm B2). If not both CB2 and CB3 are closed, meaning that one of them is open, that indicates there is a direction reversal fault (SFF on

one of the other feeders). This confirms that the fault is not on the busbar and there is no need to take any action locally for CB6 or other breakers that are not associated with this fault (not operating). This algorithm runs in parallel with algorithm A and B2 shown next.

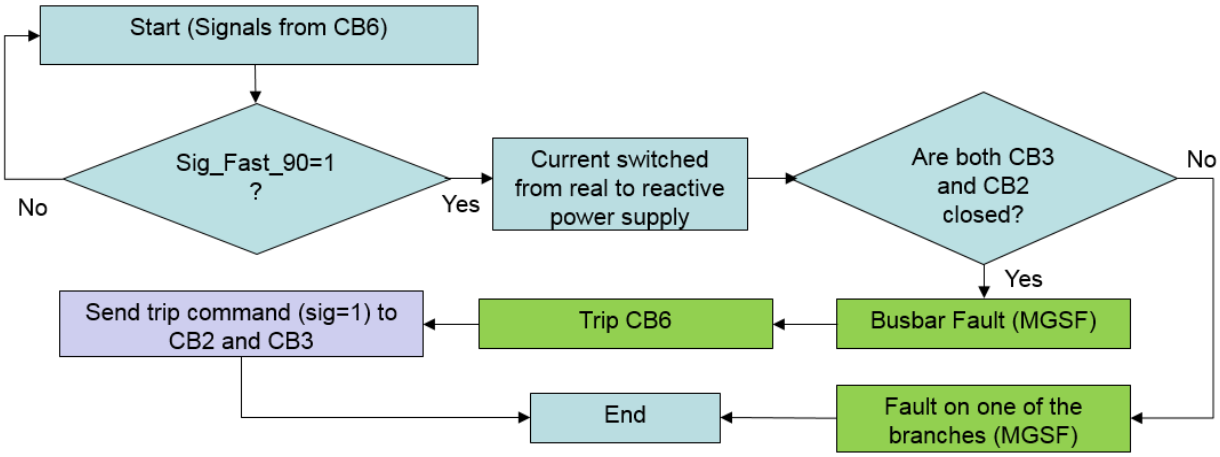


**Figure 3-7.** Algorithm B1 for CB6 and sends commands to CB2 and CB3

### 3.4.3 Microgrid Side Faults (Algorithm B2)

This part of the algorithm completes algorithm B1 as it receives the signal from algorithm B1 and processes it to perform the required action. Again, this part of the algorithm is designed based on the assumption that algorithm B1 is processed for CB6. Hence, this algorithm is implemented for both CB2 and CB3 and runs in parallel with A. The algorithm is shown in Figure 3-8. The algorithm simply receives signal sig and if this signal is equal to 1, it means that a fault is on the busbar. The algorithm then sends a trip command to the associated breaker. This concludes the whole protective coordination algorithm that is capable of isolating the smallest

possible faulted section while maintaining operation of other areas of the microgrid and protecting the system properly.

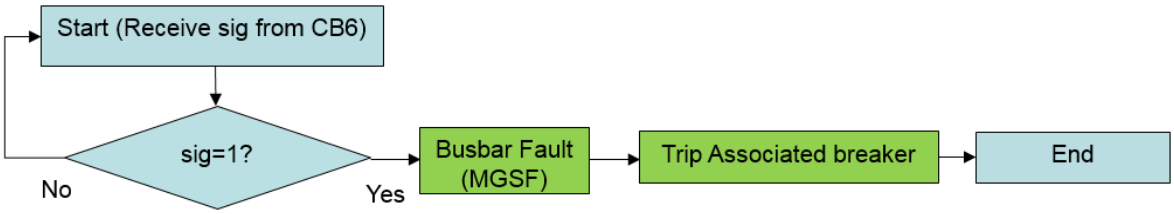


**Figure 3-8.** Algorithm B2 for CB2 and CB3

## 3.5 SIMULATION VALIDATION AND RESULTS

### 3.5.1 Validating One Unit at Constant and Varying Frequency

The phase unit of Figure 3-3 was validated at both constant and varying diesel generator output frequencies ranging from 0.1 Hz, as in Figure 3-9, to 5000 Hz. Figure 3-10 shows the phase change for a fault at F1 when the frequency varies as in Figure 3-9. The phase change was found in 7.4 ms using the rising edge and in 8.5 ms using the falling edge. Fault F1 shows a current direction reversal which is represented ideally by $180^0$ phase shift. However, in the simulation the result is approximately $150^0$ which is due to the line impedances in the system. Similarly, Figure 3-11 shows the phase change result for a fault at F2. The phase change was determined in 9.6 ms from rising edge and in 11.9 ms from falling edge.

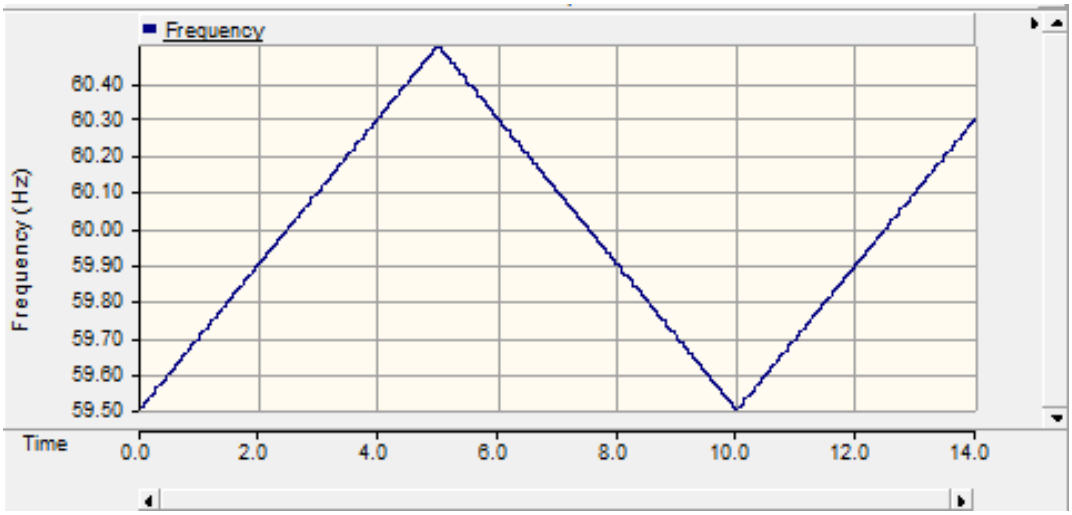


**Figure 3-9.** Varying frequency input for diesel generator

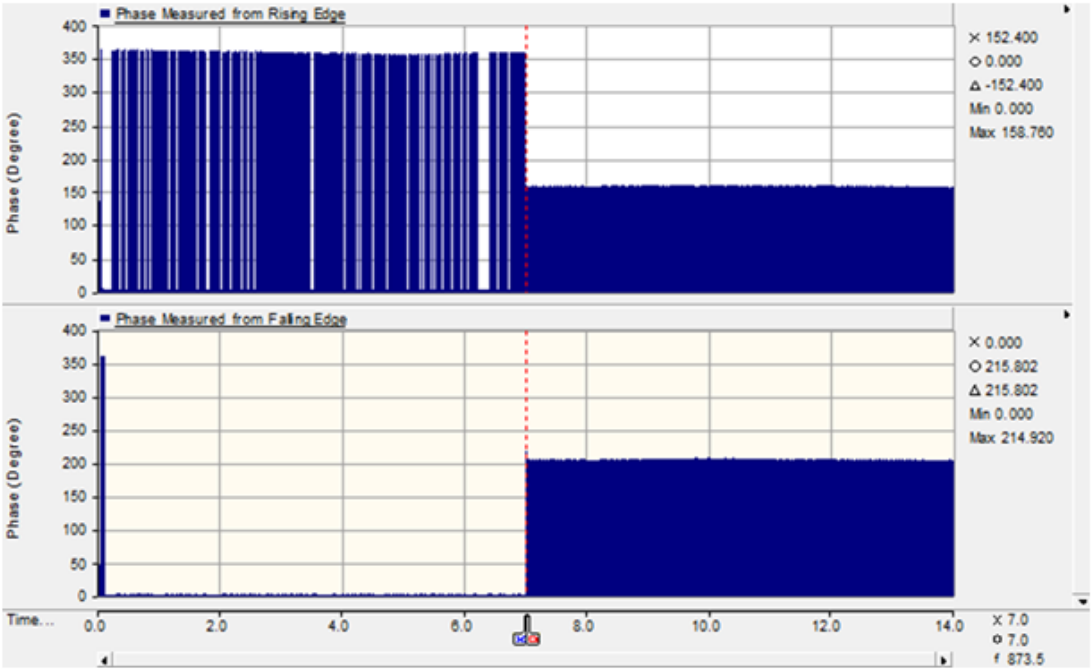


**Figure 3-10.** Output of rising edge unit for fault at F1 with varying frequency.

### 3.5.2 Validating All Units Using All references at Different Instants

It is critical to validate that the phase measurement produces satisfactory results when the fault occurs at different points on the wave. In this section, the performance of the phase unit of Figure 3-3 is shown when the fault occurs at different points on the wave. The desire is to confirm the phase measurement with a second measurement to make phase change detection more reliable. Thus, we investigate the signal closest to the fault vector that gives fastest detection and the signal that is the 2nd closest to that fault vector that gives the 2nd fastest detection.

The result of phase detection is shown in Table 3-1 and Table 3-2, for the instant at marker 'O' and the instant at marker 'X' of Figure 3-12, respectively. The unit showed promising results for the fastest and 2nd fastest signals. In Table 3-1, the fastest detection duration is 1.3 ms and the second fastest is 4.5 ms which is in line with our prediction of a maximum of 2.78 ms for the fastest signal as explained in section 3.3.1. Our results are faster than predicted because the solution depends on the point on wave at which the fault occurs and the phase deviation caused by the fault. When a second measurement is utilized for confirmation, the detection duration is within 5.54 ms. The results obtained for the second fastest was 4.5 ms which is within the maximum expected duration of 5.54 ms. Note that the speed of the apparatus could be increased if areas 2, 3 and 4 of Figure 3-2 are used. However, the focus is given only on area 1 here as only utilizing area 1 produced satisfactory results.

To validate that the units produce theoretically sound results, a fault is placed at F1, which is represented by IA_F in Figure 3-4. With the fact that the measurement is taken in the counter clockwise direction for area 1, we can predict theoretically which signal is supposed to

give the fastest and 2nd fastest detection. When the phase angle change is measured with all 6 voltage references in Figure 3-4 with respect to phase A current, it is anticipated that reference C and –B will give the fastest and 2nd fastest results, respectively. This expectation is demonstrated in simulation as shown in Table 3-1 and Table 3-2. For phase B current angle change detection, reference A and –C, give the fastest and second fastest, respectively, which is proven in simulation as shown in Table 3-1 and Table 3-2. For phase C current, references B and –A give the fastest and 2nd fastest, respectively, which is shown again in Table 3-1 and Table 3-2.

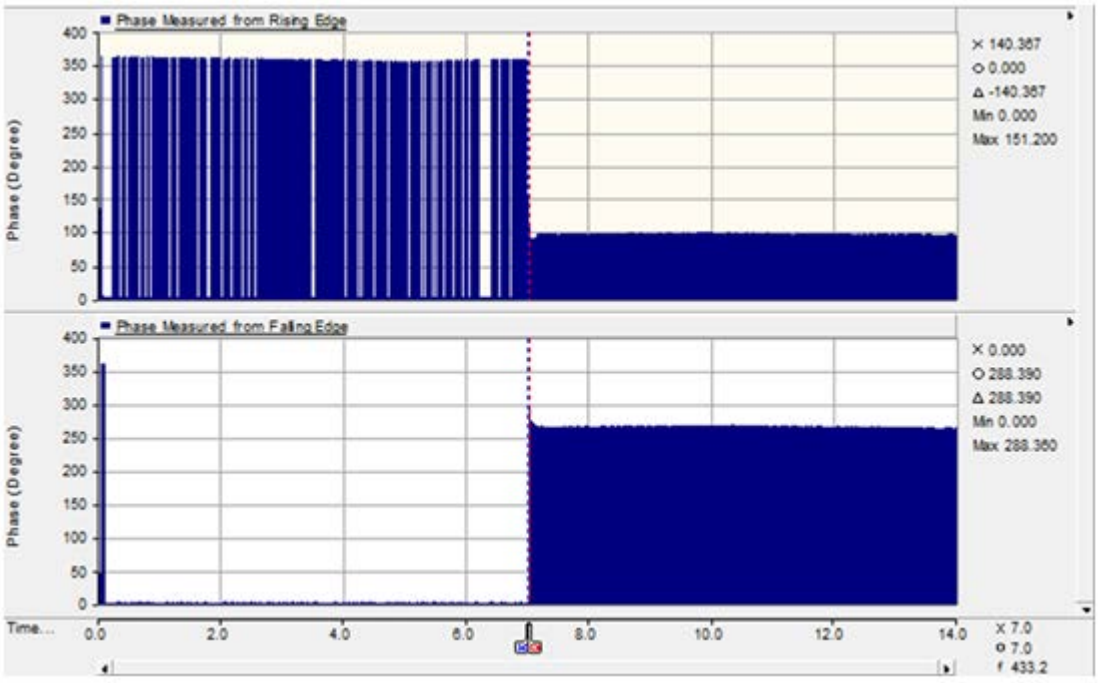


**Figure 3-11.** Output of rising edge unit for fault at F2 with varying frequency.

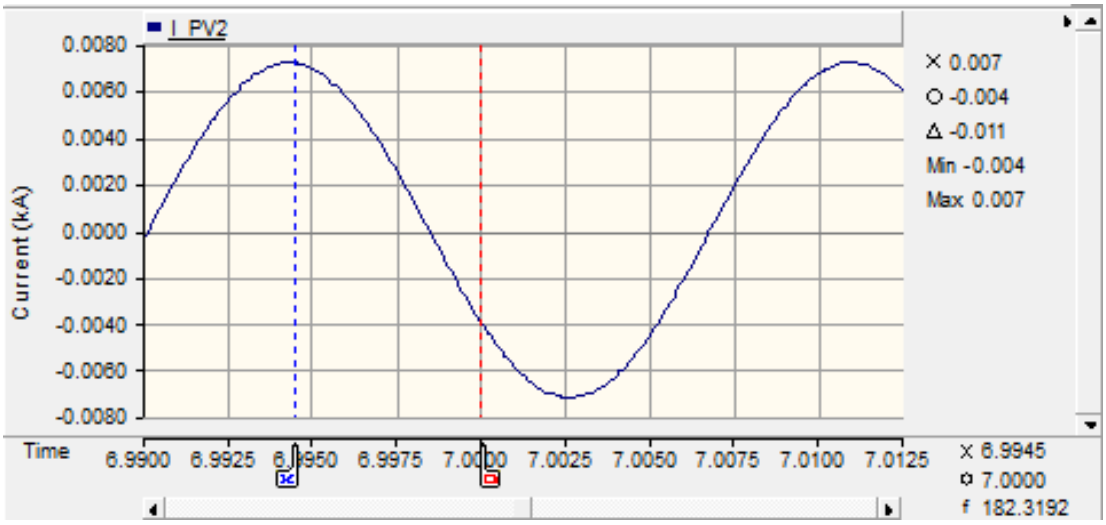


**Figure 3-12.** Fault instants marked at the current waveform.

**Table 3-1. Signals Giving the Quickest Phase Information for a 3-phase Fault F1 using Detection Area 1 at 7.00s**

| Phase of Current | V (Fastest) | Time (ms) | V (2nd Fastest) | Time (ms) |
|---|---|---|---|---|
| **A** | C | 1.300 | -B | 4.500 |
| **B** | A | 7.400 | -C | 10.19 |
| **C** | B | 13.00 | -A | 15.70 |

**Table 3-2. Signals Giving the Quickest Phase Information for a 3-phase Fault F1 using Detection Area 1 at 6.9945s**

| Phase of Current | V (Fastest) | Time (ms) | V (2nd Fastest) | Time (ms) |
|---|---|---|---|---|
| **A** | C | 7.300 | -B | 10.10 |
| **B** | A | 12.90 | -C | 15.60 |
| **C** | B | 1.200 | -A | 4.500 |

## 3.6 CONCLUSION

The goal of this chapter was to detect faults and determine the direction of fault current to perform protective coordination within an AC based microgrid in the presence of low fault currents due to inverter-based sources. Faults and their direction were detected by utilizing phase angle change of the phase difference between voltage and current as the main indicator. This was accomplished by designing a special phase measurement unit that can detect the phase change much faster than high speed directional relays in the market. It can detect a phase change within 2.78 ms if no confirmation signal is used and within 5.54 ms when a confirmation signal is used. This protection function is necessary in order to prevent nuisance tripping, blinding, slow tripping times, and to protect weak sources in the microgrid that could be otherwise be damaged if traditional high speed directional relays are used. The proposed method is able to isolate the smallest possible areas to protect the microgrid against faults while keeping unfaulted areas of the microgrid under operation. In general, the approach is general enough for other microgrid configurations and load placement locations.

It is critical here to note that this algorithm is only for showing how the fault current direction indicator described is useful for protective coordination of the AC circuit breakers in the microgrid. This approach will need to be modified to incorporate other protection requirements as for the case of low voltage ride through scenarios and IEEE 1547 mandates.

# 4.0 MODEL-BASED FAULT DETECTION OF INVERTER-BASED MICROGRIDS

In the previous chapter, the microgrid is assumed to have no load on its feeder and all the loads are only placed on the main bus. What if the load is placed on the feeder as shown in Figure 4-1? In this case if the current is normally flowing out of the feeder into the rest of microgrid (out of blue area into green area) and then reverses its direction, that does not necessarily indicate a fault. It could just be an increase in load that the local supply could not fully supply. Hence, we might face a difficulty distinguishing between a load increase in the feeder and fault in the feeder as shown in Figure 4-1. Therefore, a different fault detection approach is proposed here in order to cover wide system configurations. This approach is a model-based approach and can be coupled with the phase-based approach to make a more robust protection system. When faults occur in a microgrid feeder, the internal circuit structure changes significantly altering the system dynamic relationships. In this chapter, we exploit this concept and propose a model-based fault detection technique that works regardless of fault current levels. Here, different models describing a microgrid feeder under non-faulted and faulted conditions are derived. A communication-less approach is found to detect the status of the system with certainty under specific system constraints derived here. Besides the analytical proof of communication-less method, the performance of the proposed solution is demonstrated in the MATLAB/SIMULINK simulation environment.

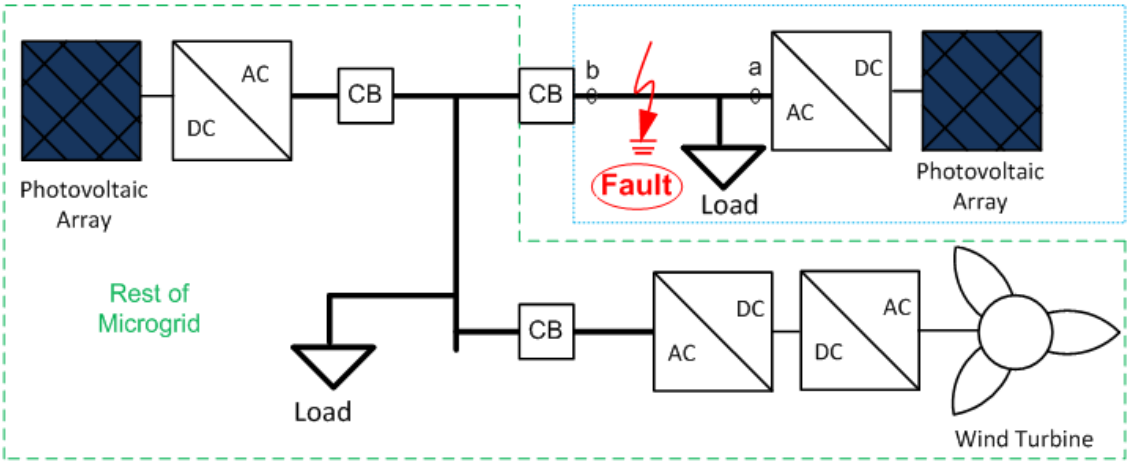


**Figure 4-1.** Inverter-based microgrid under study. CB refers to a circuit breaker. The dotted blue line represents a microgrid feeder.

## 4.1 INTRODUCTION

Protection is one of the most critical and challenging problems when it comes to microgrid systems. As mentioned before, the limited current contribution from inverter-based sources, the bi-directionality of power flow, the diversification of distributed energy resources (DERs), and the different modes of operation are the elements that cause difficulty in protecting microgrids [20], [58]. Traditional over-current protection is not a reliable method when it comes to protecting the microgrid due to lower available source currents resulting in longer trip times [20], [58]. Most methods in the literature depend on differential protection and a communication system in order to achieve this objective which can be slow and very costly [20], [31], [58]. Relying on communication degrades the reliability because the system becomes more prone to a single point of failure. Others have used sequence components, which fail in detecting balanced three-phase faults and are unreliable in the case of unbalanced conditions [31], [58]. Some have used data

mining approaches along with the differentials which are complex methods and also depend on communication [63]. The same is true for traveling wave based approaches [70], [71]. Wavelet analysis has been proposed in [73] and has not been validated. In [66], the authors have added a flywheel in the microgrid in order to boost fault currents and use traditional over-current protection. This method is costly and depends on the proper operation of the flywheel. A combination of different approaches has been proposed in [25] with differential protection as the main strategy. This method is costly and slow since it relies on other mechanisms as backup. In [114], the authors developed a method based on analyzing non-stationary differential signals using the Hilbert Huang Transform. This method is complex and suffers from unsatisfactory reliability and high cost due to the differential protection used. The authors in [115] used differential protection as a foundation and tried to improve it by using Hilbert space and fuzzy processes. This method still suffers from the same cost and reliability issues as pure differentials due to the use of differentials. In [116], the authors proposed a solution based on transient polarity comparison which is based on a wavelet transform but requires a central communication network.

In this chapter a novel communication-free fault detection method for inverter-based microgrids is proposed. The method can detect faults in the power transmission paths (feeders) of a microgrid (Figure 4-1) regardless of the fault current level and the mode of operation (islanded or grid-connected). The developed scheme will overcome the issue of low fault levels that may cause slow tripping times or prevent the microgrid protection from tripping at all. It will not use central communication to allow the protection system to operate faster, be more reliable, and be less costly. Microgrid fault detection cannot be based on voltage levels alone because renewables have to meet low-voltage and high-voltage ride through requirements specified in IEEE1547.

The rest of this chapter is organized as follows: In Section 4.2, the microgrid feeder model with different faulted and non-faulted conditions is given along with an explanation of the model-based fault detection approach. In Section 4.3, the mathematical proof of the ability to detect faults using one-sided measurement only (communication-less) will be provided and system constraints will be given. In Section 4.4, simulation results for the method using two-sided measurement (with communication) and the method using only one-sided measurement (no communication) will be provided. The simulation will demonstrate numerically that the proposed approach is able to distinguish between different conditions (faulted and non-faulted) in an inverter-dominated microgrid that produces low fault current levels. Section 4.5 concludes the chapter.

## 4.2 FEEDER MODELING AND FAULT DETECTION APPROACH

The major challenge of microgrid protection is that voltage and current levels alone cannot be used to detect faults. Hence, a method based on the structure (internal dynamics) of the microgrid is developed here. This approach is used because the circuit structure will change when a fault occurs within the microgrid. If we can identify the change in the internal system dynamics, we can detect faults. One approach to detect system changes is to have a prior knowledge of the possible system structures modeled as transfer functions, state-space descriptions or static models. Therefore, the different possible mathematical descriptions for different possible faulted conditions and a non-faulted condition must be derived. In the modeling process, the voltage of the system is treated as a system input and the current as a system output. Our methodology for identifying microgrid faults is depicted in Figure 4-2. The

communication-based approach utilizes two measurement locations at both ends of the transmission path (these occur at point *a* and point *b* in Figure 4-1) as inputs to the protection apparatus. The communication-free approach exploits only one measurement located at the microgrid side (point *b* only in Figure 4-1) as an input to the protection apparatus. For both approaches, each model produces an estimated current which is compared to the measured current in real-time. When there is a match between a measured current and an estimated current, there will be a clear distinction between a faulted condition and a non-faulted condition. This will lead to the successful detection of a fault despite the low-current levels that the inverter-based sources produce during faults.

For the communication-free approach, the error between measured and estimated current could be large. This might hinder the operation of the protection system which can be avoided under certain system constraints derived in section 4.3.

To perform the aforementioned approach, the different models for the non-faulted and faulted microgrid cases are derived in the appendix. These models are provided in a state-space format, from which sets of system transfer functions can be obtained, and can be used in the simulation. Three different state-space representations for various fault points within the studied microgrid and one model describing the system under normal operation are derived in the appendix to show that there is a clear distinction in the matrices for faulted and non-faulted conditions. The circuit representation of the microgrid feeder of Figure 4-1 (dotted blue line) and the fault locations are identified in Figure 4-3.

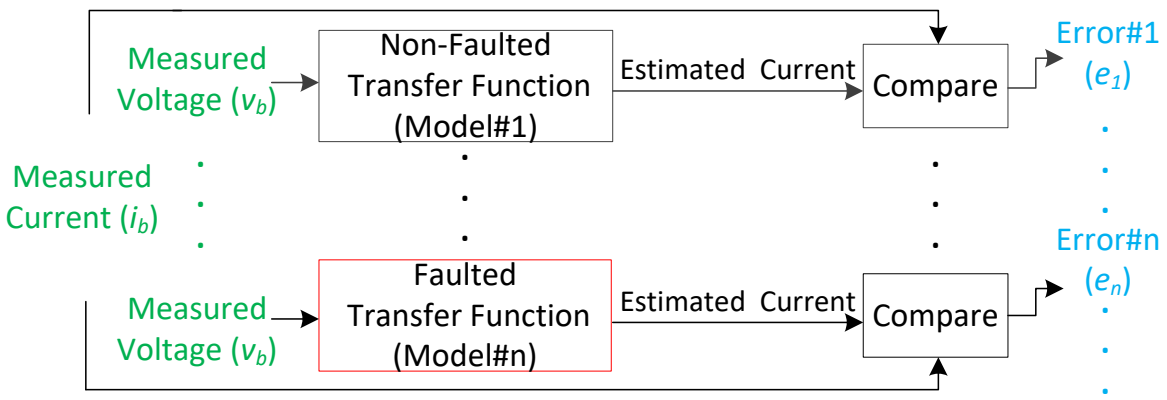


**Figure 4-2.** Microgrid fault-detection method.

If switch $S_{fC}$ is closed, this configuration corresponds to the case of a fault at the beginning of the feeder. If switch $S_{fB}$ is closed, this configuration corresponds to a fault near the system load. If switch $S_{fD}$ is closed, this configuration corresponds to a fault in the middle of the cable. Finally, if all switches are open, this case refers to normal operation of the microgrid.

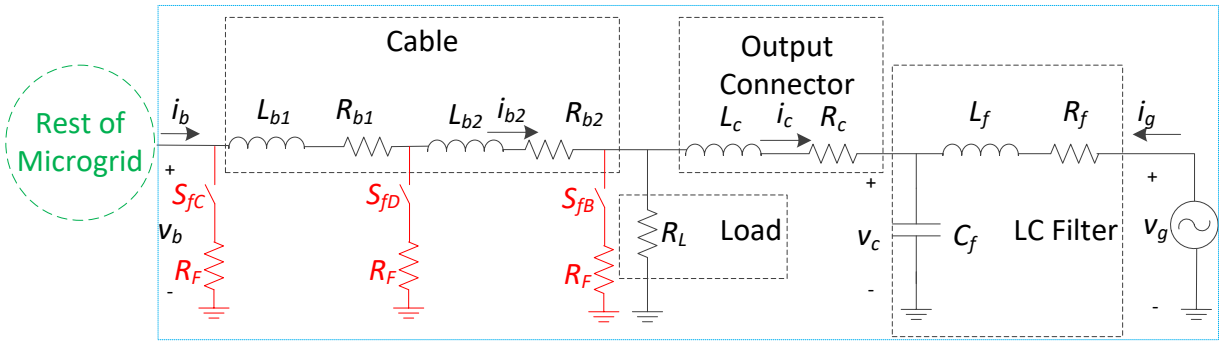


**Figure 4-3.** Microgrid feeder circuit during normal operation (switches OPEN) and during faulted conditions (specific switches CLOSED**).**

### 4.2.1 Nominal Feeder Model (Non-faulted)

Because our concern is to look at faults along the feeder of the system and not inside the inverter, the inverter and the renewable resource are modeled as a voltage source with filter and an output connector as shown in Figure 4-3. The dynamics of the microgrid feeder can be modeled in state-space form as in (4.1) and (4.2).

$$\dot{x} = Ax + Bu \tag{4.1}$$

$$y = Cx + Du \tag{4.2}$$

where the system states are

$$x = [i_b \quad i_{b2} \quad i_c \quad v_c \quad i_g]^T$$

$$\equiv [x_1 \quad x_2 \quad x_3 \quad x_4 \quad x_5]^T$$

and the input and output relationships are defined as

$$u = [v_b \quad v_g]^T$$

$$y = i_b = x_1.$$

Using circuit laws, the state-space matrices A, B, C, and D for the non-faulted condition can be shown to be (4.3), (4.4), (4.5) and (4.6), respectively. Note that ρ is chosen based on the inputs utilized, that is, ρ = 1 when there is communication and ρ = 0 when there is no communication.

$$A=\begin{bmatrix} -\frac{(R_b+R_L)}{L_b} & 0 & \frac{R_L}{L_b} & 0 & 0 \\ 0 & 0 & 0 & 0 & 0 \\ \frac{R_L}{L_c} & 0 & -\frac{(R_c+R_L)}{L_c} & -\frac{1}{L_c} & 0 \\ 0 & 0 & \frac{1}{C_f} & 0 & \frac{1}{C_f} \\ 0 & 0 & 0 & -\frac{1}{L_f} & -\frac{R_f}{L_f} \end{bmatrix} \tag{4.3}$$

$$B=\begin{bmatrix} \frac{1}{L_b} & 0 & 0 & 0 & 0 \\ 0 & 0 & 0 & 0 & \rho\frac{1}{L_f} \end{bmatrix}^T \tag{4.4}$$

$$C=\begin{bmatrix} 1 & 0 & 0 & 0 & 0 \end{bmatrix} \tag{4.5}$$

$$D=\begin{bmatrix} 0 & 0 \end{bmatrix} \tag{4.6}$$

where $Rb = Rb1 + Rb2$ and $Lb = Lb1 + Lb2$.

### 4.2.2 Faulted Feeder Model (Fault between Load and Cable)

Consider the case when the fault with impedance, $R_F$, occurs near the load within the microgrid depicted in Figure 4-3. Electrically, this is when switch $S_{fB}$ is closed. The state-space matrices *A*, *B*, *C*, and *D* for this faulted condition can be shown to be (4.7), (4.4), (4.5), and (4.6), respectively.

$$A = \begin{bmatrix} \frac{-(R_b+\gamma)}{L_b} & 0 & \frac{\gamma}{L_b} & 0 & 0 \\ 0 & 0 & 0 & 0 & 0 \\ \frac{\gamma}{L_c} & 0 & \frac{-(R_c+\gamma)}{L_c} & \frac{-1}{L_c} & 0 \\ 0 & 0 & \frac{1}{C_f} & 0 & \frac{1}{C_f} \\ 0 & 0 & 0 & \frac{-1}{L_f} & \frac{-R_f}{L_f} \end{bmatrix} \tag{4.7}$$

where,

$$\gamma = \frac{R_L R_F}{R_L + R_F}.$$

### 4.2.3 Faulted Feeder Model (Fault at Microgrid Side of Cable)

Consider the case when a fault occurs at the end of the feeder closest to the microgrid end of the architecture as shown in Figure 4-3. That is when $S_{fC}$ is closed. The state-space description for this condition can be expressed by (4.8), (4.9), (4.10), and (4.11):

$$A = \begin{bmatrix} 0 & 0 & 0 & 0 & 0 \\ 0 & \frac{-\gamma_1}{L_b} & \frac{R_L}{L_b} & 0 & 0 \\ 0 & \frac{R_L}{L_c} & \frac{-\gamma_2}{L_c} & \frac{-1}{L_c} & 0 \\ 0 & 0 & \frac{1}{C_f} & 0 & \frac{1}{C_f} \\ 0 & 0 & 0 & \frac{-1}{L_f} & \frac{-R_f}{L_f} \end{bmatrix} \tag{4.8}$$

$$B = \begin{bmatrix} 0 & \frac{1}{L_b} & 0 & 0 & 0 \\ 0 & 0 & 0 & 0 & \rho\frac{1}{L_f} \end{bmatrix}^T \tag{4.9}$$

$$C = \begin{bmatrix} 0 & 1 & 0 & 0 & 0 \end{bmatrix} \tag{4.10}$$

$$D = [\frac{1}{R_F} \quad 0] \tag{4.11}$$

where,

$$\gamma_1 = R_L + R_b$$

$$\gamma_2 = R_c + R_L .$$

### 4.2.4 Faulted Feeder Model (Fault in the Middle of Cable)

This condition corresponds to the scenario when $S_{fD}$ is closed. The state-space description for this scenario is described by (4.12), (4.13), (4.5), and (4.6):

$$A = \begin{bmatrix} \frac{-\gamma_3}{L_{b1}} & \frac{R_F}{L_{b1}} & 0 & 0 & 0 \\ \frac{R_F}{L_{b2}} & \frac{-\gamma_4}{L_{b2}} & \frac{R_L}{L_{b2}} & 0 & 0 \\ 0 & \frac{R_L}{L_c} & \frac{-\gamma_2}{L_c} & \frac{-1}{L_c} & 0 \\ 0 & 0 & \frac{1}{C_f} & 0 & \frac{1}{C_f} \\ 0 & 0 & 0 & \frac{-1}{L_f} & \frac{-R_f}{L_f} \end{bmatrix} \tag{4.12}$$

$$B = \begin{bmatrix} \frac{1}{L_{b1}} & 0 & 0 & 0 & 0 \\ 0 & 0 & 0 & 0 & \rho\frac{1}{L_f} \end{bmatrix}^T \tag{4.13}$$

where,

$$\gamma_3 = R_{b1} + R_F$$
$$\gamma_4 = (R_F + R_L + R_{b2}) .$$

This covers the wide range of fault locations on a feeder so that one set of dynamic relationships either matches one of the faulted conditions or is closest to one set compared to the others. For instance, when a fault occurs a distance away from the middle of the cable closer to the load, this condition should match the model described by (4.7) and neither the non-faulted model nor the other faulted models. A simulation case in Figure 4-8 has been shown to demonstrate that this is true.

Note that the system in each condition (non-faulted, and faulted conditions) can be represented in the s-domain as

$$i_b(s) = T(s) \cdot v_b(s) + T_g(s) \cdot v_g(s) \tag{4.14}$$

where *T(s)* is the transfer function resulting from the input $v_b$. *T(s)* can be derived by setting $\rho = 0$ and solving to obtain

$$T(s) = C(sI - A)^{-1}B + D \,. \tag{4.15}$$

and $T_g(s)$ is the transfer function resulting from the input $v_g$. The parameters *A*, *B*, *C*, and *D* are matrices corresponding to the state-space description derived above for each condition. Four different transfer functions, $T_n(s)$ (where $n$ = 1, 2, 3, and 4) are derived for the four different state space descriptions above which are used in the fault detection approach described in Figure 4-2.

## 4.3 ANALYTICAL ANALYSIS OF THE COMMUNICATION-FREE APPROACH FOR DETERMINING SYSTEM DESIGN CONSTRAINTS

Relying on communication is not desirable in protection systems because it degrades the reliability, slows protection operation and adds cost. This is why we investigate the effectiveness of a communication-free approach. Hence, we develop a mathematical proof showing that model-based fault detection works when only one measurement from the microgrid side is used under specific constraints.

To do so, we investigate the conditions upon which the fault identification method works when ignoring the source contribution ($i_g$), filter and output connector impedance at the end of the feeder. We ignore the source measurement ($i_g$ and $v_g$) because the source and the microgrid side measurements ( $i_b$, and $v_b$) are separated by cable with a specific length and would require the use of a communication channel to send the measurement information to the protection system if measurements on both ends are utilized. Hence, by ignoring the source, system fault identification can be communication-free. It is understood that the error between estimated system current and actual current will not be close to zero depending on the available $i_g$. However, we propose the following:

**Proposition 1**. The function giving the smallest error between the actual current and the estimated current describes the state of the system regardless of the size of error and regardless of the magnitude of $i_g$ for certain system constraints. This proposition is explained by the inequalities below:

1) For no fault: $|e_1| < |e_2|$ and $|e_1| < |e_3|$ and $|e_1| < |e_4|$

2) For ($S_{fB}$ closed): $|e_2| < |e_1|$ and $|e_2| < |e_3|$ and $|e_2| < |e_4|$

3) For ($S_{fC}$ closed): $|e_3| < |e_1|$ and $|e_3| < |e_2|$ and $|e_3| < |e_4|$

4) For ($S_{fD}$ closed): $|e_4| < |e_1|$ and $|e_4| < |e_2|$ and $|e_4| < |e_3|$

Note that $e_n$ is the error resulting from the difference between the measured value and the estimated output of transfer function $n$ which is derived from condition $n$ ($n$ = 1, 2, 3, and 4 for when all switches of Figure 4-3 are open, $S_{fB}$ is closed, $S_{fC}$ is closed, and $S_{fD}$ is closed, respectively). This error is calculated using the amplitude of the steady-state signal. The 1) - 4) inequalities in Proposition 1 show that the error associated with the transfer function describing the true dynamics of the system *must be lower* than any of the errors resulting from the remaining transfer functions with incorrect system dynamics for the given microgrid fault scenario in order to successfully detect the fault.

Before proceeding, it is important to note that according to our best knowledge the analysis in this section is a first attempt that analytically examines blinding and nuisance tripping scenarios giving clear indications of when they might occur based on system parameters. This is to allow for protection without the use of communication. Also, the analysis provided here

presents a general guideline that can be followed to include more faulted scenarios. Hence, this analysis procedure is general enough to be easily extended to *n* number of faults.

Observing matrices (4.3), (4.7), (4.8), and (4.12) in Section 4.2 for the different conditions of the system, we can see that there is a clear distinction between a non-faulted condition shown in (4.3) and the faulted conditions shown in (4.7), (4.8), and (4.12). This will be used as a basis to detect faults in the microgrid feeder regardless of fault current levels.

To prove Proposition 1 and find the system constraints guaranteeing its validity, we compare different mathematical relationships describing the system at different scenarios. To do so, we develop an impedance-based model for the non-faulted and faulted condition of the feeders as shown in Figure 4-4.

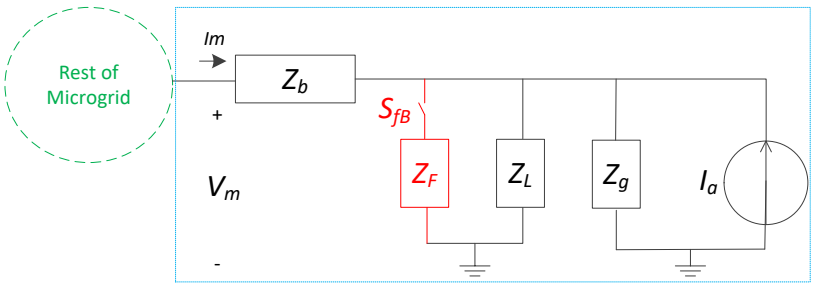


**Figure 4-4.** Equivalent impedance-based model for when all switches of Figure 4-3 are open (Normal operation) and during faulted condition between load and cable (SfB CLOSED).

Before proceeding, it is worth noting that the faulted condition used in this analysis is condition ($S_{fB}$ closed) only. Other conditions have not been explored because other conditions will give less restrictive constraints. The reason why condition ($S_{fB}$ closed) will give the most restrictive constraint is because the current contribution from the DER ($i_g$) for other conditions ($S_{fC}$ closed or $S_{fD}$ closed) will be lower than the current for condition ($S_{fB}$ closed). This is because

there is more impedance within the path for all faulted conditions compared to condition $S_{fB}$. Also, the other fault conditions make a significant alteration to the state-space matrix which is evident by inspecting (4.3), (4.8), and (4.12). Hence, faults are easier to detect even in the case of high-impedance faults. Being able to detect a wide range of faults for most conditions makes our communication-free model-based fault detection method strong.

In Figure 4-4, the distributed source, filter and output connector of Figure 4-3 are lumped into the Norton equivalent represented by $I_a$ and $Z_g$. Hence, during normal operation (Figure 4-4) the actual measured value of current magnitude, $|I_m|$, during a non-faulted condition is

$$| I_m^{NF} | = \left| \frac{(V_m - I_a (Z_L \backslash\backslash Z_g))}{Z_b + (Z_L \backslash\backslash Z_g)} \right| \tag{4.16}$$

where $Z_b$ is the impedance of the line and $Z_L$ is the load impedance. Note that $V_m$, $I_a$, $Z_L$, $Z_g$, $Z_b$, are all complex phasors. Note that the magnitude of power phasors are RMS values. In order to prove Proposition 1 and find the constraints upon which the proposition remains valid, we need to find a relationship describing the estimated current for when the current contribution ($I_a$) from the distributed generation is ignored. This condition is described by (4.17). Equation (4.17) is necessary in order to construct inequalities proving Proposition 1 and the reason for its necessity will be explained in further subsections:

$$| I_E^{NF} | = \left| \frac{V_m}{Z_b + Z_L} \right| . \tag{4.17}$$

Here $I_E^{NF}$ is defined as the estimate of the measured current for a non-faulted condition, $I_m^{NF}$. This estimate of the non-faulted condition could be the output of the transfer function derived from (4.3), (4.4), (4.5), and (4.6) if $v_g$ is treated as a disturbance (i.e $\rho = 0$ in the relationships found in Section 4.2). Throughout this chapter, we will use the subscript $E$ to

denote the value estimated by the model function and subscript *m* to denote the actual measured value.

For the case when a fault occurs between the load and cable ($S_{fB}$ closed in Figure 4-4) the current magnitude representing the actual measurement is defined by

$$| I_m^F |= \left| \frac{(V_m - I_a Z_{eq})}{Z_b + Z_{eq}} \right| \tag{4.18}$$

where

$$Z_{eq} = Z_L \backslash\backslash Z_F \backslash\backslash Z_g .$$

Note that $Z_{eq}$ is a complex phasor, and $Z_F=R_F$. The current estimate of the faulted condition when $S_{fB}$ is closed is described by

$$| I_E^F |= \left| \frac{V_m}{Z_b + (Z_L \backslash\backslash Z_F)} \right| . \tag{4.19}$$

Equations (4.16)-(4.19) will be used to prove Proposition 1 under specific system constraints. This is done by disproving all possible counter examples.

### 4.3.1 Analytical Analysis of Masked Fault Scenarios

The first counter example that will be analyzed here is a masked fault scenario. A masked fault (blinding scenario) is a fault in the system that has not been detected by the proposed, communication-free detection method. When we ignore the contribution of the DER, it is possible to get a masked fault due to the effects of the DER because the DER produces current

that we are not accounting for. A masked fault occurs when $|e_1| \leq |e_2|$ while the system is faulted. This scenario occurs when inequality (4.20) is satisfied:

$$\left| |I_m^F| - |I_E^{NF}| \right| \leq \left| |I_m^F| - |I_E^F| \right|. \tag{4.20}$$

Inequality (4.20) describes a condition when there is a fault in the system yet the model for the non-faulted case gives a smaller error than the model for the faulted case when compared to actual measurement. This leads to a masked fault condition. Solving (4.20) gives four distinct regions depending on the left hand side (LHS) and right hand side (RHS) sign of the expressions within the outside absolute value of (4.20) ($LHS = |I_m^F| - |I_E^{NF}|$ and $RHS = |I_m^F| - |I_E^F|$). The four distinct region analyses are as follow:

- *If* $LHS \geq 0$ *AND* $RHS \geq 0$

Here, (4.20) becomes

$$|I_m^F| - |I_E^{NF}| \leq |I_m^F| - |I_E^F|. \tag{4.21}$$

Solving (4.21) gives

$$\frac{1}{|Z_b + Z_L|} \geq \frac{1}{|Z_b + Z_L // Z_F|}. \tag{4.22}$$

Note the real and imaginary parts of $Z_b$, $Z_L$, and $Z_F$ are positive. Therefore, (4.22) is satisfied when (4.23) is satisfied.

$$|Z_L| < |Z_L \backslash\backslash Z_F| \tag{4.23}$$

Inequality (4.23) can never be satisfied implying that (4.22) is never satisfied. Thus, (4.21) is never satisfied. Hence, a masked fault never occurs within this region.

- *If* $LHS < 0$ *AND* $RHS < 0$

Here (4.20) becomes

$$| I_m^F | - | I_E^{NF} | \geq | I_m^F | - | I_E^F | . \tag{4.24}$$

Inequality (4.24) is always satisfied because (4.21) is never satisfied. Therefore, in order to know the conditions of the system giving a masked fault, we check the bounds of this region which is defined by (LHS < 0 and RHS < 0) as

$$| I_m^F | < | I_E^{NF} | \text{ and } | I_m^F | < | I_E^F | . \tag{4.25}$$

If one of the sides of (4.25) is dissatisfied then we are guaranteed that (12) is never satisfied because the two sides of (4.25) have to be satisfied simultaneously. Hence, we only investigate LHS<0 which is

$$| I_m^F | < | I_E^{NF} | . \tag{4.26}$$

Realize that $V_m$, and $I_a$ are complex quantities, and $|I_m|$ is the RMS signal. Substituting (4.17) and (4.18) into (4.26), simplifying and rearranging gives

$$\frac{| V_m - I_a Z_{eq} |}{| Z_b + Z_{eq} |} < \frac{| V_M |}{| Z_b + Z_L |} . \tag{4.27}$$

Our ultimate goal is to disprove all counterexamples or give as few and as relaxed constraints as possible to disprove all counterexamples. For the case if either side of (4.25) is prevented from being true (never operating in this region), we can guarantee that a masked fault never occurs. Hence, inequality (4.26) can be made to always be false so that (4.25) is never satisfied. This is done by performing an inequality reversal to force the system to always operate in the opposite region. Hence, the sign of (4.27) is redirected and we solve for an impedance ratio limit which is shown as Constraint 1:

**Constraint 1**: The inequality below must be satisfied to prevent a masked fault scenario:

$$\frac{|V_m - I_a Z_{eq}|}{|V_m|} \geq \frac{|Z_b + Z_{eq}|}{|Z_b + Z_L|} \tag{4.28}$$

Note that backup protection based on low-voltage (lower than IEEE1547 ride-through requirements) is assumed to always exist. Hence, $V_m$ in Constraint 1 is a constant quantity chosen above the backup protection value. Current $I_a$ should be as large as possible during faulted conditions which is typically 2 p.u. for inverters. Analyzing the microgrid according to (4.28), the range of fault impedances ($Z_F$) that the apparatus can detect can be determined. The constraint should be tested for the minimum and maximum possible values of $Z_L$. Constraint 1 represented by (4.28) provides the following physical insight: the ratio of the faulted system equivalent impedance to the non-faulted system equivalent impedance must be lower than the ratio of the voltage drop across the cable up to the fault point to the total voltage ($V_m$).

- *If LHS ≥ 0 AND RHS < 0*

Here (4.20) becomes

$$|I_m^F| - |I_E^{NF}| \leq -|I_m^F| + |I_E^F|. \tag{4.29}$$

Solving (4.29) does not give much physical insight. Hence, we reverse the inequality sign of (4.29) so that it is never satisfied and find a system constraint preventing a masked fault:

**Constraint 2.** The inequality below must be satisfied to prevent a masked fault scenario:

$$\frac{2|V_m - i_a Z_{eq}| \cdot |Z_b + Z_L|}{|V_m| \cdot |Z_b + Z_{eq}|} > \frac{|Z_b + Z_L|}{|Z_b + Z_L \backslash\backslash Z_F|} + 1 \tag{4.30}$$

Note that the result of $Z_F$ based on Constraint 1 can be substituted into Constraint 2 to make sure that (4.30) is true. If it is not, then $Z_F$ is lowered and the analysis process is repeated until (4.30) is satisfied. At the end of the iterations, the maximum value of $Z_F$ that the communication-free method can detect will be obtained. An optimization problem can also be formulated to find the optimal values.

- *If LHS < 0 AND RHS ≥ 0*

Here (4.20) becomes

$$|I_m^F| - |I_E^{NF}| \geq -|I_m^F| + |I_E^F|. \tag{4.31}$$

Solving (4.31) for when $Z_F = 0\ \Omega$ gives us a condition where it is always satisfied. Therefore, we check the system parameters that allow the system to operate in this region if this region exists for a general $Z_F$ (all possible types of faults - low and high impedance). This region (LHS < 0 and RHS ≥ 0) is expressed by

$$|I_m^F| < |I_E^{NF}| \text{ and } |I_m^F| \geq |I_E^F|. \tag{4.32}$$

By examining (4.32), we see that the left hand side of this equation is the same as (4.26). Equation (4.26) is forced to always be false by Constraint 1. Hence, (4.32) cannot be satisfied under Constraint 1. Therefore, a masked fault is impossible for this region.

### 4.3.2 Analytical Analysis of False Positive Scenarios

The only other counterexample that must be disproven to prove Proposition 1 to find all the constraints that guarantee its validity is a false positive (nuisance trip) scenario. A false positive

scenario occurs when there is no fault and we falsely identify a fault (i.e., when $|e_2| \leq |e_1|$ while there is no fault). This condition occurs when the following is satisfied:

$$\left| |I_m^{NF}| - |I_E^F| \right| \leq \left| |I_m^{NF}| - |I_E^{NF}| \right|. \tag{4.33}$$

Here, the LHS and RHS are redefined to be the expressions within the outside absolute value of (4.33) (i.e., $LHS = |I_m^{NF}| - |I_E^F|$ and $RHS = |I_m^{NF}| - |I_E^{NF}|$). Solving (4.33) gives four distinct regions as follows:

- *If* $LHS \geq 0$ *AND* $RHS \geq 0$

Here (4.33) becomes

$$|I_m^{NF}| - |I_E^F| \leq |I_m^{NF}| - |I_E^{NF}|. \tag{4.34}$$

Solving (4.34) gives

$$\frac{1}{|Z_b + Z_L // Z_F|} \geq \frac{1}{|Z_b + Z_L|}. \tag{4.35}$$

Inequality (4.35) is the same as (4.22) but with a reversed inequality sign and we concluded that (4.22) can never be satisfied. Hence, (4.35) is always satisfied. Therefore, if this region is entered, there is always a false positive. Hence, we check if it is possible to operate in this region or find the conditions that make the system operate within these boundaries. This region is expressed by

$$LHS \geq 0 \text{ and } RHS \geq 0 \tag{4.36}$$

Solving LHS $\geq 0$ of (4.36), we obtain

$$\frac{|V_M - I_a Z_{eq1}|}{|Z_b + Z_{eq1}|} \geq \frac{|V_m|}{|Z_b + Z_L \backslash\backslash Z_F|} \tag{4.37}$$

where,

$$Z_{eq1} = Z_L \,//\, Z_g . \tag{4.38}$$

Inequality (4.37) does not give much insight as to whether or not it is possible to operate in this region. Hence, we reverse the inequality sign of (4.37) so that (4.37) is never satisfied and find a system constraint (Constraint 3) preventing a false positive. Note that in Section 4.3.1 when we solve for the maximum value of $Z_F$, this gives us the value of the highest impedance for a fault on the system, which the apparatus can detect. However, in this section the analysis is for a false positive scenario, which means that there is no fault to begin with. Hence, the constraints here restrict the value of the assumed fault impedance in the model equations. However, when the range of the assumed fault resistance is decreased, this also decreases the range of faults that can be detected when faults occur. Hence, a tradeoff between protection system dependability (guaranteeing the relay always operates for faults) and security (guaranteeing the relay will not trip when there is no fault) is made. In protection system design, this tradeoff always exists [117] and the same is true for the proposed method. From Constraint 3, to make the protection system more secure, the fault impedance used in the model equations needs to be lowered. However, the more this impedance is lowered, the lower the range of fault impedances that can be detected in the communication-free approach (more security as opposed to more dependability). Hence, a thorough analysis has to be done by the designer to choose whether dependability versus security is valued most for a particular application. It is worth noting here that the communication-based approach is more robust in detecting a wide range of faults with a higher range of fault impedance.

**Constraint 3**. The fault impedance value used to calculate the equations must be such that the system satisfies the following constraint if security is desired over dependability:

$$\frac{|V_m - I_a Z_{eq1}|}{|V_m|} < \frac{|Z_b + Z_{eq1}|}{|Z_b + Z_L \backslash\backslash Z_F|} \tag{4.39}$$

Note that here $V_m$ is chosen (for this section's constraints) based on the largest possible stable normal operating value (i.e $V_m$=1.10 p.u.) as opposed to the smallest faulted value for the previous section's (Section 4.3.1) constraints. This is because a nuisance trip means that we are operating normally as opposed to a faulted condition in a blinding scenario in 4.3.1. Also, the constraint is checked for the largest and smallest possible $I_a$ and $Z_L$ during normal operation.

- *If LHS < 0 AND RHS < 0*

Here (4.33) becomes

$$|I_m^{NF}| - |I_E^F| \geq |I_m^{NF}| - |I_E^{NF}|. \tag{4.40}$$

Solving (4.40) gives

$$\frac{1}{|Z_b + Z_L|} \geq \frac{1}{|Z_b| + |Z_L // Z_F|}. \tag{4.41}$$

Inequality (4.41) is the same as equation (4.22) which was proven to never be satisfied in Section 4.3.1. Hence, (4.40) is never satisfied and a false positive can never occur in this region.

- *If LHS ≥ 0 AND RHS < 0*

In region (*LHS* ≥ 0 *AND RHS* ≥ 0) Constraint 3 has already been derived to prevent LHS of (4.33) ≥0 from occurring. This means we can never operate in this region under Constraint 3. Hence, a false positive can never occur in this region.

- *If LHS < 0 AND RHS ≥ 0*

Here (4.33) becomes

$$| I_m^{NF} | - | I_E^F | \geq - | I_m^{NF} | + | I_E^{NF} | . \tag{4.42}$$

Solving (4.42) yields

$$2\frac{|V_m - I_a Z_{eq1}|}{|Z_b + Z_{eq1}|} - \frac{|V_m|}{|Z_b + Z_L // Z_F|} \geq \frac{|V_m|}{|Z_b + Z_L|} \tag{4.43}$$

Inspecting (4.43) does not provide much insight into a system physical constraint. Hence, we investigate the region (LHS $< 0 \cap$ RHS $\geq 0$) to get insight into the possibility of a false positive.

First, LHS < 0 of (4.33) is solved to obtain

$$\frac{|V_m - I_a Z_{eq1}|}{|Z_b + Z_{eq1}|} < \frac{|V_m|}{|Z_b + Z_L \backslash\backslash Z_F|}. \tag{4.44}$$

Then, RHS ≥ 0 of (4.33) is solved to achieve

$$\frac{|V_m - I_a Z_{eq1}|}{|Z_b + Z_{eq1}|} \geq \frac{|V_m|}{|Z_b + Z_L|}. \tag{4.45}$$

Here, we try to use all possible equations (4.43), (4.44), and (4.45) to give multiple sufficient conditions guaranteeing the prevention of a false positive. We do this to give more room for $Z_F$ to increase in order to increase dependability while keeping the same level of security.

If one of the inequalities of (4.43), (4.44), or (4.45) is reversed then a false positive can never occur. However, (4.44) cannot be reversed to prevent a false positive because that will violate Constraint 3 developed in (4.39). Hence, the system must satisfy one of the equations listed as Constraint 4.

**Constraint 4**. One of the following conditions must be satisfied to prevent a false positive if security is desired over dependability:

$$2\frac{|V_m - I_a Z_{eq1}|}{|Z_b + Z_{eq1}|} - \frac{|V_m|}{|Z_b + Z_L \backslash\backslash Z_F|} < \frac{|V_m|}{|Z_b + Z_L|} \tag{4.46}$$

$$\frac{|V_m - I_a Z_{eq1}|}{|V_m|} < \frac{|Z_b + Z_{eq1}|}{|Z_b + Z_L|} \tag{4.47}$$

Note that the values derived from the previous constraints (Constraints 1-3) are checked against Constraint 4. If the constraint is satisfied, then the analysis procedure ends. If it is not, then the analysis is repeated until all constraints are satisfied or we can just set-up an optimization problem and solve it.

## 4.4 SIMULATION RESULTS

Here simulation results showing the performance of the proposed approach using communication (two sided measurements) is shown in order to validate the model. The results of the communication-free approach are also shown for different cases. The microgrid here is designed based on [47] which turned out to satisfy Constraints 1-4. Note that the error values are calculated from the p.u. RMS quantities. The top plots of all the figures demonstrate the effectiveness of the communication-based fault detection approach. The bottom plots of all the

figures demonstrate the effectiveness of the communication-free approach proved by the analysis of Section 4.3. The top graph of Figure 4-5 (between $t$ = 0 s to $t$ = 0.3 s) provides a validation of the model developed in the appendix for a non-faulted scenario (zero error). After $t$ = 0.3secs, the simulation results in Figure 4-5, Figure 4-6, and Figure 4-7 provide validations of the faulted models developed in the appendix for ($S_{fB}$ closed), ($S_{fD}$ closed), and ($S_{fC}$ closed), respectively, which is clear from the zero error results. The bottom plots demonstrate the validation of the inequalities in proposition 1.

Figure 4-7 demonstrates the effectiveness of the technique when a load is switched and a fault ($S_{fC}$ closed) is applied later in the simulation. Figure 4-8 shows the results when a fault $S_{fD}$ is applied at 20% of cable length (from load side) with a different fault resistance. This figure shows that the model matches the one described by ($S_{fB}$ closed) because this fault model is closest to this condition compared to the other fault model options.

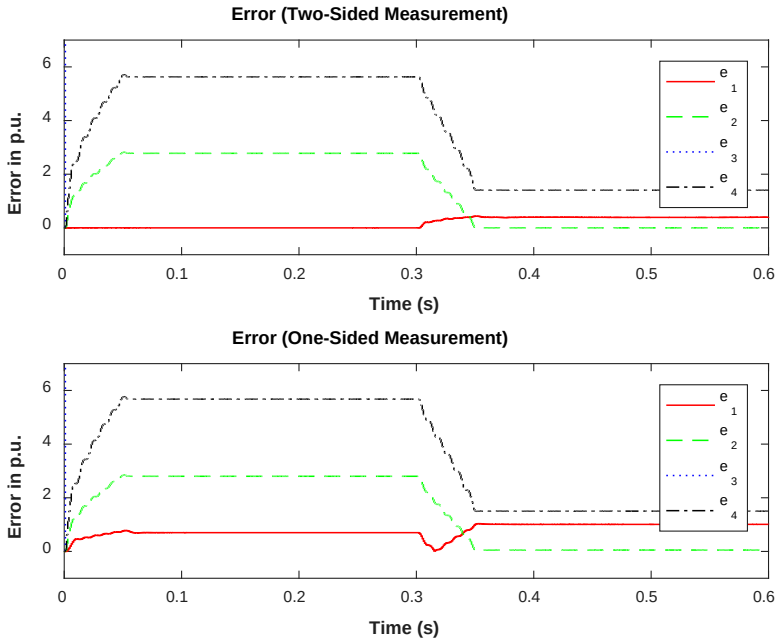


**Figure 4-5.** Results during normal operation and when a fault $S_{fB}$ is applied at 0.3 sec, $R_F = 0.01\ \Omega$. The dotted blue line reaches around 82 p.u. before 0.3 sec and around 40 p.u. after 0.3 sec (not shown).

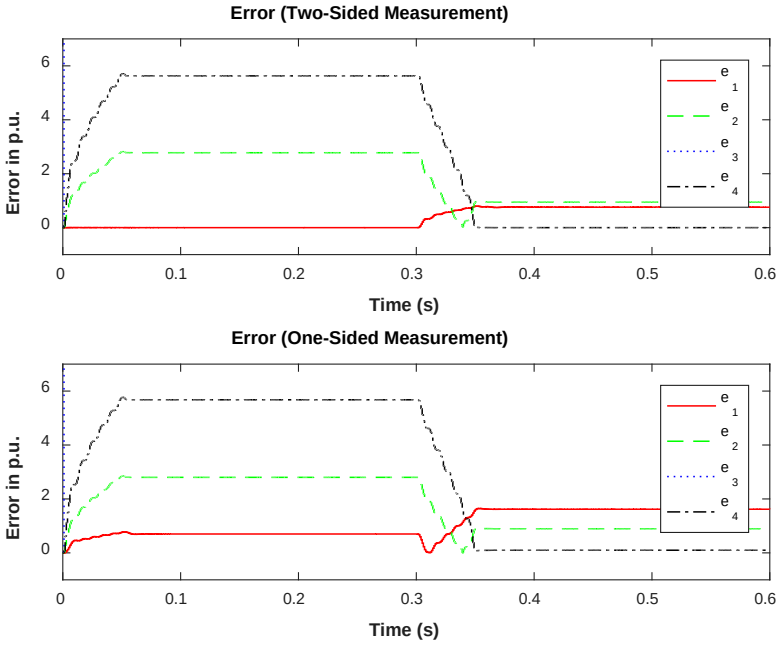


**Figure 4-6.** Results during normal operation and when a fault $S_{fD}$ is applied at 0.3 sec, $R_F = 0.01\ \Omega$. The dotted line reaches around 82 p.u. before 0.3 sec and around 20 p.u. after 0.3 sec (not shown).

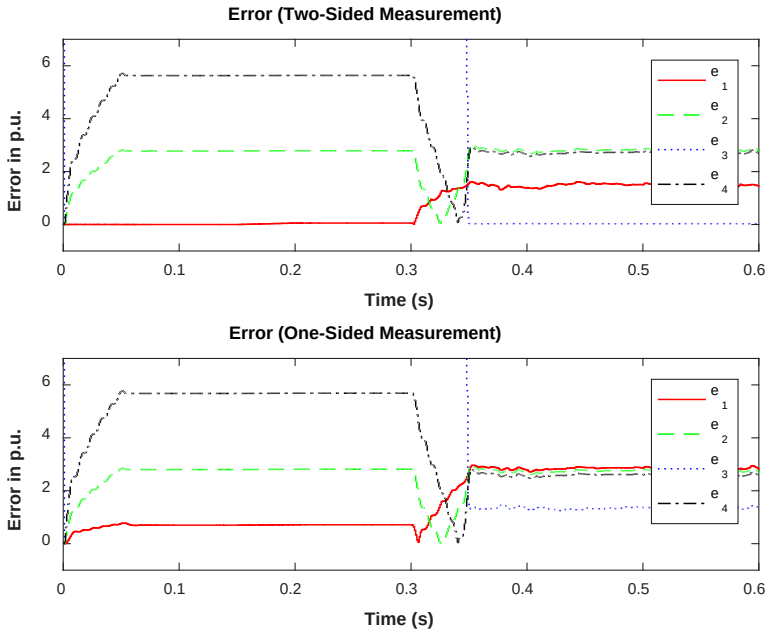


**Figure 4-7.** Results when Load ($R_L$ = 12 Ω) is switched at $t$ = 0.15 secs when a fault $S_{fC}$ is applied at 0.3 sec, $R_F$ = 0.01 Ω. The dotted blue line reaches around 82 p.u. before 0.3 sec (not shown).

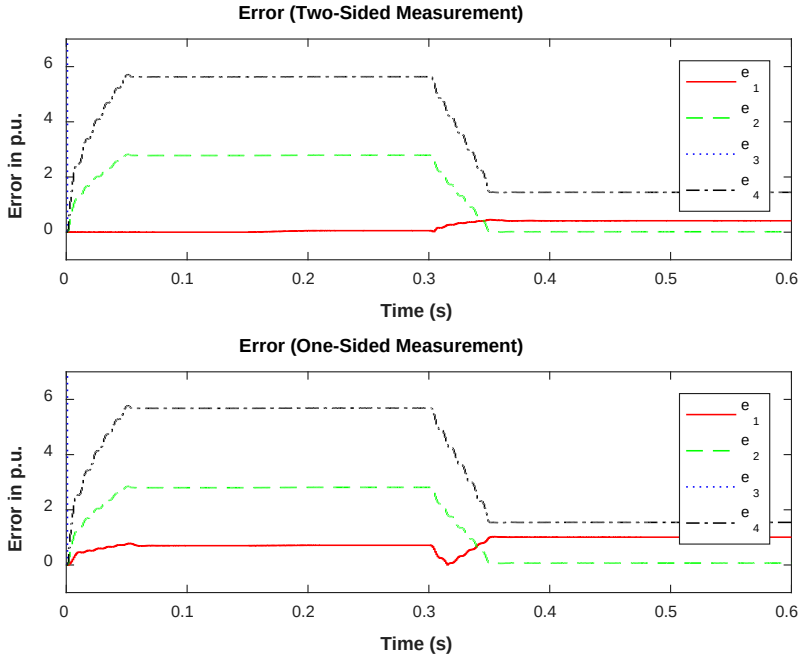


**Figure 4-8.** Results when a fault $S_{fD}$ at 20% of cable length is applied at 0.3 sec with $R_F$ = 0.04 Ω after load ($R_L$ = 12) is switched at $t$ = 0.15 secs. The dotted blue line reaches around 82 p.u. before 0.3 sec and around 40 p.u. after 0.3 sec (not shown).

## 4.5 CONCLUSION

This chapter provided models for different conditions (faulted and non-faulted) for a microgrid feeder. These models were developed and used in a model-based approach to detect faults in the case of low-fault current levels in inverter-dominated microgrids. To make the system more reliable, faults can be detected without introducing communication; a mathematical proof and system constraints are provided. The method developed in this chapter can easily distinguish between non-faulted and faulted conditions of microgrids regardless of fault current levels. This is because faults cause significant alterations to the governing system relationships. The proposed approach can be easily extended to other microgrid configurations. The faults are detected in steady-state here. However, the models developed in the appendix can serve as a basis to develop future methods that operate much faster by investigating the transient region for the model-based fault detection.

# 5.0 REDUCED-ORDER MODELING OF INVERTER BASED MICROGRIDS

The problem of fault detection mentioned in the previous chapters is not the only critical problem when it comes to facilitating the deployment of microgrids. An additional critical problem of microgrids is being able to stabilize and regulate (voltage and frequency) the system during normal operations and during disturbances. The reason why this is critical is that, a severe disturbance might cause the system's main parameters (voltage and frequency) to lose stability or fall below accepted deviations. Primary and secondary level controllers play a critical role in stabilizing the system after such disturbances. Hence, improving the design of primary and secondary level controllers of microgrids is of critical importance to microgrids' deployment. Many of the controller synthesis methods produce controllers of the same order as the model order. Hence, lower order models are desired to reduce the order of controllers. While this is true, the accuracy of the controller is dependent upon the accuracy of the model. In modeling of microgrids, there is always a compromise between accuracy and complexity as indicated by model order. Many of the currently available models found in the literature are reflective of system behavior but with high-order or less representative of system behavior with a low-order mathematical representation. In this chapter, a reduced order, linear, inverter based, microgrid model based on the *dq* reference frame is developed. The order of the model is 2*n* (for *n* distributed generators (DG)) lower than the least of the orders of models currently available. The

system representation includes the commonly neglected network dynamics and the interconnection coupling between DG units. Static and dynamic model equations are utilized to capture strong correlations between the linear, reduced order ($6n - 1$ states for $n$ DGs) model and non-linear system model in the transient (low frequency) and steady-state regions. The model developed is validated via a time domain simulation in the MATLAB/SIMULINK environment. The effect of the interconnection coupling between DGs on the eigenvalues is also presented.

## 5.1 INTRODUCTION

Microgrids are still in their early development stages resulting in many key challenges that must be addressed for widespread adoption and deployment. Critical concerns come in the form of microgrid stability and controller development. In order for researchers and engineers to tackle such challenges, appropriate microgrid dynamic models need to be determined to ease controller design and tuning.

The microgrid system is inherently a nonlinear system. To-date, researchers have linearized their chosen microgrid architecture model and developed small-signal, linear *dq* based models for stability analysis and control design [35], [118], [119]. Others have developed sequence component-based models for power flow analysis [120]. One of the most common control approaches to microgrids is hierarchal control [36]. In hierarchal control, there are three layers of control (primary, secondary, and tertiary). This hierarchy is due to the fact that each control layer has a different timescale with the primary being the fastest layer, next the secondary, and then the tertiary [36], [37], [42]. The main objective of the primary control is to

respond to fast changes to stabilize the system and to maintain proper load sharing between the generation units. The controllers used in this layer are usually the real power-frequency (P/f) droop controller and the reactive power-voltage (Q/V) droop controller [43], [44]. The objective of the secondary controller is to compensate for voltage and frequency deviation caused by the primary controller. This controller is slower than the primary, and many central and distributed control techniques have been proposed for this layer [36], [42], [45]–[47]. Finally, the main goal for the tertiary controller is optimal economic dispatch [36], [48], [49]. There is also another layer internal to the inverter, often associated with microgrid settings, which is sometimes called the zero-level layer. This layer consists of inner voltage and current controllers that have high-bandwidth.

It is well known that increasing the droop gain improves the power sharing capability between DG units but at the expense of voltage regulation which can cause instabilities [54], [121]. Hence, a need exists for better primary and secondary level controllers. In order to analyze, design, and tune secondary controllers, appropriate models have to be established and agreed upon. In many of the research articles to date, the full order model has been utilized [35]. However, this model is quite large consisting of 16 states per DG and makes using control design algorithms challenging due to the computational burden. Also, using this full-order model in control design could result in high-order controllers which are not desired in any control applications. Hence, a lower order model is needed, especially for secondary controller design purposes, which is still an active area of research [32].

Reduced models have been developed in many papers [40], [50]–[55]. A reduced order model including the dominant modes has been derived in [55]. Nevertheless, their model is for single-phase systems and excludes network dynamics. A reduced order model has been derived

in [113] using the well-known singular perturbation technique. Nonetheless, the model developed is suitable for stability analysis and is not well suited for secondary control design. The authors in [53] produced an effective low-order (15 state) model for a 2 DG microgrid system as opposed to a 36 state full order model. However, the work neglects the network dynamics. Their model also relies upon utilizing the operating point of the full-order model which can be hard to obtain.

Most of the reduced models use mathematical tools such as the singular perturbation technique to reduce the model and ignored the network dynamics. Ignoring the network dynamics is satisfactory for high-inertial systems but stability results may not be accurate for low-inertial microgrids [50], [52]. The authors in [52] attempted to include the network dynamics. However, they developed a phasor-based model and they ignored the coupling between DGs. The coupling between units could lead to other instabilities as well which will be shown later in this chapter. It is also more desirable that the reduced model be constructed in the conventional *dq* reference frame so that it captures the modes of interest for the control objectives of the secondary layer.

To do proper control design, a reduced order model is needed in order to design a low-order controller. This model must incorporate the modes of interest while incorporating the network dynamics and the coupling between units to show the interaction between the higher-level (primary and secondary) controllers. The challenge of incorporating the modes of interest, the network dynamics, and the coupling between DGs while still keeping the model order low and in *dq* frame is the focus of this chapter

The main contribution of this chapter is to develop a symbolic, reduced order, *dq* based dynamic model of inverter based microgrids. This new model utilizes fewer states and

accurately reflects the dynamics of a full order, detailed model compared to those found in the literature such as in [53]. The model developed can be used to conveniently investigate many issues such as controller design and tuning, parameter variations and robust stability analysis under parametric uncertainties. The system of interest is shown in Figure 5-1.

The model derived in this chapter is of the 6th order for each DG except the DG that is treated as a common reference, which is of the 5th order. For $n$ DGs, the order is $6n - 1$, which is less than the *dq* based reduced order models found in the literature. The least is 8 states per DG ($8n$ for $n$ DGs) [53]. The overall model was derived through a combination of static and dynamic model derivation, by ignoring fast states, and by algebraic manipulations. This model is derived based on the knowledge that the inner voltage controller, inner current controller, output filter and output connector are the modes that are fast. Hence, they are not relevant in the secondary controller design.

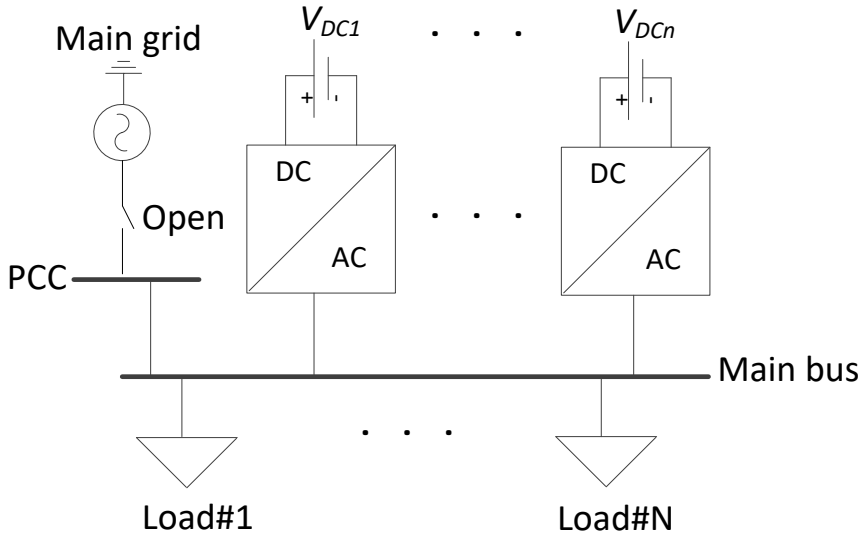


**Figure 5-1.** Microgrid configuration

The rest of this chapter is organized as follows: In Section 5.2, the full order model of a microgrid is explained. In Section 5.3, the *dq* based reduced-order nonlinear model is derived. In Section 5.4, the linearized reduced-order model is presented. In Section 5.5, model validation results are presented, and Section 5.6 concludes the chapter.

## 5.2 MODEL DESCRIPTION OF AC MICROGRID

The full order model of one DG unit apart of the microgrid is shown in Figure 5-2. The load is not shown in this model. However, in full order models the load is usually modeled as a resistor plus an inductor in parallel.

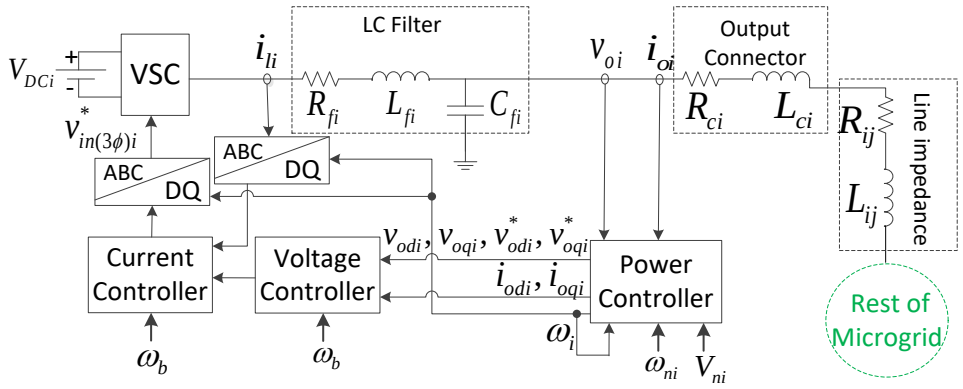


**Figure 5-2.** One DG full-order model**.**

The one DG unit shown in Figure 5-2 contains an LC filter, an output connector, a line impedance, a power controller, a voltage controller, and a current controller. The power controller stabilizes the system due to changes in loads and is responsible for real and reactive power sharing. The voltage controller regulates the voltage according to the voltage set-point acquired by the droop controller. The current controller regulates the current according to the set point set by the voltage controller. The current controller produces the modulation index

processed in the pulse width modulator (PWM), which produces the switching commands for the VSC switches. The power controller block is shown in Section 5.2.1. The inner voltage and current controllers are PI controller based with feedforward compensation terms. The inner controller models are developed based [35] an shown in Sections 5.2.2 and 5.2.3.

### 5.2.1 Power Controller

The power controller, which is implemented in MATLAB/SIMULINK, is shown in Figure 5-3. The frequency droop controller and voltage droop controller can be expressed as

$$\omega_i = \omega_n - m_{pi} P_i \tag{5.5}$$

$$v^*_{o,magi} = V_{ni} - n_{Qi} Q_i , \tag{5.6}$$

respectively, where $\omega_i$ is the angular frequency reference generated by the droop and sent to the ith inverter. $\omega_n$ is the primary control angular frequency reference value set as the nominal value or acquired from a secondary controller if secondary control is implemented, $m_{pi}$ is the frequency-power droop gain for the ith DG, and $P_i$ is the measured active power at the ith DG terminal. $v^*_{o,magi}$ is the reference voltage generated by the droop at the ith DG and sent to the inner voltage control loop. $V_{ni}$ is the primary control voltage reference value acquired from the secondary controller or set as the nominal. $n_{Qi}$ is the voltage-reactive power droop gain for the ith DG. $Q_i$ is the reactive power measured at ith DG output.

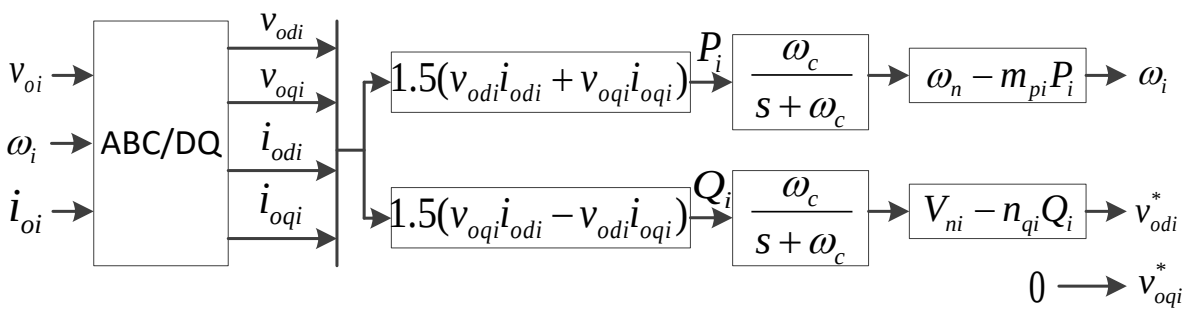


**Figure 5-3.** Power Controller

One of the DGs' reference frame is treated as the common reference frame with a rotating frequency $\omega_{com}$. The angle of the ith DG reference frame with respect to the common reference frame satisfies

$$\dot{\delta} = \omega_i - \omega_{com}. \tag{5.7}$$

The differential equations of the power controller can be written as

$$\dot{P}_i = -\omega_c P_i + \frac{3}{2}\omega_c (v_{odi} i_{odi} + v_{oqi} i_{oqi}) \tag{5.8}$$

$$\dot{Q}_i = -\omega_c Q_i + \frac{3}{2}\omega_c (v_{oqi} i_{odi} - v_{odi} i_{oqi}), \tag{5.9}$$

where $v_{odi}$, $v_{oqi}$, $i_{odi}$, and $i_{oqi}$ are the direct and quadrature voltage and current outputs of the ith DG, respectively.

The controller is designed such that the output voltage magnitude reference is aligned with the d-axis and the q-axis is set to zero as follows:

$$v^*_{odi} = V_{ni} - n_{Qi} Q_i, \quad v^*_{oqi} = 0. \tag{5.10}$$

### 5.2.2 Voltage Controller

The voltage controller is part of the zero-level control internal to the inverter. The one used here which is implemented in SIMULINK is shown in Figure 5-4. The dynamic algebraic differential equations of the voltage controller is as follow:

$$\dot{\phi}_{di} = v^*_{odi} - v_{odi} \tag{5.11}$$

$$\dot{\phi}_{qi} = v^*_{oqi} - v_{oqi} \tag{5.12}$$

$$i^*_{ldi} = F_i i_{odi} - \omega_b C_{fi} v_{oqi} + K_{pv}(v^*_{odi} - v_{odi}) + K_{iv}\phi_{di} \tag{5.13}$$

$$i^*_{lqi} = F_i i_{oqi} + \omega_b C_{fi} v_{odi} + K_{pv}(v^*_{oqi} - v_{oqi}) + K_{iv}\phi_{qi} \tag{5.14}$$

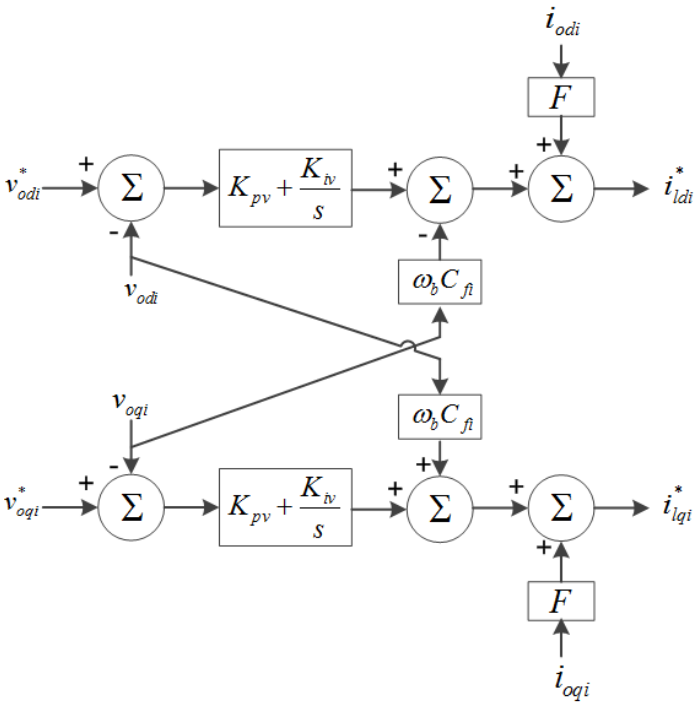


**Figure 5-4.** Inner Voltage Controller

### 5.2.3 Current Controller

The current controller is part of the zero-level control internal to the inverter. The one used here which is implemented in SIMULINK is shown in Figure 5-5. The dynamic differential algebraic equations are as follow:

$$\dot{\gamma}_{di} = i^*_{ldi} - i_{ldi} \tag{5.15}$$

$$\dot{\gamma}_{qi} = i^*_{lqi} - i_{lqi} \tag{5.16}$$

$$v^*_{idi} = -\omega_b L_{fi} i_{lqi} + K_{pc}(i^*_{ldi} - i_{ldi}) + K_{ic}\gamma_{di} \tag{5.17}$$

$$v^*_{iqi} = \omega_b L_{fi} i_{ldi} + K_{pc}(i^*_{lqi} - i_{lqi}) + K_{ic}\gamma_{qi}. \tag{5.18}$$

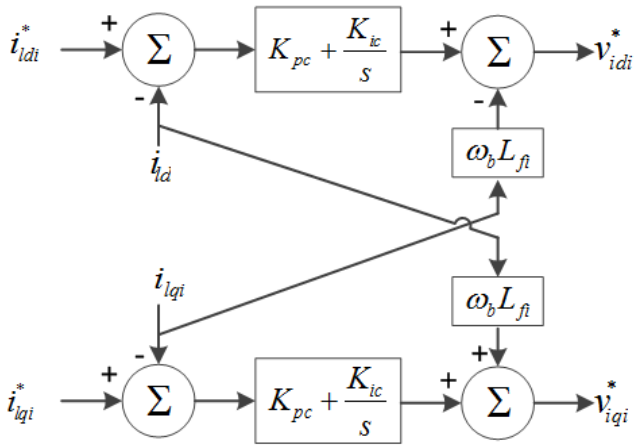


**Figure 5-5.** Inner Current Controller

## 5.3 DERIVATION OF THE DQ BASED NONLINEAR REDUCED-ORDER MODEL

As mentioned in the introduction, there is a need for low-order models in the *dq* reference frame. In this modeling effort, we will use our knowledge of the circuit and the controllers in the voltage source converter (VSC) to produce a reduced order model that accurately captures the important dynamics of the system for secondary or primary level controller design or tuning. It has been well-established in the literature through comprehensive eigenvalue analysis that the dominant modes of the microgrid are those associated with the droop controller; and increasing the droop controller gain could make the system unstable depending on the loading conditions [35], [50], [55], [122]. Hence, the equations for the droop controllers are kept in the reduced-order model and voltage and current controller equations are neglected.

In addition, most VSC units lock the phase *A* voltage to the *d*-axis which makes $v_{oq} = 0$. Hence, further reduction is achieved here by ignoring the *q* component of the voltage signal. The network dynamics are preserved here and they are lumped with the output connector to add the static influence of the connector. The filter dynamics are ignored, but the static influence of the filter is kept along with the capacitor state for further model accuracy. The filter capacitors are needed when the inverters are used for voltage and frequency regulation [53]. The capacitor state of the filter is necessary in order to define the output voltage of the converter with respect to a state. The coupling between DGs is shown by treating the load as static (because the load dynamics are fast) and using Kirchhoff Current Law (KCL) to couple the units differential equations at the main bus. By incorporating the dynamic influence of the dominant modes and the static influence of the fast modes, the derived model becomes very accurate, retains coupling between controllers and the DGs, and is useful for controller design and tuning.

### 5.3.1 Derivation of the Reduced-Order VSC Controller Model

According to [35], [53], the voltage and current controller are fast modes of the system and can be reasonably ignored. Hence, the controller for this reduced-order model is only the power controller with the measurement filter depicted in Figure 5-3. Therefore, $v^*_{in(3\phi)i} \equiv v^*_{oi}$.

In order to derive the equations of the reduced model, we start with the droop controller equations as follows:

$$v^*_{oi} = V_{ni} - n_{qi}Q_i \tag{5.19}$$

$$\omega_i = \omega_{ni} - m_{pi}P_i \tag{5.20}$$

where $V_{ni}$ is the voltage set point, $n_{qi}$ the voltage-reactive power droop gain, $Q_i$ the measured reactive power, $v_{oi}{}^*$ the voltage reference sent to the inner controllers for the $i$th DG, $\omega_{ni}$ the angular frequency set point, $m_{pi}$ the frequency-real power droop gain, $P_i$ the measured real power, and $\omega_i$ the angular frequency reference for the $i$th DG. Assuming perfect alignment of phase $A$ voltage to the $d$-axis (i.e $v^*_{oqi} = 0$), the droop equation becomes

$$v^*_{odi} = V_{ni} - n_{qi}Q_i\,. \tag{5.21}$$

This assumption is safe because this type of alignment is common in microgrid control [35], [47].

The instantaneous real and reactive powers are calculated from measured voltages and currents. Hence,

$$\hat{p}_i = \frac{3}{2}(v_{odi}i_{odi} + v_{oqi}i_{oqi}) \tag{5.22}$$

$$\hat{q}_i = \frac{3}{2}(v_{oqi} i_{odi} - v_{odi} i_{oqi}) \tag{5.23}$$

where $v_{odi}$ and $v_{oqi}$ are voltages in the *d* and *q* axes, respectively for the *i*th DG, and $i_{odi}$ and $i_{oqi}$ are the *i*th DG currents in the *d* and *q* axes, respectively.

The power is filtered before being sent to the droop controller. Hence, the measured power in the frequency domain becomes

$$P_i = \frac{\omega_c}{s + \omega_c} \hat{p}_i \tag{5.24}$$

$$Q_i = \frac{\omega_c}{s + \omega_c} \hat{q}_i \tag{5.25}$$

where $\omega_c$ is the angular frequency of the measurement filter. The measured real and reactive power in time domain is then given by

$$\dot{P}_i = -\omega_c P_i + \frac{3}{2}\omega_c (v_{odi} i_{odi} + v_{oqi} i_{oqi}) \tag{5.26}$$

$$\dot{Q}_i = -\omega_c Q_i + \frac{3}{2}\omega_c (v_{oqi} i_{odi} - v_{odi} i_{oqi}). \tag{5.27}$$

Assuming the inner controllers are fast enough and establish $v_{oqi} = 0$, the measured real and reactive power become

$$\dot{P}_i = -\omega_c P_i + \frac{3}{2}\omega_c v_{odi} i_{odi} \tag{5.28}$$

$$\dot{Q}_i = -\omega_c Q_i - \frac{3}{2}\omega_c v_{odi} i_{oqi}. \tag{5.29}$$

As shown from (5.28) and (5.29), we have utilized the fact that the inner controllers are fast and the voltage alignment to the *d*-axis perfectly allowing the expressions to simplify greatly. These

assumptions will be used throughout the derivation to arrive at the lowest order and simplest dynamic model under investigation.

### 5.3.2 Derivation of the Reduced-Order Circuit Model

Here, we neglect fast circuit dynamics and keep only the slow modes along with some of the fast modes that are absolutely necessary to capture important effects in the system. Static values of the circuit are also kept to produce accurate results and to capture coupling between important modes. First, we know that the output filter and connector are fast modes of the system [35], [53]. Hence, they can be ignored. However, the static values of these two elements have to be kept to produce accurate results. The network dynamics (cable dynamics) are essential although they are fast because they can cause instabilities in the slow modes [52] and also play a part in capturing the coupling between the DGs. Here, since we are keeping the network dynamics, we can add the connector parameters to the cable values for stronger accuracy between the detailed system model and reduced-order model. The connector and cable parameters can be added together because they are in series. In addition, secondary and primary level controller design is concerned with voltage and frequency regulation. Therefore, the output capacitor of the filter cannot be ignored [53]. Along with these assumptions, the load dynamics are fast and can be ignored [35]. However, their static influence is necessary for accurate results and is also necessary to capture the coupling between DGs. The circuit structure of a 2-DG microgrid after reduction is depicted in Figure 5-6.

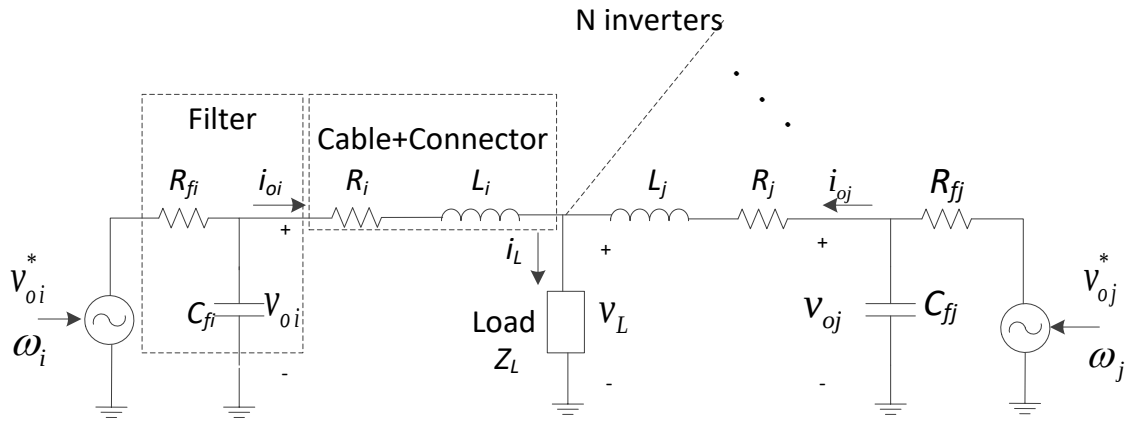


**Figure 5-6.** Two-DG reduced-order circuit model.

In Figure 5-6., $v^*_{oi}$ is the three-phase reference voltage signal generated by the inverter. This signal results from converting $v^*_{odi}$ and $v^*_{oqi}$ in Figure 5-3 to a three-phase unit utilizing the frequency produced by the (P/f) droop controller. The *d*-axis and *q*-axis equivalent circuit model of the left DG (the *i*th DG) is shown in Figure 5-7 and Figure 5-8, respectively.

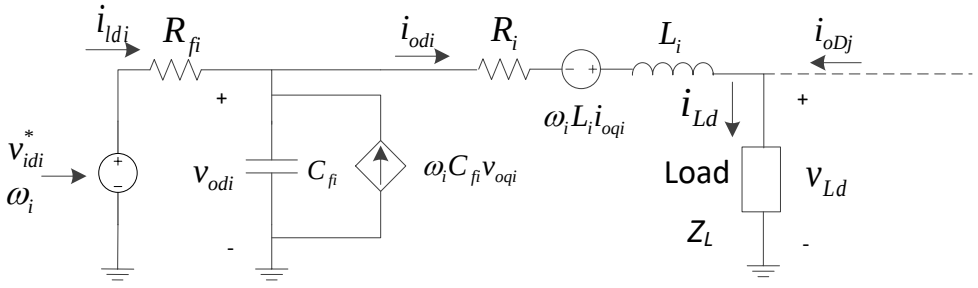


**Figure 5-7**. d-axis of the circuit for DGi.

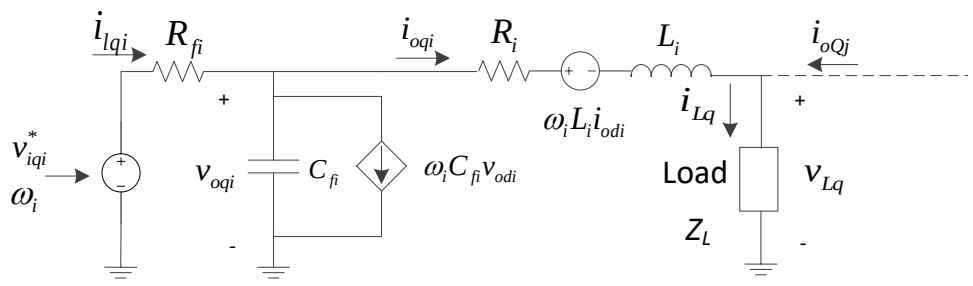


**Figure 5-8.** q-axis of the circuit for DGi.

By performing KVL on the circuits of Figure 5-7 and Figure 5-8, we arrive at

$$\dot{i}_{di} = \frac{1}{L_i} v_{odi} - \frac{R_i}{L_i} i_{odi} + \omega_i i_{oqi} - \frac{1}{L_i} v_{Ld} \tag{5.30}$$

$$\dot{i}_{qi} = \frac{1}{L_i} v_{oqi} - \frac{R_i}{L_i} i_{oqi} - \omega_i i_{odi} - \frac{1}{L_i} v_{Lq} \tag{5.31}$$

where $L_i$ and $R_i$ are the inductance and resistance of the sum of the cable and connector at the $i$th DG, respectively; $v_{Ld}$ and $v_{Lq}$ are the $d$ and $q$ component voltages at the load point, respectively. By performing KCL at the load point in Figure 5-7 and Figure 5-8, we arrive at

$$i_{Ld} = i_{odi} + i_{odj} \tag{5.32}$$

$$i_{Lq} = i_{oqi} + i_{oqj}. \tag{5.33}$$

where $i_{Ld}$ and $i_{Lq}$ are the $d$ and $q$ components of the load current, respectively.

The voltage at the load can be defined in terms of its own state and the state of the neighboring DG as

$$v_{Ld} = Z_L (i_{odi} + i_{odj}) \tag{5.34}$$

$$v_{Lq} = Z_L (i_{oqi} + i_{oqj}) \tag{5.35}$$

where $Z_L$ is the static value of the load. Here, we ignore the dynamics of the load because they are considered fast modes [35]. Nevertheless, the equivalent resistance value ($Z_L$) is necessary to capture accurate results. Substituting (5.34) and (5.35) into (5.30) and (5.31) and noting that $v_{oqi} = 0$, (5.30) and (5.31) become

$$\dot{i}_{odi} = \frac{1}{L_i} v_{odi} - (\frac{R_i}{L_i} + \frac{Z_L}{L_i}) i_{odi} + \omega_i i_{oqi} - \frac{Z_L}{L_i} i_{oDj} \tag{5.36}$$

$$\dot{i}_{oqi} = -(\frac{R_i}{L_i} + \frac{Z_L}{L_i}) i_{oqi} - \omega_i i_{odi} - \frac{Z_L}{L_i} i_{oQj}. \tag{5.37}$$

Substituting (5.20) into (5.36) and (5.37), we arrive at

$$\dot{i}_{odi} = \frac{1}{L_i} v_{odi} - (\frac{R_i}{L_i} + \frac{Z_L}{L_i}) i_{odi} + \omega_{ni} i_{oqi} - m_{pi} P_i i_{oqi} - \frac{Z_L}{L_i} i_{oDj} \tag{5.38}$$

$$\dot{i}_{oqi} = -(\frac{R_i}{L_i} + \frac{Z_L}{L_i}) i_{oqi} - \omega_{ni} i_{odi} + m_{pi} P_i i_{odi} - \frac{Z_L}{L_i} i_{oQj}. \tag{5.39}$$

Note that the upper case *Q* and *D* subscripts refer to the values in the global reference frame. Within (5.36)-(5.39), $i_{oDj}$ and $i_{oQj}$ are the *d* and *q* components of the *j*th DG, respectively, in the global reference frame. The states can be transformed from the local to global reference frame using

$$\begin{bmatrix} i_{oDj} \\ i_{oQj} \end{bmatrix} = \begin{bmatrix} \cos\delta_j & -\sin\delta_j \\ \sin\delta_j & \cos\delta_j \end{bmatrix} \begin{bmatrix} i_{odj} \\ i_{oqj} \end{bmatrix}. \tag{5.40}$$

Using (5.40), (5.38) and (5.39) become

$$\dot{i}_{odi} = \frac{1}{L_i} v_{odi} - (\frac{R_i + Z_L}{L_i}) i_{odi} + \omega_{ni} i_{oqi} - m_{pi} P_i i_{oqi} - \frac{Z_L}{L_i} \cos(\delta_j) i_{odj} + \frac{Z_L}{L_i} \sin(\delta_j) i_{oqj} \tag{5.41}$$

$$\dot{i}_{oqi} = -(\frac{R_i + Z_L}{L_i}) i_{oqi} - \omega_{ni} i_{odi} - m_{pi} P_i i_{odi} - \frac{Z_L}{L_i} \sin(\delta_j) i_{odj} - \frac{Z_L}{L_i} \cos(\delta_j) i_{oqj}. \tag{5.42}$$

Performing KCL at the filter node for the *d* and *q* circuits, one arrives at

$$C_{fi}\dot{v}_{odi} = C_{fi}\omega_i v_{oqi} + i_{ldi} - i_{odi} \tag{5.43}$$

$$C_{fi}\dot{v}_{oqi} = -C_{fi}\omega_i v_{odi} + i_{lqi} - i_{oqi}. \tag{5.44}$$

Note that

$$i_{ldi} = \frac{v_{idi}^{*} - v_{odi}}{R_{fi}}. \tag{5.45}$$

Throughout the analysis, we have neglected the *q* component because it is not involved in the primary controller action and it is regulated to zero as mentioned previously. The regulation to zero makes the capacitor filter state of Figure 5-8 to be modeled as a short-circuit. Hence, we can assume $\dot{v}_{oqi} = 0$. Substituting (5.21) into (5.45), we arrive at

$$i_{ldi} = \frac{V_{ni} - n_{qi}Q_i - v_{odi}}{R_{fi}}. \tag{5.46}$$

Substituting (5.46) into (5.43), we get

$$\dot{v}_{odi} = \frac{V_{ni}}{C_{fi}R_{fi}} - \frac{n_{qi}}{C_{fi}R_{fi}}Q_i - \frac{1}{C_{fi}R_{fi}}v_{odi} - \frac{1}{C_{fi}}i_{odi}. \tag{5.47}$$

The angle of each DG is defined as

$$\dot{\delta}_i = \omega_i - \omega_{com} \tag{5.48}$$

where $\omega_{com}$ is the angular frequency of the common reference frame. One of the DGs is taken as the common reference. Here, we assume $\omega_1 = \omega_{com}$. Substituting (5.20) into (5.48), we arrive at

$$\dot{\delta}_i = \omega_{ni} - m_{pi}P_i - \omega_{n1} + m_{p1}P_1. \tag{5.49}$$

Equations (5.28), (5.29), (5.41), (5.42), (5.47), and (5.49) describe the reduced-order nonlinear dynamics of each DG including the effects of the network dynamics and the coupling between the units.

## 5.4 LINEARIZATION OF THE DQ BASED REDUCED-ORDER MODEL

The system of nonlinear equations can be expressed in a compact form as

$$\begin{aligned} \dot{x}(t) &= h(x(t), u(t), t) \\ y(t) &= f(x(t), u(t), t) \end{aligned} \quad . \tag{5.50}$$

Here we demonstrate the proposed method on a two DG system, but our modeling approach can be generalized to any *n* DG systems. The states for a two DG system are defined as follows:

$$x \equiv [P_1 \; Q_1 \; i_{od1} \; i_{ioq1} \; v_{od1} \; P_2 \; Q_2 \; i_{od2} \; i_{ioq2} \; v_{od2} \; \delta_2]^T$$

Note that the state for $\delta_1$ has been omitted because it is always equal to zero according to (5.49). The input to the system can be chosen as

$$u = [V_{n1} \quad V_{n2}]^T .$$

The output can be chosen as

$$y = [v_{od1} \quad v_{od2}]^T .$$

To linearize the system (5.50), suppose that the system is operating around the following operating point:

$$x_0 = [P_{10} \; Q_{10} \; i_{od10} \; i_{oq10} \; v_{od10} \; P_{20} \; Q_{20} \; i_{od20} \; i_{oq20} \; v_{od20} \; \delta_{20}]^T$$

and

$$u_0 = [V_{n10} \quad V_{n20}]^T$$

Suppose that the input is $u$. Then, for a small perturbation of the input $\bar{u}$, such that the input becomes $u = u_0 + \bar{u}$, and the state also undergoes a small perturbation $\bar{x}$, such that it becomes $x = x_0 + \bar{x}$; in that scenario the solution to the system can be approximated around the operating point as

$$\begin{aligned} \dot{x}_0 + \dot{\bar{x}} &= h(x_0 + \bar{x}, u_0 + \bar{u}) \\ &= h(x_0, u_0) + \frac{\partial h}{\partial x}\bar{x} + \frac{\partial h}{\partial u}\bar{u} + \dots \end{aligned} \tag{5.51}$$

where $\frac{\partial h}{\partial x}$ and $\frac{\partial h}{\partial u}$ are the Jacobians, which are denoted *A* and *B*, respectively. The linear small-signal state space expressions can be defined as

$$\dot{\bar{x}} = A\bar{x} + B\bar{u} \tag{5.52}$$

$$\bar{y} = C\bar{x} + D\bar{u}$$

with $C = \frac{\partial f}{\partial x}$ and $D = \frac{\partial f}{\partial u}$. Before taking the Jacobian of the nonlinear system, we can safely assume that the angle $\bar{\delta}_j$ is small such that that following holds

$$\cos\bar{\delta}_j \cong 1 \tag{5.53}$$

$$\sin\bar{\delta}_j \cong \bar{\delta}_j. \tag{5.54}$$

After substituting (5.53) and (5.54) into (5.41) and (5.42), the system is linearized by taking the Jacobian of the nonlinear system, (5.50). Hence, the linearization of the nonlinear system can be expressed in the following state-space matrices:

$$A = \begin{bmatrix} A_{11} & A_{12} \\ A_{21} & A_{22} \end{bmatrix} \tag{5.55}$$

where

$$A_{11}=\begin{bmatrix} -\omega_c & 0 & d_1 & 0 & \frac{3}{2}\omega_c i_{od10} \\ 0 & -\omega_c & 0 & -d_1 & -\frac{3}{2}\omega_c i_{oq10} \\ -m_{p1} i_{oq10} & 0 & b_1 & a_1 & \frac{1}{L_1} \\ m_{p1} i_{od10} & 0 & m_1 & b_1 & 0 \\ 0 & n_{q1} c_1 & \frac{-1}{C_{f1}} & 0 & c_1 \end{bmatrix} \tag{5.56}$$

and

$$A_{22}=\begin{bmatrix} -\omega_c & 0 & d_2 & 0 & \frac{3}{2}\omega_c i_{od20} & 0 \\ 0 & -\omega_c & 0 & -d_2 & -\frac{3}{2}\omega_c i_{oq20} & 0 \\ -m_{p2} i_{oq20} & 0 & b_2 & a_2 & \frac{1}{L_2} & 0 \\ m_{p2} i_{od20} & 0 & m_2 & b_2 & 0 & 0 \\ 0 & n_{q2} c_2 & \frac{-1}{C_{f2}} & 0 & c_2 & 0 \\ -m_{p2} & 0 & 0 & 0 & 0 & 0 \end{bmatrix} \tag{5.57}$$

where

$$a_i = \omega_{ni} - m_{pi} P_{i0}$$

$$b_i = \frac{-R_i - Z_L}{L_i}$$

$$c_i = -\frac{1}{C_{fi} R_{fi}}$$

$$d_i = \omega_c v_{odi0}$$

$$m_i = m_{pi} P_{i0} - \omega_{ni}$$

The coupling terms of the system are expresses as:

$$A_{12}=\begin{bmatrix} 0 & 0 & 0 & 0 & 0 & 0 \\ 0 & 0 & 0 & 0 & 0 & 0 \\ 0 & 0 & \dfrac{-Z_L}{L_1} & \dfrac{Z_L}{L_1}\delta_{20} & 0 & \dfrac{Z_L}{L_1}i_{oq20} \\ 0 & 0 & \dfrac{-Z_L}{L_1}\delta_{20} & \dfrac{-Z_L}{L_1} & 0 & -\dfrac{Z_L}{L_1}i_{od20} \\ 0 & 0 & 0 & 0 & 0 & 0 \end{bmatrix} \tag{5.58}$$

and

$$A_{21}=\begin{bmatrix} 0 & 0 & 0 & 0 & 0 \\ 0 & 0 & 0 & 0 & 0 \\ 0 & 0 & \dfrac{-Z_L}{L_2} & 0 & 0 \\ 0 & 0 & 0 & \dfrac{-Z_L}{L_2} & 0 \\ 0 & 0 & 0 & 0 & 0 \\ m_{p1} & 0 & 0 & 0 & 0 \end{bmatrix}. \tag{5.59}$$

The input matrix is

$$B=\begin{bmatrix} 0 & 0 & 0 & 0 & -c_1 & 0 & 0 & 0 & 0 & 0 & 0 \\ 0 & 0 & 0 & 0 & 0 & 0 & 0 & 0 & 0 & -c_2 & 0 \end{bmatrix}^T \tag{5.60}$$

and the output matrices are

$$C=\begin{bmatrix} 0 & 0 & 0 & 0 & 1 & 0 & 0 & 0 & 0 & 0 & 0 \\ 0 & 0 & 0 & 0 & 0 & 0 & 0 & 0 & 0 & 1 & 0 \end{bmatrix} \tag{5.61}$$

and $D=0$.

Matrices (5.55), (5.60), and (5.61) describe the reduced-order linearized model of the two DG system with the coupling, (5.58) and (5.59), clearly observed in the off-diagonal terms of (37). As mentioned previously, the model developed and simulated in this chapter is for a two-DG system for demonstration purposes. The modeling approach can be extended to include any *n* arbitrary DG system as follows:

$$A = \begin{bmatrix} A_{11} & A_{12} & \cdots & A_{1n} \\ A_{21} & A_{22} & \cdots & A_{2n} \\ \vdots & \vdots & \ddots & \vdots \\ A_{n1} & A_{n2} & \cdots & A_{nn} \end{bmatrix} \tag{5.62}$$

where the diagonal terms are the same as $A_{22}$ but with the associated index. The off-diagonal terms (assuming the frequency at DG 1 is the common frequency) are

$$A_{1n} = \begin{bmatrix} 0 & 0 & 0 & 0 & 0 & 0 \\ 0 & 0 & 0 & 0 & 0 & 0 \\ 0 & 0 & \dfrac{-Z_L}{L_1} & \dfrac{Z_L}{L_1}\delta_{n0} & 0 & \dfrac{Z_L}{L_1} i_{oqn0} \\ 0 & 0 & \dfrac{-Z_L}{L_1}\delta_{n0} & \dfrac{-Z_L}{L_1} & 0 & -\dfrac{Z_L}{L_1} i_{iodn0} \\ 0 & 0 & 0 & 0 & 0 & 0 \end{bmatrix} \tag{5.63}$$

and

$$A_{n1} = \begin{bmatrix} 0 & 0 & 0 & 0 & 0 \\ 0 & 0 & 0 & 0 & 0 \\ 0 & 0 & \dfrac{-Z_L}{L_n} & 0 & 0 \\ 0 & 0 & 0 & \dfrac{-Z_L}{L_n} & 0 \\ 0 & 0 & 0 & 0 & 0 \\ m_{p1} & 0 & 0 & 0 & 0 \end{bmatrix} \tag{5.64}$$

and

$$A_{nk} = \begin{bmatrix} 0 & 0 & 0 & 0 & 0 & 0 \\ 0 & 0 & 0 & 0 & 0 & 0 \\ 0 & 0 & \dfrac{-Z_L}{L_n} & \dfrac{Z_L}{L_n}\delta_{k0} & 0 & \dfrac{Z_L}{L_n} I_{oqk0} \\ 0 & 0 & \dfrac{-Z_L}{L_n}\delta_{k0} & \dfrac{-Z_L}{L_n} & 0 & -\dfrac{Z_L}{L_n} I_{odk0} \\ 0 & 0 & 0 & 0 & 0 & 0 \\ m_{pk} & 0 & 0 & 0 & 0 & 0 \end{bmatrix} \tag{5.65}$$

where $n \neq k$, $n \neq 1$, and $k \neq 1$

For convenience the whole A matrix for a 2 DG microgrid system which is used for simulation in the next section is $A =$

$$\begin{bmatrix}
-\omega_c & 0 & d_1 & 0 & \frac{3}{2}\omega_c I_{od10} & 0 & 0 & 0 & 0 & 0 & 0 \\
0 & -\omega_c & 0 & -d_1 & -\frac{3}{2}\omega_c I_{oq10} & 0 & 0 & 0 & 0 & 0 & 0 \\
-m_{p1} I_{oq10} & 0 & b_1 & a_1 & \frac{1}{L_1} & 0 & 0 & \frac{-Z_L}{L_1} & \frac{Z_L}{L_1}\delta_{20} & 0 & \frac{Z_L}{L_1} I_{oq20} \\
m_{p1} I_{od10} & 0 & m_1 & b_1 & 0 & 0 & 0 & \frac{-Z_L}{L_1}\delta_{20} & \frac{-Z_L}{L_1} & 0 & -\frac{Z_L}{L_1} I_{od20} \\
0 & n_{q1} c_1 & -\frac{1}{C_{f1}} & 0 & c_1 & 0 & 0 & 0 & 0 & 0 & 0 \\
0 & 0 & 0 & 0 & 0 & -\omega_c & 0 & d_2 & 0 & \frac{3}{2}\omega_c I_{od20} & 0 \\
0 & 0 & 0 & 0 & 0 & 0 & -\omega_c & 0 & -d_2 & -\frac{3}{2}\omega_c I_{oq20} & 0 \\
0 & 0 & \frac{-Z_L}{L_2} & 0 & 0 & -m_{p2} I_{oq20} & 0 & b_2 & a_2 & \frac{1}{L_2} & 0 \\
0 & 0 & 0 & \frac{-Z_L}{L_2} & 0 & m_{p2} I_{od20} & 0 & m_2 & b_2 & 0 & 0 \\
0 & 0 & 0 & 0 & 0 & 0 & n_{q2} c_2 & -\frac{1}{C_{f2}} & 0 & c_2 & 0 \\
m_{p1} & 0 & 0 & 0 & 0 & -m_{p2} & 0 & 0 & 0 & 0 & 0
\end{bmatrix} \tag{5.66}$$

## 5.5 MODEL VALIDATION RESULTS

Here a comparison between the reduced-order, linear model and the high-order, nonlinear model is presented. The models are simulated in MATLAB. The system parameters are shown in Table 5-1 and the initial conditions are shown in Table 5-2. The results are shown for DG 2 only, as DG 1 showed the same results.

**Table 5-1. System Parameters**

| Inverter parameters (10 kA rating) | | | |
|---|---|---|---|
| Parameter | Value | Parameter | Value |
| $V_{DC}$ | 650 V | $R_{f1}$ and $R_{f2}$ | 0.1 Ω |
| $V_n$ | 381.0512 V | $L_{f1}$ and $L_{f2}$ | 1.35 mH |
| $m_{p1}$ and $m_{p2}$ | 0.000094 | $C_{f1}$ and $C_{f2}$ | 50 µF |
| $n_{Q1}$ and $n_{Q2}$ | 0.0013 | $R_{c1}$ and $R_{c2}$ | 0.03 Ω |
| $R_{12}$ | 0.23 Ω | $L_{12}$ | 318.31 µH |

**Table 5-2. Initial Conditions**

| Parameter | Value | Parameter | Value |
|---|---|---|---|
| $P_1$ | 2895.57 W | $P_2$ | 2895.57 W |
| $Q_1$ | 516.269 Var | $Q_2$ | − 497.269 Var |
| $i_{od1}$ | 7.68673 A | $i_{od2}$ | 7.70183 A |
| $i_{oq1}$ | − 1.3576 A | $i_{oq2}$ | 1.3025 A |
| $v_{od1}$ | 380.3611 V | $v_{od2}$ | 381.7175 V |
| $Z_L$ | 25 Ω | $\delta_2$ | 0.0029857 rad |

A step response of the load is performed here to show the comparison between the full order and reduced order models. We can see from Figure 5-9 - Figure 5-12, and Figure 5-14 that the reduced-order model simulation results match very closely with the non-linear, high-order simulation for $P_2$, $Q_2$, $I_{od2}$, $I_{oq2}$, and $\delta_2$, respectively.

Figure 5-13 shows the voltage $v_{od2}$ which also matches closely with the nonlinear high-order model except for the very high-frequency transients. These transients are much lower in magnitude in the reduced-order model because the fast acting states are not accounted for in the reduced-order model. There is a system oscillation in the voltage waveform matching the high-order, non-linear model in its shape as shown in the magnified portion of Figure 5-13. This oscillation is not present in the capacitor voltage of the reduced-order model developed in [53] even though the model in [53] has more states than the model developed here. Compared to [53], our reduced order model accounts for high frequency system transients.

A comparison between a model without the coupling terms and the model with the coupling terms is shown in Figure 5-15. It can be clearly observed that there are multiple critical modes close to the real axis that are not clearly predicted in the uncoupled model. It is very clear from Figure 5-15 that the coupling terms (off-diagonal elements) greatly influence the dominant modes. Hence, neglecting them will influence the stability of the system.

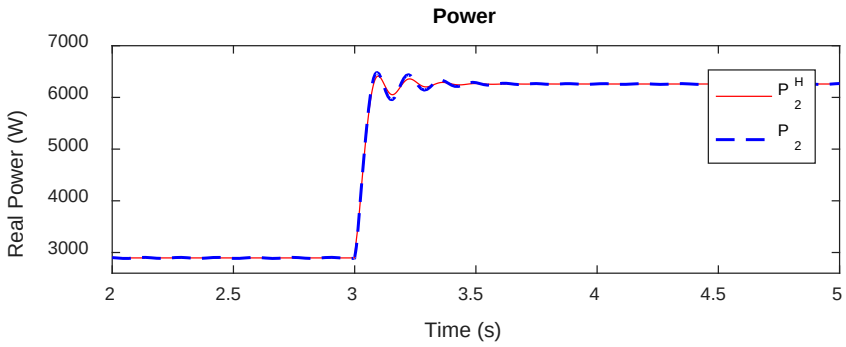


**Figure 5-9.** Plot of the real power of the high-order, nonlinear model at DG 2 ($P_2^H$) compared with that of the reduced-order model ($P_2$).

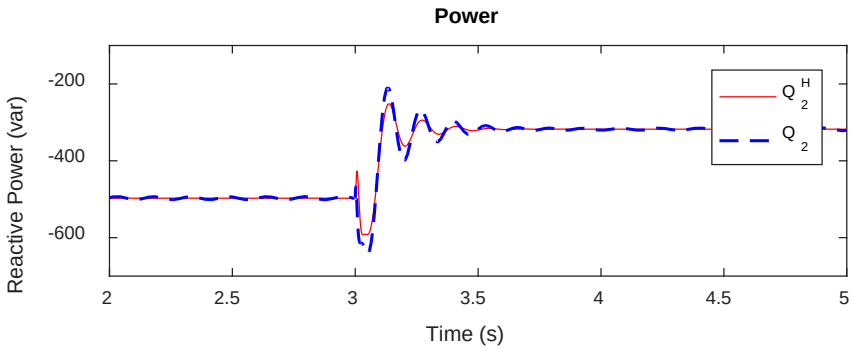


**Figure 5-10.** Plot of the reactive power of the high-order, nonlinear model at DG 2 ($Q_2^H$) compared with that of the reduced-order model ($Q_2$).

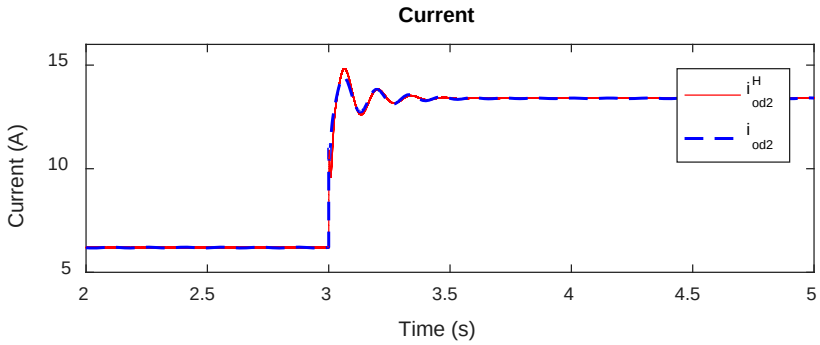


**Figure 5-11.** Plot of the d-axis's current of the high-order, nonlinear model at DG 2 ($I_{od2}^H$) compared with that of the reduced-order model ($I_{od2}$).

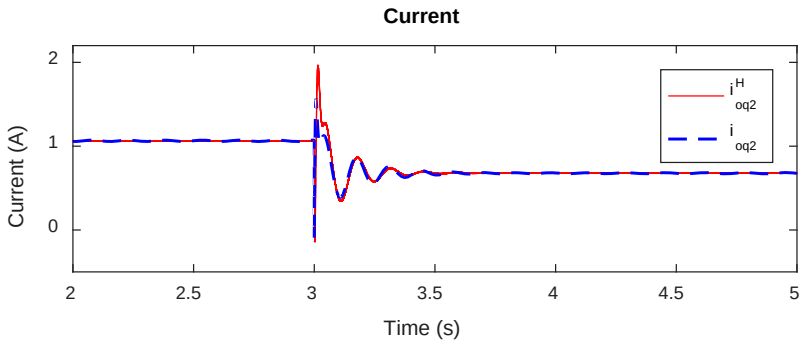


**Figure 5-12.** Plot of the q-axis's current of the high-order, nonlinear model at DG 2 ($I_{oq}^{2H}$) compared with that of the reduced-order model ($I_{oq2}$).

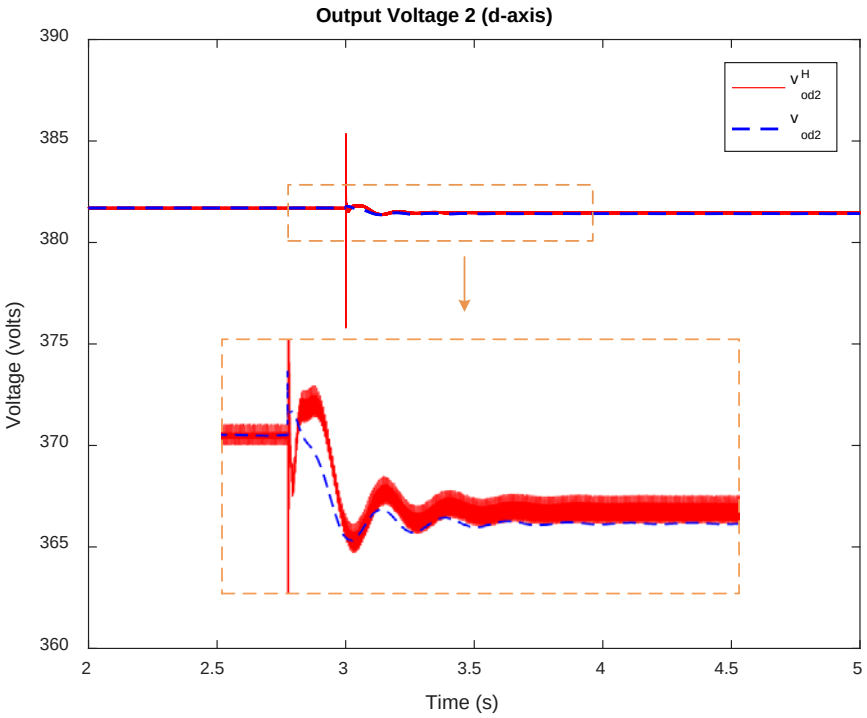


**Figure 5-13.** Plot of d-axis's voltage of the high-order nonlinear model at DG 2 ($v_{oq2}^{H}$) compared with that of the reduced-order model ($v_{od2}$).

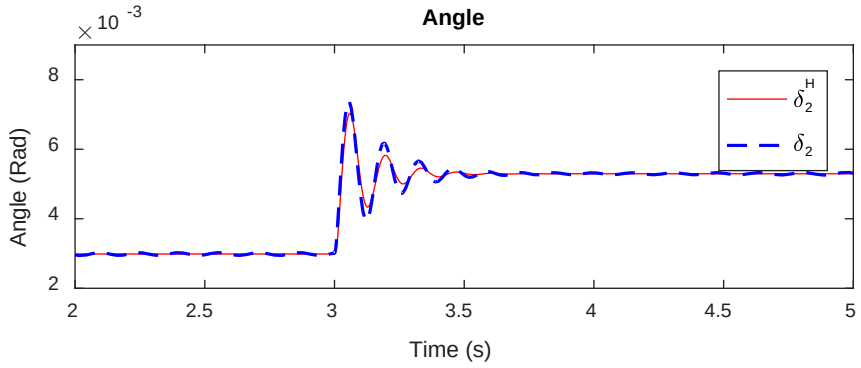


**Figure 5-14.** Plot of the angle of the high-order nonlinear model at DG 2 ($\delta_2^{H}$) compared with that of the reduced-order model ($\delta_2$).

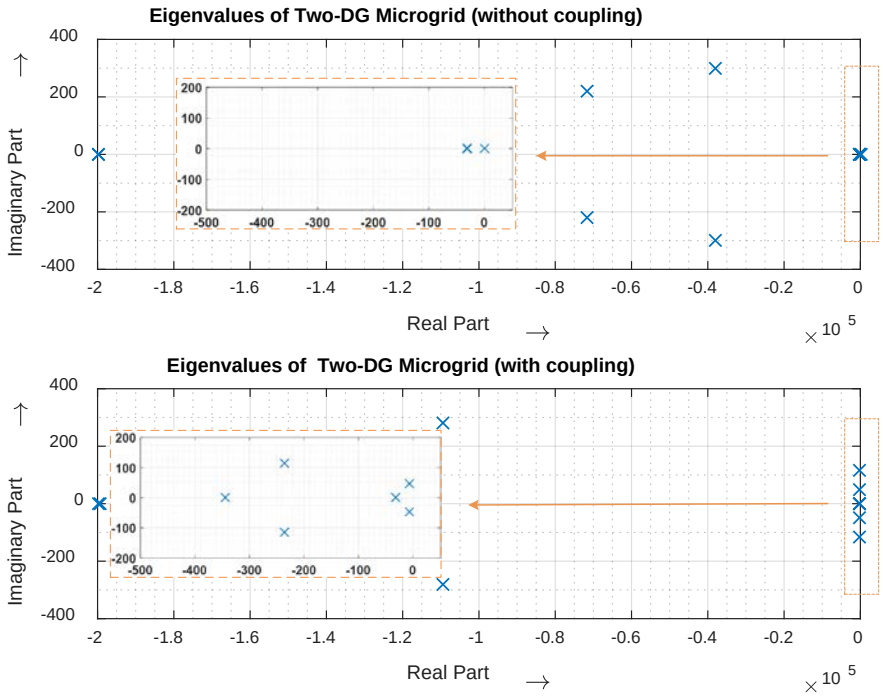


**Figure 5-15.** Poles and zeros of the reduced-order model without the coupling terms compared with the model with coupling terms.

## 5.6 CONCLUSION

In this chapter, the lowest possible reduced-order model for secondary level controller design/tuning and primary level control tuning purposes was derived. The model was derived based on our physical insights of the system as opposed to using other mathematical methods. This approach made it possible to derive a simple, useful, and low-order model that captures significant modes while keeping important effects of those modes such as network dynamics and coupling between DGs. This was not possible in other reduced order models available in the literature because they relied only on utilizing some mathematical techniques without utilizing

the complete understanding of the system. Eigenvalue analysis showed that coupling greatly influences the dominant modes of the microgrid. The order of the model derived is 2*n* lower than that of the reduced ones available in the literature of similar accuracy. Although the developed model order is almost one third of the order of the full-order models, simulation results showed strong agreement between the reduced-order model with the high-order, nonlinear model.

# 6.0 ROBUST CONTROLLER DESIGN UTILIZING THE REDUCED-ORDER MODEL

The reduced order model will be utilized to synthesize a controller robust against large load changes. This is for the purpose of demonstrating the usefulness of the model developed. The controller is designed using linear quadratic integral (LQI) control method. The controller is designed based on the low-order model and a comparison is made between the performance of the controller on the low-order linearized model and the high-order non-linear model. This comparison showed that the controllers' behavior is the same regardless of the model utilized which demonstrates the effectiveness of the reduced-order model.

## 6.1 INTRODUCTION

Microgrids have the ability to operate in grid connected and islanded modes allowing it to be operational in the case of planned or unplanned outages on the main utility grid. However, when the islanded mode becomes operational, this produces unbalances in the supply and demand of the active and reactive power of the microgrid [123]. Primary control, which is the first layer of the hierarchal control structure, is used to balance the mismatch of power between distributed generation (DG) units. Droop control is often used for this layer, which causes deviations in the

voltage and frequency. Hence, a second layer called secondary control is used to compensate for the voltage and frequency deviations [36].

The focus of this chapter is secondary voltage control. Secondary control can be performed in a centralized, de-centralized, or distributed fashion [36], [43], [45], [124]. Decentralized control has plug and play capabilities and is independent of communication links [125]. However, decentralized is harder to control and has operational limitations, and also has drawbacks in voltage and frequency regulation with load changes; hence, affect voltage and frequency of sensitive loads [105], [126]. Centralized control, however, can achieve the restoration of voltage during such load changes. Centralized control uses communication links to pass information in order to generate the appropriate voltage and frequency [125]. The data is fed through low bandwidth communication links in order to achieve voltage and frequency restoration during islanding operations [45]. Generally speaking, centralized control is appropriate for islanded conditions while de-centralized and distributed approaches are suitable for grid-connected conditions [32]. The focus of this chapter is islanded conditions under extreme load changes. Hence, the centralized approach will be adopted.

The main contribution of this chapter is the utilization of LQI control to regulate the voltage following sharp load changes. This is for the purpose of showing the effectiveness of the reduced-order model for secondary controller design.

## 6.2 EXTREME LOAD CHANGES WITHOUT SECONDARY CONTROL

Here the microgrid is modified to be rated at 66 kVA and a load of 65 kVA with 0.87 power factor is applied at 3 seconds to show the behavior of the system under large load change. The simulation results is shown for both the reduced order linear model and the full-order non-linear model. All the states of the system are shown in Figure 6-1 to Figure 6-11. We can see that the voltage at DG 1 drops to 355.8 V which is around 7% drop from the nominal of 381.05 V and the voltage at DG2 drops to 369.82 V, which is around 3% drop from the nominal. The voltage drop is different at both terminals due to the unequal line impedances. The LQI control which will be designed in the next sub-sections will regulate these voltage back to the nominal.

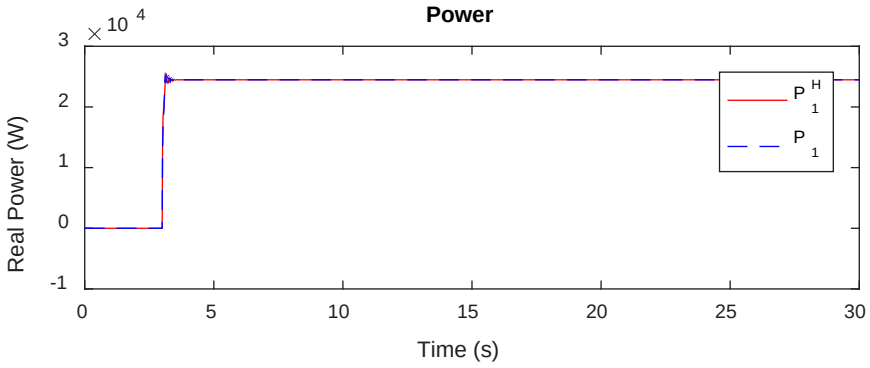


**Figure 6-1.** Plot of the real power of the high-order, nonlinear model at DG 1 ($P_1^H$) compared with that of the reduced-order model ($P_1$).

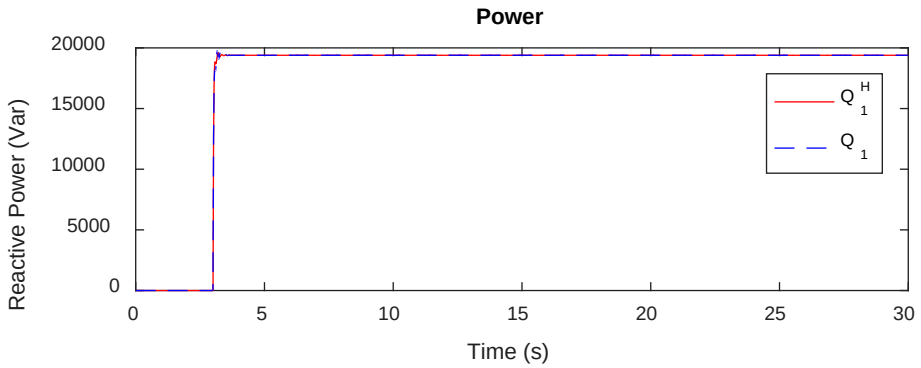


**Figure 6-2.** Plot of the reactive power of the high-order, nonlinear model at DG 1 ($Q_1^H$) compared with that of the reduced-order model ($Q_1$).

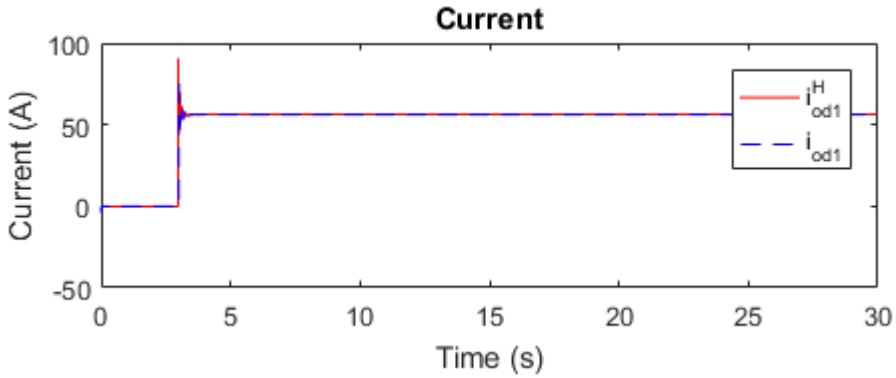


**Figure 6-3.** Plot of the d-axis's current of the high-order, nonlinear model at DG 1 ($I_{od1}^H$) compared with that of the reduced-order model ($I_{od1}$).

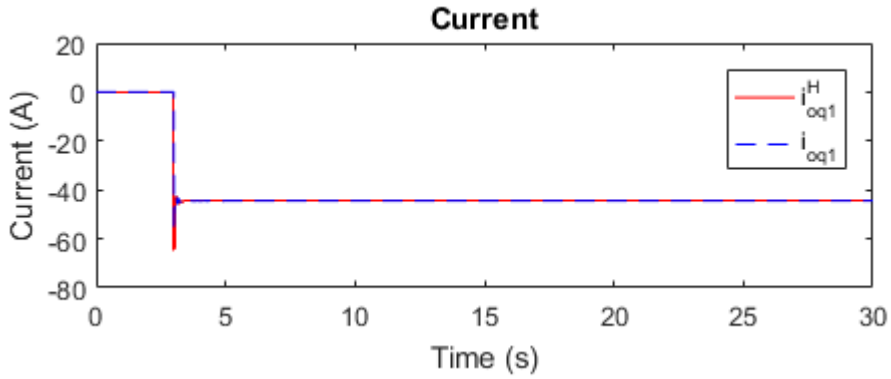


**Figure 6-4.** Plot of the q-axis's current of the high-order, nonlinear model at DG 1 ($I_{oq1}^H$) compared with that of the reduced-order model ($I_{oq1}$).

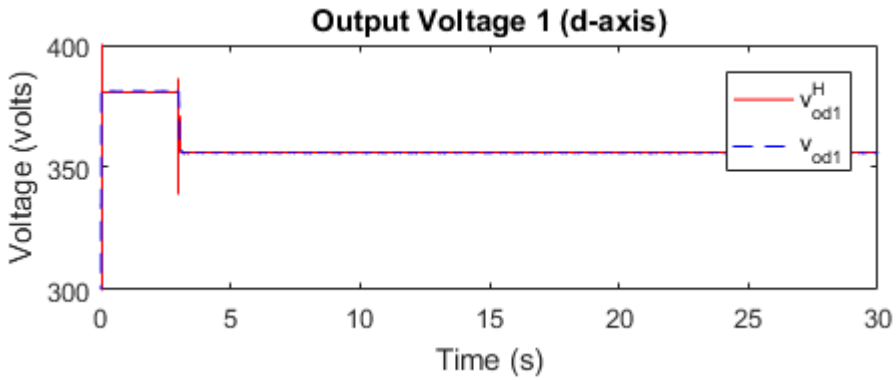


**Figure 6-5.** Plot of d-axis's voltage of the high-order nonlinear model at DG 1 ($v_{oq1}{}^{H}$) compared with that of the reduced-order model ($v_{od1}$).

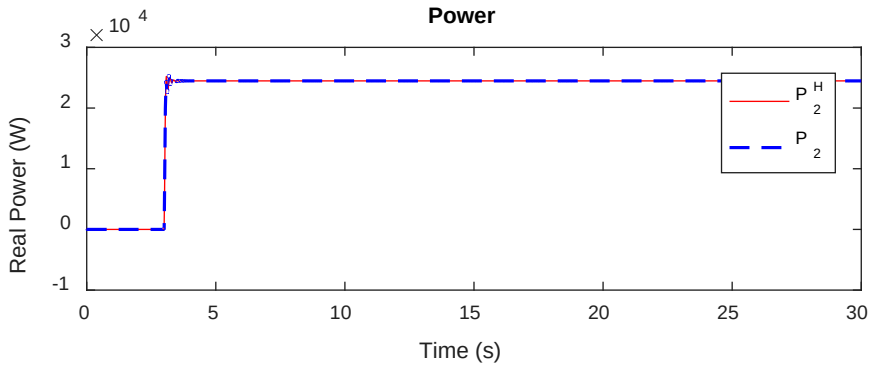


**Figure 6-6.** Plot of the real power of the high-order, nonlinear model at DG 2 ($P_2{}^{H}$) compared with that of the reduced-order model ($P_2$).

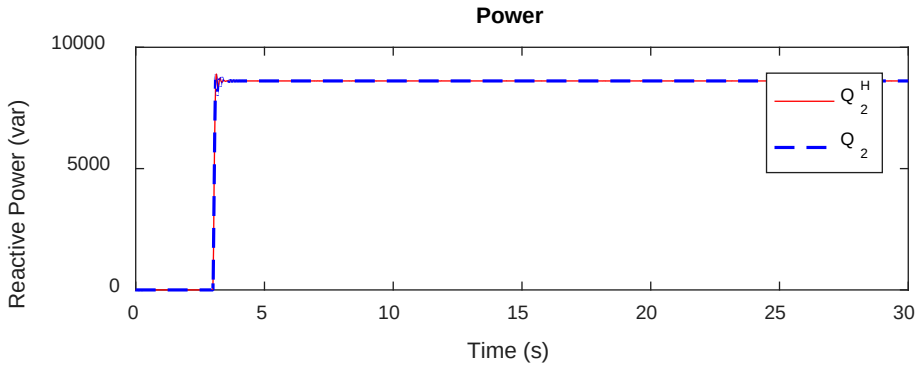


**Figure 6-7.** Plot of the reactive power of the high-order, nonlinear model at DG 2 ($Q_2{}^{H}$) compared with that of the reduced-order model ($Q_2$).

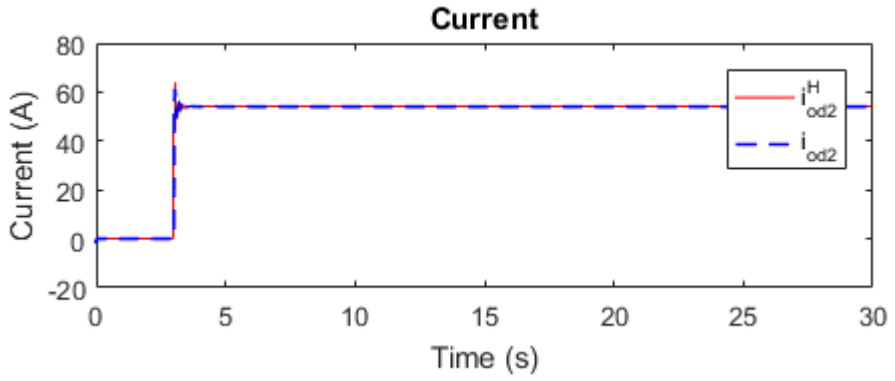


**Figure 6-8.** Plot of the d-axis's current of the high-order, nonlinear model at DG 2 ($I_{od2}{}^{H}$) compared with that of the reduced-order model ($I_{od2}$).

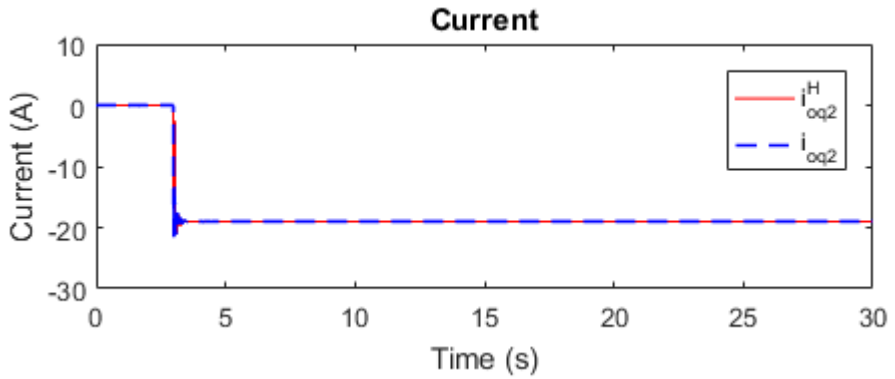


**Figure 6-9.** Plot of the q-axis's current of the high-order, nonlinear model at DG 2 ($I_{oq2}{}^{H}$) compared with that of the reduced-order model ($I_{oq2}$).

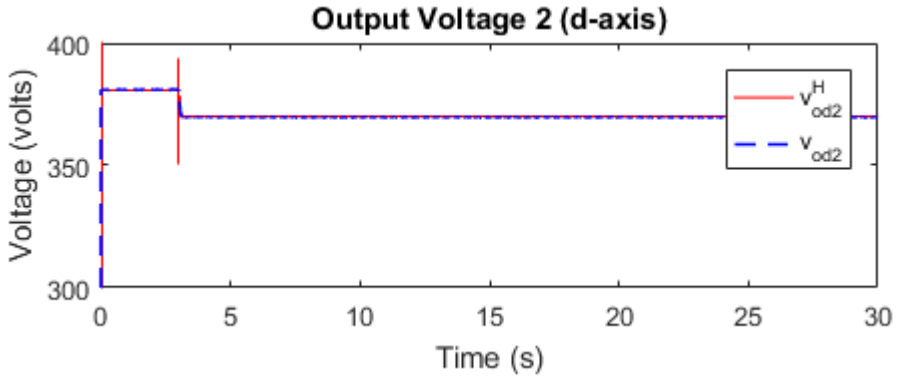


**Figure 6-10.** Plot of d-axis's voltage of the high-order nonlinear model at DG 2 ($v_{od2}{}^{H}$) compared with that of the reduced-order model ($v_{od2}$).

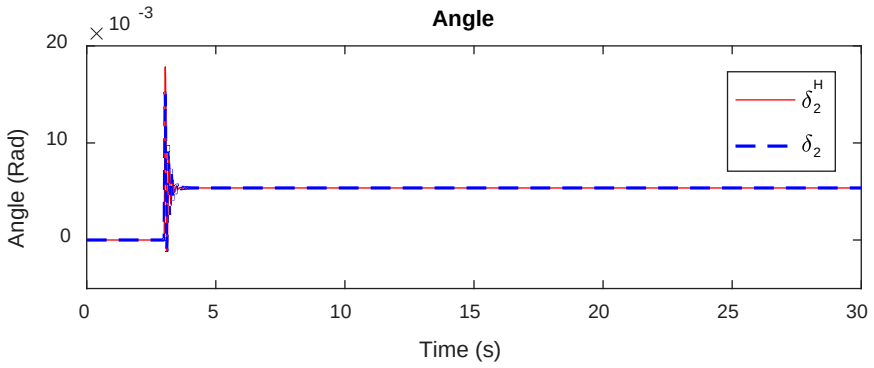


**Figure 6-11.** Plot of the angle of the high-order nonlinear model at DG 2 ($\delta_2{}^H$) compared with that of the reduced-order model ($\delta_2$).

## 6.3 SECONDARY LQI VOLTAGE CONTROL

Our goal here is to regulate the voltage at the terminal of the inverter, which is the voltage across the capacitor $C_{fi}$ (i.e. the voltages $v_{oi}$ and $v_{oj}$). The system makes the *d*-axis voltage lag the phase *A* voltage by 90$^o$ such that the *q* component of the voltage is driven to zero [35]. Hence, regulating the terminal voltage is nothing but regulating the d-axis voltage (i.e $v_{odi}$ and $v_{odj}$). Figure 6-12 shows how the secondary LQI controller is applied to the 2DG micorgrid system.

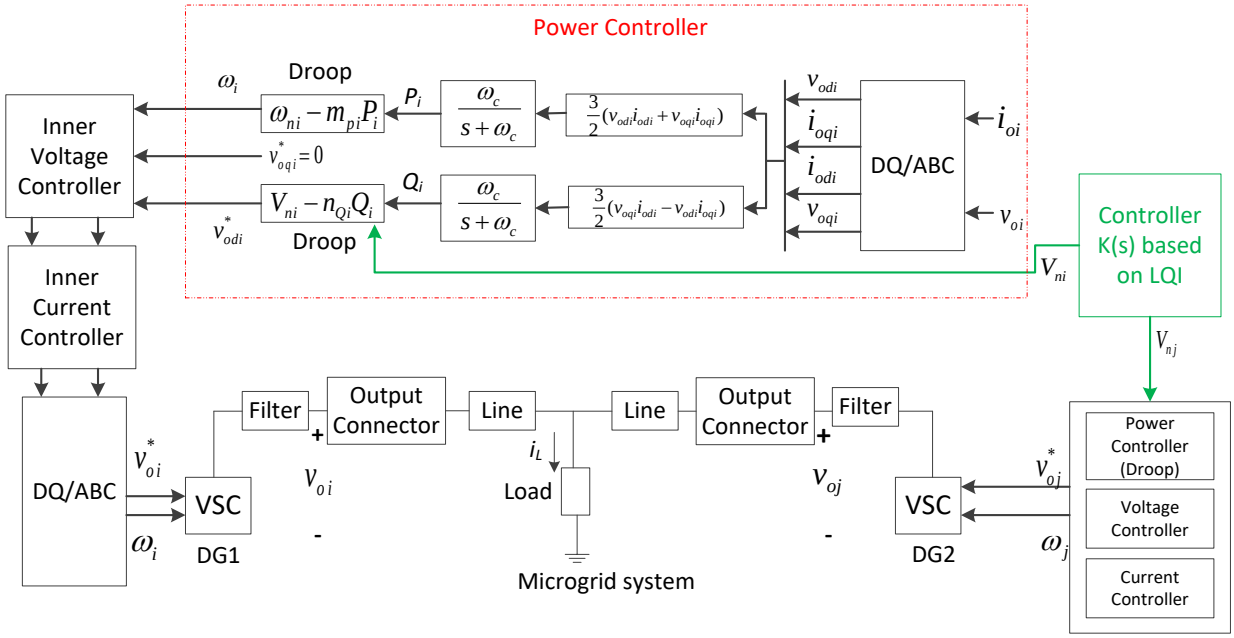


**Figure 6-12.** Microgrid system with the proposed LQI secondary controller

The objective of the secondary controller is to regulate the voltage at the terminal to its nominal value within a tight tolerance. The voltage deviations cannot exceed 5% according to ANSI C84.1 standard [127]. The most common approach to do this is to shift the droop curve as in Figure 6-13 to achieve the desired voltage. Here, the system is assumed to have high X/R ratio. This makes the reactive power proportional to voltage and the real power proportional to the frequency. If the system does not have high X/R ratio, then coupling between both droop equations can occur. The controller design approach that will be presented in the next section can be easily modified to account for any X/R ratio.

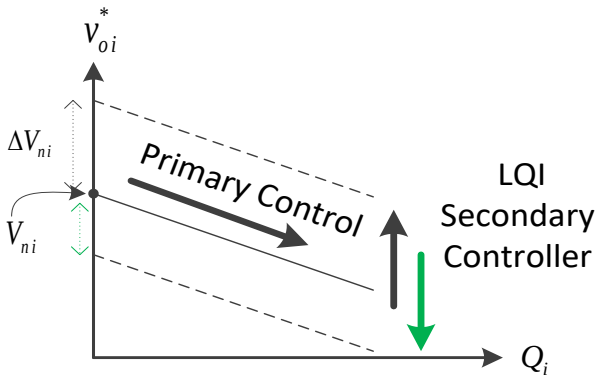


**Figure 6-13.** Primary control curve with secondary control

### 6.3.1 Linear Quadratic Integral Control Approach

The LQI controller will be designed to alleviate voltage deviations due to extreme load changes in islanded conditions. The controller is designed with the architecture shown in Figure 6-14 [128]. The microgrid plant can be modeled in state-space format by

$$\begin{aligned} \dot{x} &= Ax + Bu \\ y &= Cx \end{aligned} \tag{6.1}$$

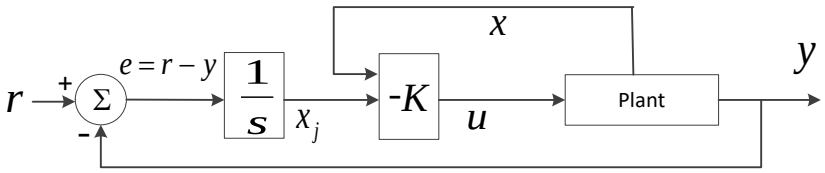


**Figure 6-14. Proposed linear quadratic integral controller**

where $A$ is the open loop system matrix derived as in equation (5.66), and $x$ is vector of all the states of the system. The input is defined as in the previous chapter, which is expressed again here for convenience as

$$u = [V_{n1} \quad V_{n2}]^T \tag{6.2}$$

where $V_{n1}$ and $V_{n2}$ are the set-points for the droop controller 1 and 2, respectively. Hence, the B matrix can be chosen accordingly as in equation (5.60). It is desired to control the terminal d-axis voltage. Hence, the output is defined as in the previous chapter, which is expressed again here for convenience as

$$y = [v_{od1} \quad v_{od2}]^T . \tag{6.3}$$

Hence, the *C* matrix is chosen as in (61). The controller K designed will add two extra states ($x_j$ is a vector of size 2). The addition of the two extra states corresponds to the two states to be controlled (one for each DG). Hence, the number of integrators have to equal the number of controlled outputs. The two states are the voltage error (difference between nominal and actual values) as

$$e_1 = r - y_1 = r - v_{od1} \tag{6.4}$$

and

$$e_2 = r - y_2 = r - v_{od2} . \tag{6.5}$$

The control law becomes

$$u = -Kz \tag{6.6}$$

where *z* contains the states of the system after adding the two extra states i.e.

$$z = \begin{bmatrix} x \\ x_{new} \end{bmatrix}, \tag{6.7}$$

where

$$x_{new} = \begin{bmatrix} e_1 \\ e_2 \end{bmatrix}.$$

Therefore, the overall model (with the augmented integrator) becomes:

$$\dot{z} = A_{aug} z + B_{aug} u$$
$$y = C_{aug} z \tag{6.8}$$

where $A_{aug}$ contains the original A with the addition of two new rows that account for additional integral states. The matrixes $B_{aug}$ and $C_{aug}$ are also constructed in a similar manner. The control law is derived using LQI method, which minimizes the cost function [128]

$$J(u) = \int_0^\infty \left( z^T Q z + u^T R u + 2 z^T N u \right) dt \tag{6.9}$$

with the following assumptions held true:

1) the augments system $(A_{aug}, B_{aug})$ is stabilizable.

2) $R > 0$ and $Q - NR^{-1}N^T \geq 0$

3) $(Q - NR^{-1}N^T, A_{aug} - B_{aug}R^{-1}N^T)$ detectable

The weighting functions *Q*, *R*, and *N* are defined in Appendix A.

## 6.4 EXTREME LOAD CHANGES WITH SECONDARY LQI CONTROL

The LQI controller designed in the previous sub-section is applied to the microgrid reduced-order linearized model and the full-order nonlinear model. Simulation results under the extreme load change (refer to section 6.2) is shown here with proposed controller applied to the system. The simulation results here show that the behavior of controller applied to the reduced order model matches with the behavior when the controller is applied to the full-order nonlinear model. Figure 6-15 to Figure 6-25 show the behavior of the controller on all states of the system for both models. Figure 6-19 and Figure 6-24 show that the proposed LQI controller designed

based on the reduced-order model is able to regulate voltages of DG1 and DG2 back to their nominal values, respectively. This shows the effectiveness of the reduced-order model for controller design purposes.

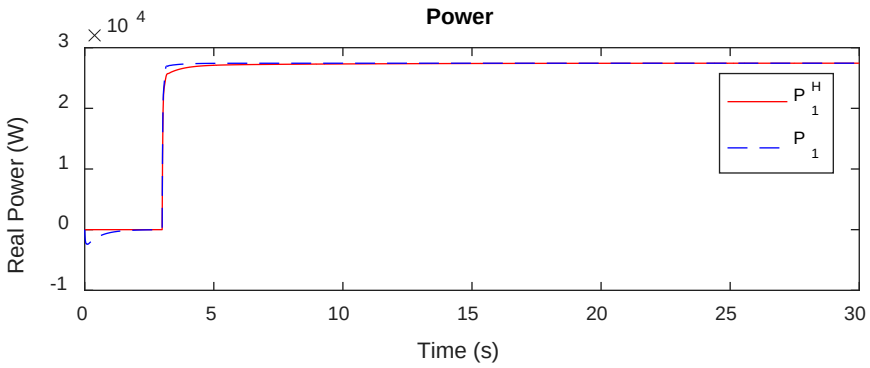


**Figure 6-15.** Plot of the real power of the high-order, nonlinear model at DG 1 ($P_1^H$) compared with that of the reduced-order model ($P_1$) with LQI control applied to both.

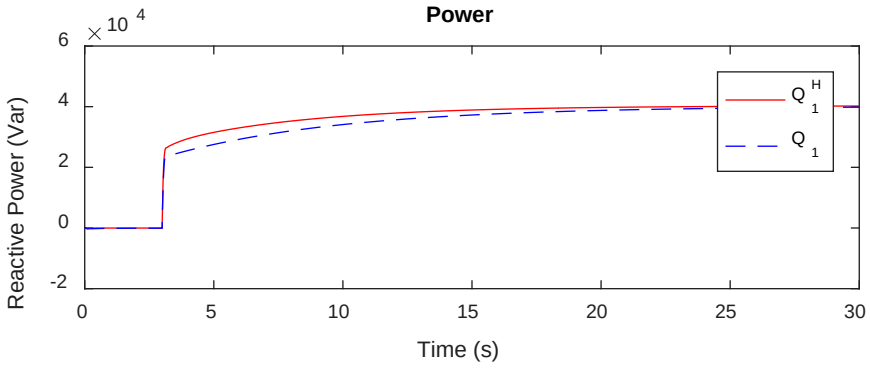


**Figure 6-16.** Plot of the reactive power of the high-order, nonlinear model at DG 1 ($Q_1^H$) compared with that of the reduced-order model ($Q_1$) with LQI control applied to both.

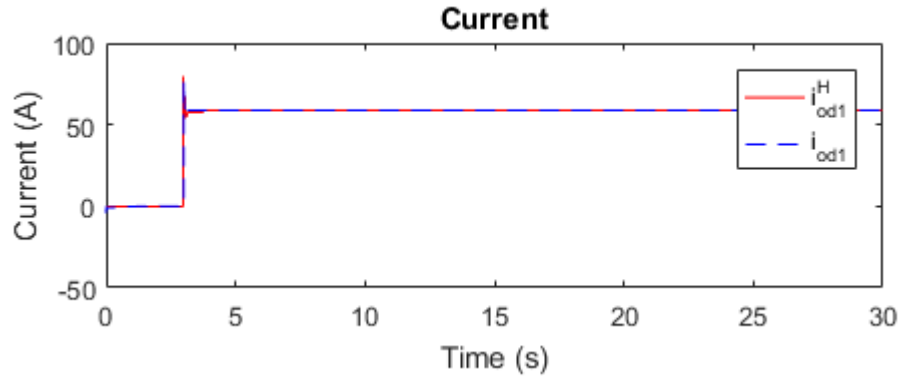


**Figure 6-17.** Plot of the d-axis's current of the high-order, nonlinear model at DG 1 ($I_{od1}^{H}$) compared with that of the reduced-order model ($I_{od1}$) with LQI control applied to both.

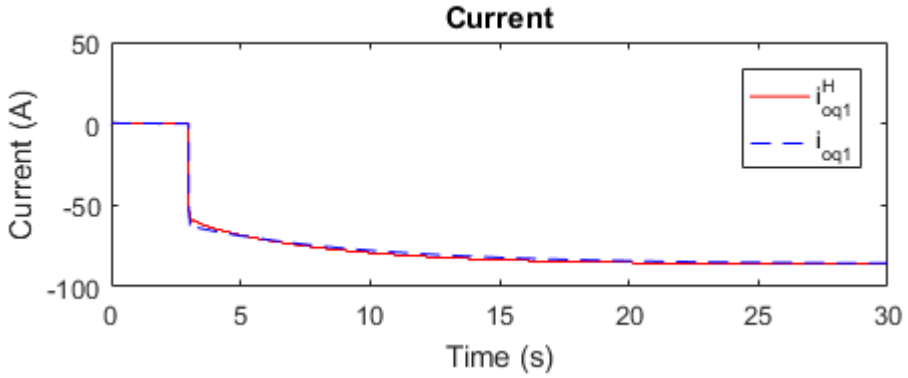


**Figure 6-18.** Plot of the q-axis's current of the high-order, nonlinear model at DG 1 ($I_{oq1}^{H}$) compared with that of the reduced-order model ($I_{oq1}$) with LQI control applied to both.

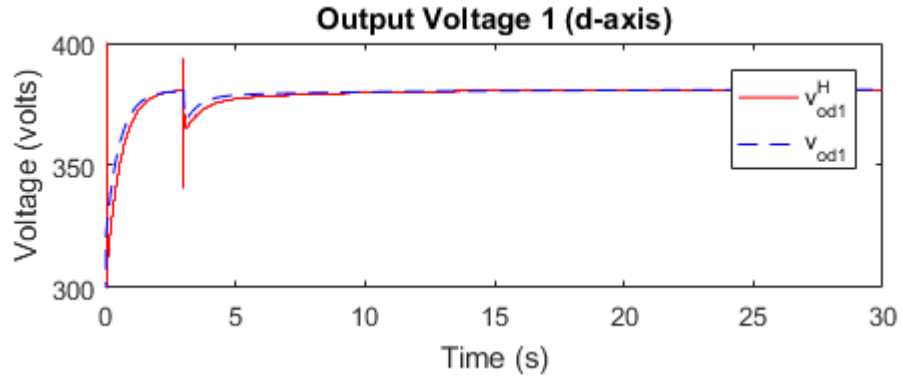


**Figure 6-19.** Plot of d-axis's voltage of the high-order nonlinear model at DG 1 ($v_{od1}^{H}$) compared with that of the reduced-order model ($v_{od1}$) with LQI control applied to both.

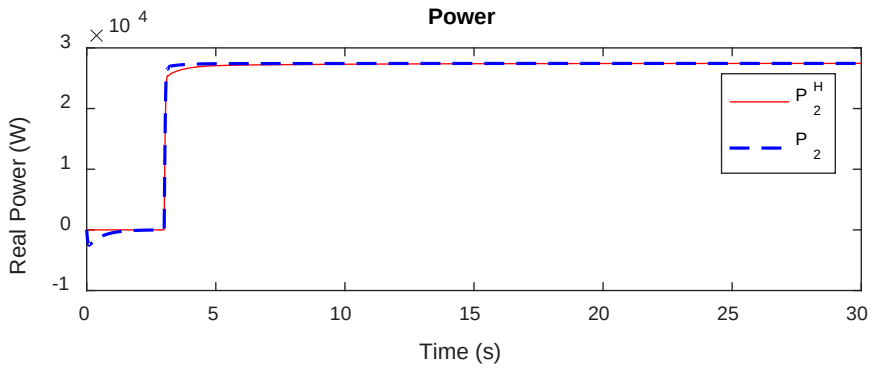


**Figure 6-20.** Plot of the real power of the high-order, nonlinear model at DG 2 ($P_2^H$) compared with that of the reduced-order model ($P_2$) with LQI control applied to both.

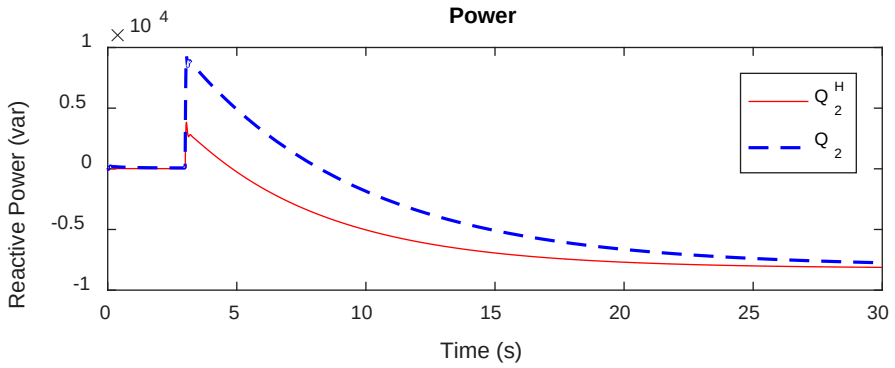


**Figure 6-21.** Plot of the reactive power of the high-order, nonlinear model at DG 2 ($Q_2^H$) compared with that of the reduced-order model ($Q_2$) with LQI control applied to both.

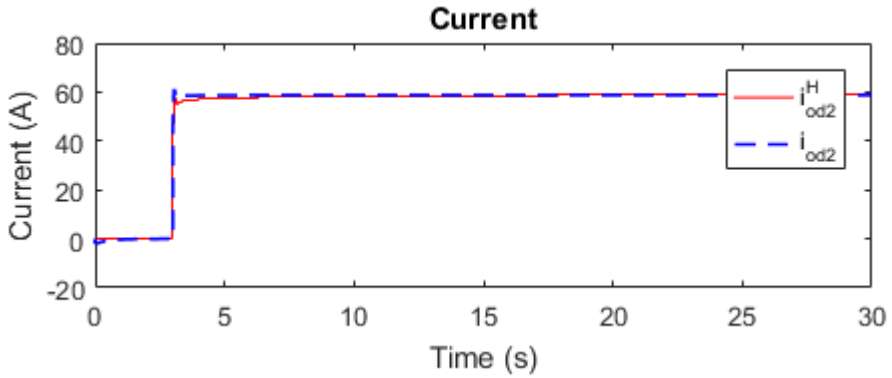


**Figure 6-22.** Plot of the d-axis's current of the high-order, nonlinear model at DG 2 ($I_{od2}^H$) compared with that of the reduced-order model ($I_{od2}$) with LQI control applied to both.

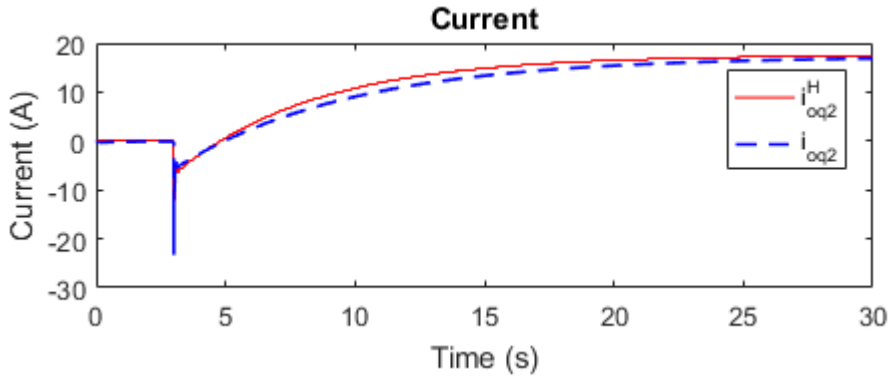


**Figure 6-23.** Plot of the q-axis's current of the high-order, nonlinear model at DG 2 ($I_{oq2}{}^{H}$) compared with that of the reduced-order model ($I_{oq2}$) with LQI control applied to both.

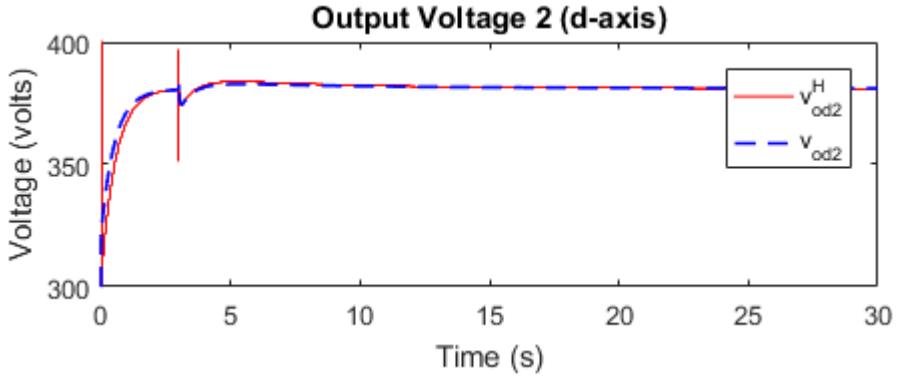


**Figure 6-24.** Plot of d-axis's voltage of the high-order nonlinear model at DG 2 ($v_{od2}{}^{H}$) compared with that of the reduced-order model ($v_{od2}$) with LQI control applied to both.

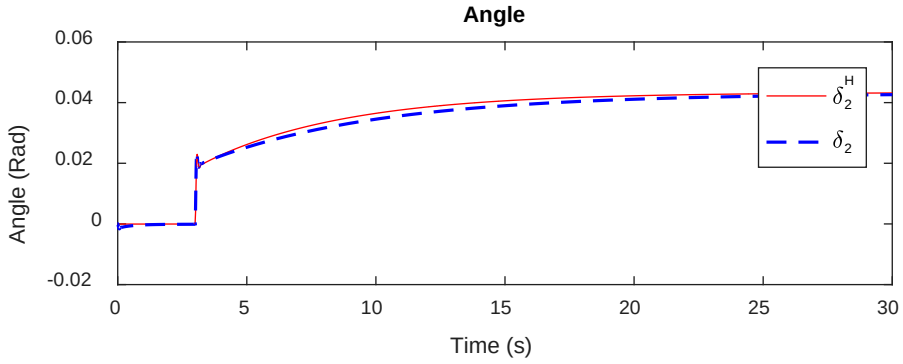


**Figure 6-25.** Plot of the angle of the high-order nonlinear model at DG 2 ($\delta_2{}^{H}$) compared with that of the reduced-order model ($\delta_2$) with LQI control applied to both.

## 6.5 CONCLUSION

This chapter demonstrated the effectiveness of utilizing the reduced-order linear model for secondary voltage control. The secondary LQI controller designed using the reduced-order model showed the same behavior when applied to the full-order model in MATLAB/SIMULINK simulation environment.

# 7.0 CONCLUSION AND FUTURE WORK

Global warming and the increased demand in electricity is pushing researchers and engineers to explore energy options alternative to fossil fuel. These issues have led to a move towards higher penetrations of renewable energy resources. When large amounts of renewable energy resources are integrated, the traditional electrical grid will face difficulties. Hence, researchers and engineers have proposed a different grid architecture called the “microgrid”. The microgrid concept was proposed not only as a way to facilitate renewable energy integration but also to increase grid reliability and security.

However, microgrids have their own protection challenges that need to be resolved in order to fully utilize their projected benefits. One of these challenges, is that traditional protection methods, such as overcurrent protection, cannot be used mainly because of low fault currents, bi-directionality of power flow, and IEEE1547 requirements. Therefore, fault current and voltage magnitudes cannot be used alone as protective indicators because they may cause breaker mis-operation or slow tripping times. Therefore, alternative fault indicators could be potential practical solutions to microgrids, which will help make our society more sustainable.

Hence, two novel methods are developed here to protect different microgrid configurations. The first method is a high-speed phase-based fault detection method. The speed of detection for this method was increased by exploiting all the phases of the three-phase power

system. The increased speed of the method can potentially be faster than high-speed directional relays. Detection using the proposed method could be done in about one third of a cycle. The effectiveness of the proposed solution was demonstrated in a PSCAD simulation environment.

The second fault detection approach is a model-based detection method. Analytical models for different fault conditions were derived to be used for this method. It is desired that the detection is not dependent upon communication channels. Hence, analytical derivations of the conditions that make the model-based detection approach work without communication channels are derived. This analytical derivation is an approach to quantify the blinding and nuisance tripping scenarios that commonly occur in renewable energy based systems.

Besides that, properly restoring the microgrid after faults or after disturbances is critical for better energy security and reliability. Therefore, it is desirable to have controllers that are robust and able to regulate and stabilize the system properly. Primary and secondary level controllers of microgrids are responsible for the stability and regulation of the system. Hence, modifying secondary controllers can be done to improve the robustness of the system. Model-based controllers can by synthesized to achieve this objective. However, they require adequate models that describe the dynamics of interests. Many of the models available have large number of states, which could result in high-order controllers and slow simulation time. Hence, a linearized symbolic *dq* based reduced-order model for secondary controller synthesis purposes was proposed in this dissertation. The model developed is convenient for the investigation of many issues such as controller design and tuning, parameter variations, and robust stability analysis under parametric uncertainty. Simulation results were performed to show that this model matches the high-order nonlinear model. Finally, a linear quadratic integral controller (LQI) was

synthesized. The controller was applied to both the reduced-order and the full-order model to demonstrate the application and the effectiveness of the model developed.

Future work based on this dissertation could focus on multiple aspects. One aspect is performing experimental studies to validate both the phase-based and model-based fault detection methods. Another research direction is performing more analytical studies on different fault types and conditions. In addition, enhancing the model-based fault detection method using principles of adaptive control so that the method is not reliant on the knowledge of system parameters is an interesting research direction to take. Finally, the reduced-order model developed laid a solid foundation to perform robust stability analysis under parametric uncertainty and synthesize robust controllers.

# APPENDIX A

## LQI CONTROL PARAMETERS

The weighting parameters used for LQI synthesis are

$$Q = diag\{0, 0, 250, 250, 20, 0, 0, 250, 250, 20, 0, 250, 250\}$$

$$R = diag\{50,50\}$$

The augmented $A$ matrix is $A_{aug}$ =

$$\begin{bmatrix}
-\omega_c & 0 & d_1 & 0 & \frac{3}{2}\omega_c I_{od10} & 0 & 0 & 0 & 0 & 0 & 0 & 0 & 0 \\
0 & -\omega_c & 0 & -d_1 & -\frac{3}{2}\omega_c I_{oq10} & 0 & 0 & 0 & 0 & 0 & 0 & 0 & 0 \\
-m_{p1} I_{oq10} & 0 & b_1 & a_1 & \frac{1}{L_1} & 0 & 0 & \frac{-Z_L}{L_1} & \frac{Z_L}{L_1}\delta_{20} & 0 & \frac{Z_L}{L_1} I_{oq20} & 0 & 0 \\
m_{p1} I_{od10} & 0 & m_1 & b_1 & 0 & 0 & 0 & \frac{-Z_L}{L_1}\delta_{20} & \frac{-Z_L}{L_1} & 0 & -\frac{Z_L}{L_1} I_{od20} & 0 & 0 \\
0 & n_{q1} c_1 & -\frac{1}{C_{f1}} & 0 & c_1 & 0 & 0 & 0 & 0 & 0 & 0 & 0 & 0 \\
0 & 0 & 0 & 0 & 0 & -\omega_c & 0 & d_2 & 0 & \frac{3}{2}\omega_c I_{od20} & 0 & 0 & 0 \\
0 & 0 & 0 & 0 & 0 & 0 & -\omega_c & 0 & -d_2 & -\frac{3}{2}\omega_c I_{oq20} & 0 & 0 & 0 \\
0 & 0 & \frac{-Z_L}{L_2} & 0 & 0 & -m_{p2} I_{oq20} & 0 & b_2 & a_2 & \frac{1}{L_2} & 0 & 0 & 0 \\
0 & 0 & 0 & \frac{-Z_L}{L_2} & 0 & m_{p2} I_{od20} & 0 & m_2 & b_2 & 0 & 0 & 0 & 0 \\
0 & 0 & 0 & 0 & 0 & 0 & n_{q2} c_2 & -\frac{1}{C_{f2}} & 0 & c_2 & 0 & 0 & 0 \\
m_{p1} & 0 & 0 & 0 & 0 & -m_{p2} & 0 & 0 & 0 & 0 & 0 & 0 & 0 \\
0 & 0 & 0 & 0 & -1 & 0 & 0 & 0 & 0 & 0 & 0 & 0 & 0 \\
0 & 0 & 0 & 0 & 0 & 0 & 0 & 0 & 0 & -1 & 0 & 0 & 0
\end{bmatrix}$$

The augmented *B* matrix is

$$B_{aug} = \begin{bmatrix} 0 & 0 & 0 & 0 & -c_1 & 0 & 0 & 0 & 0 & 0 & 0 & 0 & 0 \\ 0 & 0 & 0 & 0 & 0 & 0 & 0 & 0 & 0 & -c_2 & 0 & 0 & 0 \end{bmatrix}^T$$

The augmented C matrix is

$$C_{aug} = \begin{bmatrix} 0 & 0 & 0 & 0 & 1 & 0 & 0 & 0 & 0 & 0 & 0 & 0 & 0 \\ 0 & 0 & 0 & 0 & 0 & 0 & 0 & 0 & 0 & 1 & 0 & 0 & 0 \end{bmatrix}$$

## BIBLIOGRAPHY


[1] N. Tesla, “The Problem of Increasing Human Energy with Special References to The Harnessing of The Sun’s Energy,” *Century Magazine*, 1900.

[2] R. H. Lasseter, “MicroGrids,” in *2002 IEEE Power Engineering Society Winter Meeting. Conference Proceedings (Cat. No.02CH37309)*, 2002, vol. 1, pp. 305–308.

[3] N. Hatziargyriou, H. Asano, R. Iravani, and C. Marnay, “Microgrids,” *IEEE Power Energy Mag.*, vol. 5, no. 4, pp. 78–94, Jul. 2007.

[4] R. H. Lasseter and P. Paigi, “Microgrid: a conceptual solution,” in *2004 IEEE 35th Annual Power Electronics Specialists Conference (IEEE Cat. No.04CH37551)*, pp. 4285–4290.

[5] International Energy Agency, “World Energy Outlook 2015,” Paris, 2015.

[6] J. Minkel, “The 2003 Northeast Blackout--Five Years Later,” *Scientific American*, 2008. [Online]. Available: https://www.scientificamerican.com/article/2003-blackout-five-years-later/. [Accessed: 22-Mar-2017].

[7] “Microgrid Energy Systems.” [Online]. Available: http://www.eaton.com/FTC/utilities/MicrogridEnergySystems/index.htm. [Accessed: 22-Mar-2017].

[8] “Microgrid Solutions from ABB.” [Online]. Available: http://new.abb.com/microgrids. [Accessed: 22-Mar-2017].

[9] “Microgrids Solutions - Smart Grid Solutions - Siemens.” [Online]. Available: http://w3.usa.siemens.com/smartgrid/us/en/microgrid/pages/microgrids.aspx. [Accessed: 22-Mar-2017].

[10] “GE Grid Solutions : Grid IQ Microgrid Control System.” [Online]. Available: https://www.gegridsolutions.com/multilin/catalog/mcs.htm. [Accessed: 22-Mar-2017].

[11] S. Teimourzadeh, F. Aminifar, M. Davarpanah, and J. M. Guerrero, “Macroprotections for Microgrids: Toward a New Protection Paradigm Subsequent to Distributed Energy Resource Integration,” *IEEE Ind. Electron. Mag.*, vol. 10, no. 3, pp. 6–18, Sep. 2016.

[12] B. S. Hartono and R. Setiabudy, “Review of microgrid technology,” in *2013 International Conference on QiR*, 2013, pp. 127–132.

[13] H. Han, X. Hou, J. Yang, J. Wu, M. Su, and J. M. Guerrero, “Review of Power Sharing Control Strategies for Islanding Operation of AC Microgrids,” *IEEE Trans. Smart Grid*, vol. 7, no. 1, pp. 200–215, Jan. 2016.

[14] Y. Han, H. Li, P. Shen, E. Coelho, and J. Guerrero, “Review of Active and Reactive Power Sharing Strategies in Hierarchical Controlled Microgrids,” *IEEE Trans. Power Electron.*, vol. 8993, no. c, pp. 1–1, 2016.

[15] N. Jayawarna, X. Wu, Y. Zhang, N. Jenkins, and M. Barnes, “Stability of a microgrid,” in *3rd IET International Conference on Power Electronics, Machines and Drives (PEMD 2006)*, 2006, vol. 2006, pp. 316–320.

[16] A. H. Kasem, “Microgrid Stability Characterization Subsequent to Fault Triggered Islanding Incidents,” *Power Deliv. IEEE Trans.*, vol. 27, no. 2, pp. 658–669, 2012.

[17] X. Tang, W. Deng, and Z. Qi, “Investigation of the Dynamic Stability of Microgrid,” vol. 29, no. 2, pp. 698–706, 2014.

[18] J. Keller and B. Kroposki, “Understanding Fault Characteristics of Inverter-Based Distributed Energy Resources,” 2010.

[19] M. R. Islam and H. A. Gabbar, “Analysis of Microgrid protection strategies,” in *2012 International Conference on Smart Grid (SGE)*, 2012, pp. 1–6.

[20] H. Nikkhajoei and R. H. Lasseter, “Microgrid Protection,” in *2007 IEEE Power Engineering Society General Meeting*, 2007, pp. 1–6.

[21] H. J. Laaksonen, “Protection Principles for Future Microgrids,” *IEEE Trans. Power Electron.*, vol. 25, no. 12, pp. 2910–2918, Dec. 2010.

[22] S. Gopalan, V. Sreeram, H. Iu, and Y. Mishra, “A flexible protection scheme for an islanded Multi-Microgrid,” in *IEEE PES ISGT Europe 2013*, 2013, pp. 1–5.

[23] M. Esreraig and J. Mitra, “An observer-based protection system for microgrids,” in *2011 IEEE Power and Energy Society General Meeting*, 2011, pp. 1–7.

[24] A. Mohamed, S. Vanteddu, and O. Mohammed, “Protection of bi-directional AC-DC/DC-AC converter in hybrid AC/DC microgrids,” *Conf. Proc. - IEEE SOUTHEASTCON*, pp. 1–6, 2012.

[25] W. Huang, T. Nengling, X. Zheng, C. Fan, X. Yang, and B. J. Kirby, “An Impedance Protection Scheme for Feeders of Active Distribution Networks,” *IEEE Trans. Power Deliv.*, vol. 29, no. 4, pp. 1591–1602, Aug. 2014.

[26] S. Beheshtaein, M. Savaghebi, J. C. Vasquez, S. Member, and J. M. Guerrero, “Protection of AC and DC Microgrids : Challenges , Solutions and Future Trends,” pp. 5253–5260, 2015.

[27] Bin Li, Yongli Li, Zhiqian Bo, and A. Klimek, “Design of protection and control scheme for microgrid systems,” in *Universities Power Engineering Conference (UPEC), 2009 Proceedings of the 44th International*, 2009, pp. 1–5.

[28] M. A. Zamani, T. S. Sidhu, and A. Yazdani, “Investigations Into the Control and Protection of an Existing Distribution Network to Operate as a Microgrid: A Case Study,” *IEEE Trans. Ind. Electron.*, vol. 61, no. 4, pp. 1904–1915, Apr. 2014.

[29] M. A. Zamani, A. Yazdani, and T. S. Sidhu, “A control strategy for enhanced operation of inverter-based microgrids under transient disturbances and network faults,” *IEEE Trans. Power Deliv.*, vol. 27, no. 4, pp. 1737–1747, 2012.

[30] M. A. Zamani, “Protection and Control of Active Distribution Networks and Microgrids,” no. December, p. 196, 2012.

[31] M. A. Zamani, T. S. Sidhu, and A. Yazdani, “A Protection Strategy and Microprocessor-Based Relay for Low-Voltage Microgrids,” *IEEE Trans. Power Deliv.*, vol. 26, no. 3, pp. 1873–1883, Jul. 2011.

[32] D. E. Olivares *et al.*, “Trends in Microgrid Control,” *IEEE Trans. Smart Grid*, vol. 5, no. 4, pp. 1905–1919, Jul. 2014.

[33] J. M. Guerrero, J. C. Vasquez, J. Matas, M. Castilla, and L. G. de Vicuna, “Control Strategy for Flexible Microgrid Based on Parallel Line-Interactive UPS Systems,” *IEEE Trans. Ind. Electron.*, vol. 56, no. 3, pp. 726–736, Mar. 2009.

[34] F. L. Lewis, Z. Qu, A. Davoudi, and A. Bidram, “Secondary control of microgrids based on distributed cooperative control of multi-agent systems,” *IET Gener. Transm. Distrib.*, vol. 7, no. October 2012, pp. 822–831, 2013.

[35] N. Pogaku, M. Prodanović, and T. C. Green, “Modeling, analysis and testing of autonomous operation of an inverter-based microgrid,” *IEEE Trans. Power Electron.*, vol. 22, no. 2, pp. 613–625, 2007.

[36] J. M. Guerrero, J. C. Vasquez, J. Matas, L. G. De Vicuña, and M. Castilla, “Hierarchical control of droop-controlled AC and DC microgrids - A general approach toward standardization,” *IEEE Trans. Ind. Electron.*, vol. 58, no. 1, pp. 158–172, 2011.

[37] A. Bidram and A. Davoudi, “Hierarchical Structure of Microgrids Control System,” *IEEE Trans. Smart Grid*, vol. 3, no. 4, pp. 1963–1976, Dec. 2012.

[38] J. Kim, J. M. Guerrero, P. Rodriguez, R. Teodorescu, and K. Nam, “Mode adaptive droop control with virtual output impedances for an inverter-based flexible AC microgrid,” *IEEE Trans. Power Electron.*, vol. 26, no. 3, pp. 689–701, 2011.

[39] J. He and Y. W. Li, “Analysis, design, and implementation of virtual impedance for power electronics interfaced distributed generation,” *IEEE Trans. Ind. Appl.*, vol. 47, no. 6, pp. 2525–2538, 2011.

[40] Y. Mohamed and E. F. El-Saadany, “Adaptive Decentralized Droop Controller to Preserve Power Sharing Stability of Paralleled Inverters in Distributed Generation Microgrids,” *IEEE Trans. Power Electron.*, vol. 23, no. 6, pp. 2806–2816, Nov. 2008.

[41] N. Bottrell, M. Prodanovic, and T. C. Green, “Dynamic Stability of a Microgrid With an Active Load,” *IEEE Trans. Power Electron.*, vol. 28, no. 11, pp. 5107–5119, Nov. 2013.

[42] Y. A.-R. I. Mohamed and A. A. Radwan, “Hierarchical Control System for Robust Microgrid Operation and Seamless Mode Transfer in Active Distribution Systems,” *IEEE Trans. Smart Grid*, vol. 2, no. 2, pp. 352–362, Jun. 2011.

[43] M. C. Chandorkar, D. M. Divan, and R. Adapa, “Control of parallel connected inverters in standalone AC supply systems,” *IEEE Trans. Ind. Appl.*, vol. 29, no. 1, pp. 136–143, 1993.

[44] K. De Brabandere, B. Bolsens, J. Van den Keybus, A. Woyte, J. Driesen, and R. Belmans, “A Voltage and Frequency Droop Control Method for Parallel Inverters,” *IEEE Trans. Power Electron.*, vol. 22, no. 4, pp. 1107–1115, Jul. 2007.

[45] J. a P. Lopes, C. L. Moreira, and a. G. Madureira, “Defining control strategies for microgrids islanded operation,” *IEEE Trans. Power Syst.*, vol. 21, no. 2, pp. 916–924, 2006.

[46] M. Savaghebi, A. Jalilian, J. C. Vasquez, and J. M. Guerrero, “Secondary Control for Voltage Quality Enhancement in Microgrids,” *IEEE Trans. Smart Grid*, vol. 3, no. 4, pp. 1893–1902, Dec. 2012.

[47] A. Bidram, A. Davoudi, F. L. Lewis, and J. M. Guerrero, “Distributed Cooperative Secondary Control of Microgrids Using Feedback Linearization,” *IEEE Trans. Power Syst.*, vol. 28, no. 3, pp. 3462–3470, Aug. 2013.

[48] E. Barklund, N. Pogaku, M. Prodanovic, C. Hernandez-Aramburo, and T. C. Green, “Energy Management in Autonomous Microgrid Using Stability-Constrained Droop Control of Inverters,” *IEEE Trans. Power Electron.*, vol. 23, no. 5, pp. 2346–2352, Sep. 2008.

[49] A. Pantoja and N. Quijano, “A Population Dynamics Approach for the Dispatch of Distributed Generators,” *IEEE Trans. Ind. Electron.*, vol. 58, no. 10, pp. 4559–4567, Oct. 2011.

[50] S. V. Iyer, M. N. Belur, and M. C. Chandorkar, “A generalized computational method to determine stability of a multi-inverter microgrid,” *IEEE Trans. Power Electron.*, vol. 25, no. 9, pp. 2420–2432, 2010.

[51] J. M. Guerrero, L. GarciadeVicuna, J. Matas, M. Castilla, and J. Miret, “A Wireless Controller to Enhance Dynamic Performance of Parallel Inverters in Distributed Generation Systems,” *IEEE Trans. Power Electron.*, vol. 19, no. 5, pp. 1205–1213, Sep. 2004.

[52] X. Guo, Z. Lu, B. Wang, X. Sun, L. Wang, and J. M. Guerrero, “Dynamic Phasors-Based Modeling and Stability Analysis of Droop-Controlled Inverters for Microgrid Applications,” *IEEE Trans. Smart Grid*, vol. 5, no. 6, pp. 2980–2987, Nov. 2014.

[53] M. Rasheduzzaman, J. A. Mueller, and J. W. Kimball, “Reduced-Order Small-Signal Model of Microgrid Systems,” *IEEE Trans. Sustain. Energy*, vol. 6, no. 4, pp. 1292–1305, Oct. 2015.

[54] E. A. A. Coelho, P. C. Cortizo, and P. F. D. Garcia, “Small signal stability for single phase inverter connected to stiff AC system,” in *Conference Record of the 1999 IEEE Industry Applications Conference. Thirty-Forth IAS Annual Meeting (Cat. No.99CH36370)*, vol. 4, pp. 2180–2187.

[55] E. A. A. Coelho, P. C. Cortizo, and P. F. D. Garcia, “Small-signal stability for parallel-connected inverters in stand-alone AC supply systems,” *IEEE Trans. Ind. Appl.*, vol. 38, no. 2, pp. 533–542, 2002.

[56] P. T. Lewis, B. M. Grainger, H. A. Al Hassan, A. Barchowsky, and G. F. Reed, “Fault Section Identification Protection Algorithm for Modular Multilevel Converter-Based High Voltage DC With a Hybrid Transmission Corridor,” *IEEE Trans. Ind. Electron.*, vol. 63, no. 9, pp. 5652–5662, Sep. 2016.

[57] H. A. Al Hassan, B. M. Grainger, T. E. McDermott, and G. F. Reed, “Fault location identification of a hybrid HVDC-VSC system containing cable and overhead line segments using transient data,” in *2016 IEEE/PES Transmission and Distribution Conference and Exposition (T&D)*, 2016, pp. 1–5.

[58] E. Sortomme, S. S. Venkata, and J. Mitra, “Microgrid Protection Using Communication-Assisted Digital Relays,” *IEEE Trans. Power Deliv.*, vol. 25, no. 4, pp. 2789–2796, Oct. 2010.

[59] S. M. Brahma and A. A. Girgis, “Development of Adaptive Protection Scheme for Distribution Systems With High Penetration of Distributed Generation,” *IEEE Trans. Power Deliv.*, vol. 19, no. 1, pp. 56–63, Jan. 2004.

[60] Hui Wan, K. K. Li, and K. P. Wong, “An multi-agent approach to protection relay coordination with distributed generators in industrial power distribution system,” in *Fourtieth IAS Annual Meeting. Conference Record of the 2005 Industry Applications Conference, 2005.*, vol. 2, pp. 830–836.

[61] B. Hadzi-Kostova and Z. Styczynski, “Network Protection in Distribution Systems with Dispersed Generation,” in *2005/2006 PES TD*, pp. 321–326.

[62] E. Sortomme, G. J. Mapes, B. A. Foster, and S. S. Venkata, “Fault analysis and protection of a microgrid,” in *2008 40th North American Power Symposium*, 2008, pp. 1–6.

[63] E. Casagrande, W. L. Woon, H. H. Zeineldin, and D. Svetinovic, “A Differential Sequence Component Protection Scheme for Microgrids With Inverter-Based Distributed Generators,” *IEEE Trans. Smart Grid*, vol. 5, no. 1, pp. 29–37, Jan. 2014.

[64] R. M. Tumilty, M. Brucoli, G. M. Burt, and T. C. Green, “Approaches to network protection for inverter dominated electrical distribution systems,” in *3rd IET International Conference on Power Electronics, Machines and Drives (PEMD 2006)*, 2006, vol. 2006, pp. 622–626.

[65] M. A. Redfern and H. Al-Nasseri, “Protection of micro-grids dominated by distributed generation using solid state converters,” in *IET 9th International Conference on Developments in Power Systems Protection (DPSP 2008)*, 2008, vol. 2008, pp. 669–673.

[66] N. Jayawarna, C. Jones, M. Barnes, and N. Jenkins, “Operating MicroGrid Energy Storage Control during Network Faults,” in *2007 IEEE International Conference on System of Systems Engineering*, 2007, pp. 1–7.

[67] S. A. Saleh, “Signature-Coordinated Digital Multirelay Protection for Microgrid Systems,” *IEEE Trans. Power Electron.*, vol. 29, no. 9, pp. 4614–4623, Sep. 2014.

[68] E. Sortomme, J. Ren, and S. S. Venkata, “A differential zone protection scheme for microgrids,” in *2013 IEEE Power & Energy Society General Meeting*, 2013, pp. 1–5.

[69] P. Mahat, Z. Chen, B. Bak-Jensen, and C. L. Bak, “A Simple Adaptive Overcurrent Protection of Distribution Systems With Distributed Generation,” *IEEE Trans. Smart Grid*, vol. 2, no. 3, pp. 428–437, Sep. 2011.

[70] X. Li, A. Dysko, and G. Burt, “Enhanced protection for inverter dominated microgrid using transient fault information,” in *11th IET International Conference on Developments in Power Systems Protection (DPSP 2012)*, 2012, pp. P20–P20.

[71] X. Li, A. Dysko, and G. M. Burt, “Traveling Wave-Based Protection Scheme for Inverter-Dominated Microgrid Using Mathematical Morphology,” *IEEE Trans. Smart Grid*, vol. 5, no. 5, pp. 2211–2218, Sep. 2014.

[72] H. Al-Nasseri and M. A. Redfern, “Harmonics content based protection scheme for Micro-grids dominated by solid state converters,” in *2008 12th International Middle-East Power System Conference*, 2008, pp. 50–56.

[73] Shenxing Shi, Bo Jiang, Xinzhou Dong, and Zhiqian Bo, “Protection of microgrid,” in *10th IET International Conference on Developments in Power System Protection (DPSP 2010). Managing the Change*, 2010, pp. 11–11.

[74] H. H. Zeineldin, E. F. El-Saadany, and M. M. A. Salama, “Optimal coordination of overcurrent relays using a modified particle swarm optimization,” *Electr. Power Syst. Res.*, vol. 76, no. 11, pp. 988–995, Jul. 2006.

[75] R. Thangaraj, M. Pant, and K. Deep, “Optimal coordination of over-current relays using modified differential evolution algorithms,” *Eng. Appl. Artif. Intell.*, vol. 23, no. 5, pp. 820–829, Aug. 2010.

[76] T. S. Ustun, C. Ozansoy, and A. Zayegh, “Implementation of Dijkstra’s algorithm in a dynamic microgrid for relay hierarchy detection,” in *2011 IEEE International Conference on Smart Grid Communications (SmartGridComm)*, 2011, pp. 481–486.

[77] R. Ndou, J. I. Fadiran, S. Chowdhury, and S. P. Chowdhury, “Performance comparison of voltage and frequency based loss of grid protection schemes for microgrids,” in *2013 IEEE Power & Energy Society General Meeting*, 2013, pp. 1–5.

[78] L. Tao, C. Schwaegerl, S. Narayanan, and J. H. Zhang, “From laboratory Microgrid to real markets — Challenges and opportunities,” in *8th International Conference on Power Electronics - ECCE Asia*, 2011, pp. 264–271.

[79] G. Buigues, A. Dyśko, V. Valverde, I. Zamora, and E. Fernández, “Microgrid Protection: Technical challenges and existing techniques,” 2013.

[80] F. Katiraei, M. R. Iravani, and P. W. Lehn, “Micro-grid autonomous operation during and subsequent to islanding process,” *IEEE Trans. Power Deliv.*, vol. 20, no. 1, pp. 248–257, 2005.

[81] Fang Gao and M. R. Iravani, “A Control Strategy for a Distributed Generation Unit in Grid-Connected and Autonomous Modes of Operation,” *IEEE Trans. Power Deliv.*, vol. 23, no. 2, pp. 850–859, Apr. 2008.

[82] K. De Brabandere, B. Bolsens, J. Van den Keybus, A. Woyte, J. Driesen, and R. Belmans, “A Voltage and Frequency Droop Control Method for Parallel Inverters,” *IEEE Trans. Power Electron.*, vol. 22, no. 4, pp. 1107–1115, Jul. 2007.

[83] C. K. Sao and P. W. Lehn, “Autonomous Load Sharing of Voltage Source Converters,” *IEEE Trans. Power Deliv.*, vol. 20, no. 2, pp. 1009–1016, Apr. 2005.

[84] H. Nikkhajoei and R. H. Lasseter, “Distributed Generation Interface to the CERTS Microgrid,” *IEEE Trans. Power Deliv.*, vol. 24, no. 3, pp. 1598–1608, Jul. 2009.

[85] P. Piagi and R. H. Lasseter, “Autonomous control of microgrids,” in *2006 IEEE Power Engineering Society General Meeting*, 2006, p. 8 pp.

[86] I.-Y. Chung, W. Liu, D. A. Cartes, and K. Schoder, “Control parameter optimization for a microgrid system using particle swarm optimization,” in *2008 IEEE International Conference on Sustainable Energy Technologies*, 2008, pp. 837–842.

[87] E. Rokrok and M. E. H. Golshan, “Adaptive voltage droop scheme for voltage source converters in an islanded multibus microgrid,” *IET Gener. Transm. Distrib.*, vol. 4, no. 5, p. 562, 2010.

[88] G. Diaz, C. Gonzalez-Moran, J. Gomez-Aleixandre, and A. Diez, “Scheduling of Droop Coefficients for Frequency and Voltage Regulation in Isolated Microgrids,” *IEEE Trans. Power Syst.*, vol. 25, no. 1, pp. 489–496, Feb. 2010.

[89] C. K. Sao and P. W. Lehn, “Control and Power Management of Converter Fed Microgrids,” *IEEE Trans. Power Syst.*, vol. 23, no. 3, pp. 1088–1098, Aug. 2008.

[90] Yun Wei Li and Ching-Nan Kao, “An Accurate Power Control Strategy for Power-Electronics-Interfaced Distributed Generation Units Operating in a Low-Voltage Multibus Microgrid,” *IEEE Trans. Power Electron.*, vol. 24, no. 12, pp. 2977–2988, Dec. 2009.

[91] J. M. Guerrero, J. Matas, L. Garcia de Vicuna, M. Castilla, and J. Miret, “Decentralized Control for Parallel Operation of Distributed Generation Inverters Using Resistive Output Impedance,” *IEEE Trans. Ind. Electron.*, vol. 54, no. 2, pp. 994–1004, Apr. 2007.

[92] J. He and Y. W. Li, “Generalized closed-loop control schemes with embedded virtual impedances for voltage source converters with LC or LCL filters,” *IEEE Trans. Power Electron.*, vol. 27, no. 4, pp. 1850–1861, 2012.

[93] J. He and Y. W. Li, “Generalized closed-loop control (GCC) schemes with embedded virtual imepdances for voltage source converters,” *IEEE Energy Convers. Congr. Expo. Energy Convers. Innov. a Clean Energy Futur. ECCE 2011, Proc.*, pp. 479–486, 2011.

[94] Z. Jiang and X. Yu, “Active power — Voltage control scheme for islanding operation of inverter-interfaced microgrids,” in *2009 IEEE Power & Energy Society General Meeting*, 2009, pp. 1–7.

[95] J. C. Vasquez, J. M. Guerrero, A. Luna, P. Rodriguez, and R. Teodorescu, “Adaptive Droop Control Applied to Voltage-Source Inverters Operating in Grid-Connected and Islanded Modes,” *IEEE Trans. Ind. Electron.*, vol. 56, no. 10, pp. 4088–4096, Oct. 2009.

[96] Y. Li and Y. W. Li, “Power Management of Inverter Interfaced Autonomous Microgrid Based on Virtual Frequency-Voltage Frame,” *IEEE Trans. Smart Grid*, vol. 2, no. 1, pp. 30–40, Mar. 2011.

[97] Yan Li and Yun Wei Li, “Decoupled power control for an inverter based low voltage microgrid in autonomous operation,” in *2009 IEEE 6th International Power Electronics and Motion Control Conference*, 2009, pp. 2490–2496.

[98] J. M. Guerrero, L. Hang, and J. Uceda, “Control of Distributed Uninterruptible Power Supply Systems,” *IEEE Trans. Ind. Electron.*, vol. 55, no. 8, pp. 2845–2859, Aug. 2008.

[99] M. Prodanovic and T. C. Green, “High-Quality Power Generation Through Distributed Control of a Power Park Microgrid,” *IEEE Trans. Ind. Electron.*, vol. 53, no. 5, pp. 1471–1482, Oct. 2006.

[100] Chien-Liang Chen, Yubin Wang, Jih-Sheng Lai, Yuang-Shung Lee, and D. Martin, “Design of Parallel Inverters for Smooth Mode Transfer Microgrid Applications,” *IEEE Trans. Power Electron.*, vol. 25, no. 1, pp. 6–15, Jan. 2010.

[101] Q. C. Zhong and G. Weiss, “Synchronverters: Inverters that mimic synchronous generators,” *IEEE Trans. Ind. Electron.*, vol. 58, no. 4, pp. 1259–1267, 2011.

[102] I. Cvetkovic *et al.*, “Experimental verification of a virtual synchronous generator control concept,” *2016 IEEE 17th Work. Control Model. Power Electron.*, pp. 1–8, 2016.

[103] F. Blaabjerg, R. Teodorescu, M. Liserre, and A. V. Timbus, “Overview of Control and Grid Synchronization for Distributed Power Generation Systems,” *IEEE Trans. Ind. Electron.*, vol. 53, no. 5, pp. 1398–1409, Oct. 2006.

[104] A. Timbus, M. Liserre, R. Teodorescu, P. Rodriguez, and F. Blaabjerg, “Evaluation of Current Controllers for Distributed Power Generation Systems,” *IEEE Trans. Power Electron.*, vol. 24, no. 3, pp. 654–664, Mar. 2009.

[105] A. Micallef, M. Apap, C. Spiteri-Staines, J. M. Guerrero, and J. C. Vasquez, “Reactive Power Sharing and Voltage Harmonic Distortion Compensation of Droop Controlled Single Phase Islanded Microgrids,” *IEEE Trans. Smart Grid*, vol. 5, no. 3, pp. 1149–1158, May 2014.

[106] A. Mehrizi-Sani and R. Iravani, “Potential-Function Based Control of a Microgrid in Islanded and Grid-Connected Modes,” *IEEE Trans. Power Syst.*, vol. 25, no. 4, pp. 1883–1891, Nov. 2010.

[107] Y. Wang, Z. Chen, X. Wang, Y. Tian, Y. Tan, and C. Yang, “An Estimator-Based Distributed Voltage-Predictive Control Strategy for AC Islanded Microgrids,” *IEEE Trans. Power Electron.*, vol. 30, no. 7, pp. 3934–3951, Jul. 2015.

[108] Y. Wang, Yongdong Tan, Z. Chen, X. Wang, and Y. Tian, “A communication-less distributed voltage control strategy for a multi-bus AC islanded microgrid,” in *2014 International Power Electronics Conference (IPEC-Hiroshima 2014 - ECCE ASIA)*, 2014, pp. 3538–3545.

[109] J. W. Simpson-Porco, Q. Shafiee, F. Dorfler, J. C. Vasquez, J. M. Guerrero, and F. Bullo, “Secondary Frequency and Voltage Control of Islanded Microgrids via Distributed Averaging,” *IEEE Trans. Ind. Electron.*, vol. 62, no. 11, pp. 7025–7038, Nov. 2015.

[110] H. Bouattour, J. W. Simpson-Porco, F. Dorfler, and F. Bullo, “Further results on distributed secondary control in microgrids,” in *52nd IEEE Conference on Decision and Control*, 2013, pp. 1514–1519.

[111] J. W. Simpson-Porco, F. Dorfler, F. Bullo, Q. Shafiee, and J. M. Guerrero, “Stability, power sharing, & distributed secondary control in droop-controlled microgrids,” in *2013 IEEE International Conference on Smart Grid Communications (SmartGridComm)*, 2013, pp. 672–677.

[112] J. W. Simpson-Porco, F. Dörfler, and F. Bullo, “Synchronization and power sharing for droop-controlled inverters in islanded microgrids,” *Automatica*, vol. 49, no. 9, pp. 2603–2611, Sep. 2013.

[113] Y. Peng, Z. Shuai, J. Shen, J. Wang, C. Tu, and Y. Cheng, “Reduced order modeling method of inverter-based microgrid for stability analysis,” in *2017 IEEE Applied Power Electronics Conference and Exposition (APEC)*, 2017, pp. 3470–3474.

[114] A. Gururani, S. R. Mohanty, and J. C. Mohanta, “Microgrid protection using Hilbert–Huang transform based-differential scheme,” *IET Gener. Transm. Distrib.*, vol. 10, no. 15, pp. 3707–3716, Nov. 2016.

[115] A. H. Abdulwahid and S. Wang, “A new differential protection scheme for microgrid using Hilbert space based power setting and fuzzy decision processes,” in *2016 IEEE 11th Conference on Industrial Electronics and Applications (ICIEA)*, 2016, pp. 6–11.

[116] X. Ma, B. Li, Q. Wang, Z. Bo, M. Zhang, and X. Ma, “Research on microgrid protection based on transient polarity comparison,” in *2016 China International Conference on Electricity Distribution (CICED)*, 2016, pp. 1–5.

[117] S. H. Horowitz and A. G. Phadke, *Power system relaying*, 3rd ed. New York: Wiley, 2008.

[118] F. Katiraei, M. R. Iravani, and P. W. Lehn, “Small-signal dynamic model of a micro-grid including conventional and electronically interfaced distributed resources,” *IET Gener. Transm. Distrib.*, vol. 1, no. 3, p. 369, 2007.

[119] K. Yu, Q. Ai, S. Wang, J. Ni, and T. Lv, “Analysis and Optimization of Droop Controller for Microgrid System Based on Small-Signal Dynamic Model,” *IEEE Trans. Smart Grid*, pp. 1–11, 2015.

[120] M. Z. Kamh and R. Iravani, “Unbalanced Model and Power-Flow Analysis of Microgrids and Active Distribution Systems,” *IEEE Trans. Power Deliv.*, vol. 25, no. 4, pp. 2851–2858, Oct. 2010.

[121] A. Tuladhar, H. Jin, T. Unger, and K. Mauch, “Parallel operation of single phase inverter modules with no control interconnections,” in *Proceedings of APEC 97 - Applied Power Electronics Conference*, vol. 1, pp. 94–100.

[122] E. Barklund, N. Pogaku, M. Prodanovic, C. Hernandez-Aramburo, and T. C. Green, “Energy Management in Autonomous Microgrid Using Stability-Constrained Droop Control of Inverters,” *IEEE Trans. Power Electron.*, vol. 23, no. 5, pp. 2346–2352, Sep. 2008.

[123] F. L. Lewis, Z. Qu, A. Davoudi, and A. Bidram, “Secondary control of microgrids based on distributed cooperative control of multi-agent systems,” *IET Gener. Transm. Distrib.*, vol. 7, no. 8, pp. 822–831, Aug. 2013.

[124] Y. Yang, P. Enjeti, F. Blaabjerg, and H. Wang, “Wide-Scale Adoption of Photovoltaic Energy: Grid Code Modifications Are Explored in the Distribution Grid,” *IEEE Ind. Appl. Mag.*, vol. 21, no. 5, pp. 21–31, 2015.

[125] I. U. Nutkani, W. Peng, L. P. Chiang, and F. Blaabjerg, “Secondary Droop for Frequency and Voltage Restoration in Microgrids,” *2015 17th Eur. Conf. Power Electron. Appl. EPE-ECCE Eur. 2015*, 2015.

[126] I. U. Nutkani, P. C. Loh, P. Wang, T. K. Jet, and F. Blaabjerg, “Intertied ac-ac microgrids with autonomous power import and export,” *Int. J. Electr. Power Energy Syst.*, vol. 65, pp. 385–393, 2015.

[127] “IEEE application guide for IEEE Std 1547, IEEE standard for interconnecting distributed resources with electric power systems,” IEEE Std 1547.2, 2009.

[128] P. C. YOUNG and J. C. WILLEMS, “An approach to the linear multivariable servomechanism problem,” *Int. J. Control*, vol. 15, no. 5, pp. 961–979, May 1972.